PHYSIK-DEPARTMENT

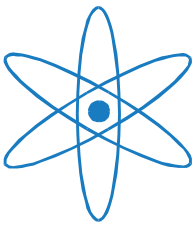

Quantum Optomechanics with Nonlinear Nanomechanical Resonators

Dissertation

von

Simon Uwe Rips

TECHNISCHE UNIVERSITÄT
MÜNCHEN

TECHNISCHE UNIVERSITÄT MÜNCHEN

Physik Department

Arbeitsgruppe “Quantum Optics and Quantum Dynamics”,
Lehrstuhl T34, Dr. Michael Hartmann

Quantum Optomechanics with Nonlinear Nanomechanical Resonators

Simon Uwe Rips

Vollständiger Abdruck der von der Fakultät für Physik der Technischen Universität München zur Erlangung des akademischen Grades eines

Doktors der Naturwissenschaften (Dr. rer. nat.)

genehmigten Dissertation.

Vorsitzender:	Univ.-Prof. Dr. R. Gross
Prüfer der Dissertation:	1. TUM Junior Fellow Dr. M. J. Hartmann
	2. Univ.-Prof. Dr. W. Zwerger

Die Dissertation wurde am 15.10.2013 bei der Technische Universität München eingereicht und durch die Fakultät für Physik am 28.11.2013 angenommen.

Abstract

In this thesis the quantum regime of nonlinear nanomechanical resonators in an opto-electro-mechanical setup is investigated theoretically. The interaction of such resonators with the light field inside a cavity has recently been employed to successfully cool their motion to the quantum mechanical ground state. Typically, this constitutes the precondition for investigations in that regime on the experimental side and defines the scientific context of this work. The central aspect here is the effect of an intrinsic mechanical nonlinearity, that is enhanced using electrostatic gradient forces that act onto the resonator. This nonlinearity can be employed to control the mechanical motion at the single phonon level. To demonstrate this, two different concepts are developed. One of them concerns the preparation of nonclassical steady states for the mechanical motion using appropriate laser drives for the cavity. Furthermore, a concept for quantum information processing with nanomechanical qubits is introduced. It is shown how a universal set of quantum gates can be implemented, where the interaction of multiple resonators with a common optical cavity mode can be used to conduct a fundamental entangling gate.

Zusammenfassung

In dieser Arbeit wird das quantenmechanische Regime von nichtlinearen, nanomechanischen Resonatoren in einem opto-elektro-mechanischem Aufbau theoretisch untersucht. Die Wechselwirkung solcher Nanoresonatoren mit dem Lichtfeld in einer optischen Mikrokavität wurde kürzlich erfolgreich genutzt um ihre Bewegung in den quantenmechanischen Grundzustand zu kühlen. Typischerweise stellt dies eine Voraussetzung für Untersuchungen in diesem Bereich auf der experimentellen Seite dar und definiert den wissenschaftlichen Kontext dieser Arbeit. Der zentrale Aspekt hier ist der Effekt einer intrinsischen Nichtlinearität im mechanischen elastischen Potential, welche mittels elektrostatischer Felder, die auf den Resonator wirken, verstärkt wird. Diese Nichtlinearität kann genutzt werden um die mechanische Bewegung auf dem Niveau einzelner Phononen zu kontrollieren. Um dies zu demonstrieren werden zwei verschieden Konzepte entwickelt. Ein Konzept beschäftigt sich mit der Preparation von nichtklassischen Zuständen der mechanischen Bewegung unter Benutzung passender Laseranregungen der optischen Kavität. Des Weiteren wird ein Konzept zur Quanteninformationsverarbeitung mit nanomechanischen Qubits vorgestellt. Es wird gezeigt wie ein universaler Satz von Quantengattern implementiert werden kann, wobei die Wechselwirkung mehrerer Nanoresonatoren mit einer gemeinsamen Photonmode benutzt wird um ein fundamentales, Verschränkung erzeugendes Gatter auszuführen.

Within the framework of this thesis, the following articles were published in refereed journals:

- S. Rips, M. Kiffner, I. Wilson-Rae and M. J. Hartmann, *Steady-state negative Wigner functions of nonlinear nanomechanical oscillators*, New J. Phys. **14**, 023042 (2012).
- S. Rips and M. J. Hartmann, *Quantum Information Processing with Nanomechanical Qubits*, Phys. Rev. Lett. **110**, 120503 (2013).
- S. Rips, I. Wilson-Rae and M. J. Hartmann, *Nonlinear nanomechanical resonators for quantum optoelectromechanics*, Phys. Rev. A **89**, 013854 (2014).

Contents

Introduction

A large part of today's scientific research in the field of quantum mechanics and in particular of quantum optics is driven by the idea of controlling small quantum systems with a very high level of precision. Here, small is meant in the sense of elementary, like single particles or single modes of a field. Various example systems range from single photons over single trapped ions or atoms to solid state devices like quantum dots and superconducting circuits. The motivation behind that approach is at least twofold. One goal has always been to implement precise experimental tests of fundamental predictions of quantum mechanics, like for instance loop-whole free tests of nonclassical correlations that arise from entanglement and are quantified by Bell's inequalities [1, 2]. But moreover, this approach of course follows a very general and successful principle, that is understanding and controlling elementary building blocks in order to advance to more complex applications and systems later on. One result of these later step are so called hybrid quantum systems that nowadays exist in various combinations.

During the last decade, a very fundamental class of devices, formed by various types of micro- and nanomechanical resonators, has approached the field of quantum physics. To a large part, this development has been driven by the progress in the top-down fabrication of structures on the micro- and nanoscale, including various mechanical structures like strings, bars, and cantilevers. Those devices are used in many technical applications. Some of them combine very high quality factors with ultra low masses, which makes them suitable for detecting very small forces [3, 4, 5]. The capability of mechanical resonators to couple to electromagnetic fields in a broad frequency range is employed for example in electrical signal processing, where they can serve as transducers or very precise frequency filters. These technical applications motivated the fabrication of resonators with increasing quality factors and frequencies and decreasing size.

The other important key developement was the progress in a relatively young subfield of quantum optics, that is the field of cavity optomechanics. This field is concerned with the interaction of the light field inside an optical cavity with the motion of mechanical resonators. For a recent review see [6]. While the idea that radiation forces exerted by light can influence the motion of mechanical resonators has been considered quite early [7], a significant interaction strength that overcomes thermal driving forces that act onto the mechanical resonator was only reached much later.

Only a bit more than ten years ago, the first optomechanical experiments started to implement cavity assisted sideband cooling of mechanical motion [8, 9, 10], a method that had been transferred from laser cooling of atoms and molecules. The critial step that finally introduced mechanical resonators to the realm of quantum mechanics was done when optomechanical experiments achieved cooling that was sufficient to reach the ground state of mechanical motion [11, 12, 13].

This development and the implicated perspective for the field of quantum physics is indeed outstanding. While mechanical resonators are the role model for the most fundamental system studied both in classical and quantum physics, the harmonic oscillator, they have always been associated to the classical world. This is because even typical nanomechanical resonators consist of billions of atoms and in that sense form a macroscopic body, whereas the rules of quantum mechanics have been developed to explain the world at the scale of single atoms. Consequently, unlike it is for atoms, the classical description of nano- and micromechanical resonators proved to be highly accurate in applications that have been considered before. The possibility to study the motion of mechanical resonators near the groundstate now holds manifold perspectives for further investigations. On a fundamental side, it promises insight into fundamental questions concerning decoherence [14]. On a more technical side, mechanical resonators in the quantum regime have great potential for hybrid quantum systems, since they can combine various coupling mechanisms to different types of other quantum systems. For example, similar to their previously mentioned use as transducers in classical signal processing, micromechanical resonators have already been considered as transducers between different quantum systems for purposes in quantum information processing [15, 16].

It is well known, that introducing a nonlinear element to a quantum system is crucial to be able to observe nonclassical effects. This is because in a linear system, the expectation values of observables follow the corresponding classical equations of motion [17]. A common way to characterize the nonclassicality of a quantum state is given by considering its Wigner representation. This phase space distribution has similarities to a classical probability distribution, but shows negative valued regions for nonclassical states. For a linear system that is subject to classical drives and embedded in a thermal environment, this Wigner distribution always shows a Gaussian shape. This is also true for systems that are close to the ground state, so that cooling a quantum system alone is not sufficient to observe nonclassical behaviour. Accordingly, introducing nonlinearites to otherwise linear systems is a common approach in quantum mechanical experiments: In superconducting circuits, for example, Josephson junctions are used as nonlinear elements to observe quantum effects. Here, we investigate the quantum regime for a nonlinear nanomechanical resonator in an opto-electromechanical setup. Thereby, the focus is set on generating and employing distinct nonclassical effects in the motion of the nanomechnical resonator. The approach that is introduced in this thesis relies on different elements: The interaction of the resonator with a laser driven optical cavity is neccesary to assure the regime of few motional excitations, but it is also used as a control element to induce more specific effects on the mechanical motion. Furthermore, electrostatic

fields are used to apply gradient forces onto the resonator. This is a common tool in the field of nanoelectromechanical systems (NEMS) that can be used to drive or tune nanomechanical resonators via their polarizability [18]. Finally, a novel element that is employed here, is a nonlinear contribution to the elastic potential of the mechanical resonator. This mechanical nonlinearity is of central importance, since it allows to resolve and address the individual energy levels of the mechanical resonator. Technically, such an intrinsic nonlinearity exists for every mechanical resonator, yet in most cases it is just too weak to be of any significance. While there exist attempts to make the mechanical motion nonlinear by employing the coupling to nonlinear ancilla systems [19, 20, 21], we here use a different approach: The intrinsic nonlinear effects are enhanced by tuning the nanoresonator close to the buckling instability [22, 23]. While the dynamics of a such a nonlinear nanomechanical resonator, sometimes also termed duffing oscillator, has been investigated both in the classical and the quantum regime before [24, 25], the additional interaction with an optical cavity is a novel aspect that can be used to exploit the nonlinear mechanical character.

It is important to note, that in optomechanical systems the interaction between the photons and the mechanical motion is already nonlinear itself, provided the optomechanical interaction is strong enough. To reach such strong optomechanical interactions is still challenging, yet a significant fraction of the current research in the field is concerned with quantum effects that occur in this nonlinear interaction regime [26, 27]. Here, we instead consider the regime of weak optomechanical coupling, which leads to a regime where nonlinear contributions to the interaction can be negelected. Besides the fact that this regime is much easier to attain, his has the following advantages: First, we avoid that the relevant mechanical and optical modes hybridize, so that the mechanical state can be characterised separately. This is important since the goal is to produce and analyze quantum effects for the resonator. Second, the ability to use the cavity as a control element relies on the linearized interaction regime. For instance, also the previously mentioned laser cooling technique works only in the weak coupling regime.

The combination of the cavity field and the electrostatic fields as control elements on the one side and a nonlinear nanomechanical resonator capable of distinct nonclassical behaviour on the other side opens up diverse possibilities to investigate the quantum regime of nanomechanical resonators. Following the general approach or idea that has been described aove, this is demonstrated by elaborating two different schemes: In the first scheme, we describe the preparation of nonclassical steady states for a single mechanical resonator. Since the groundstate for mechanical motion has already been reached, this could be one possible next step to be implemented in optomechanical experiments. The second scheme is a more advanced application comprising several nanoresonators that act as nanomechanical qubits. The qubits in that approach are formed by the two lowest energy levels for each of the nanoresoantors, that are tuned to be stronly nonlinear. The availible control channels are found to be sufficient to implement fundamental quantum logical operations on the resonators.

The main part of this thesis is organized as follows: In chapter 1 the basic model that describes the dynamics of the considered system is introduced. There, the emphasis is placed on motivating the basic concept of the optomechanical interaction between the mechanical degree of freedom and a laser driven cavity. Furthermore, standard formalisms to include damping effects are added to the description of the dynamics. The existance of a mechanical nonlinearity does not modify the standard optomechanical coupling mechanism so that in this chapter it is only introduced rather shortly. However, understanding the physical origin of the nonlinearity and its properties in a quantum description of the mechanical mode is a central aspect in this thesis. Therefore, chapter 2 provides a detailed derivation of the mechanical nonlinearity starting from elasticity theory for thin rods. In this chapter we also describe the possiblity to tune the mechanical resonance frequency using the electrostatic gradient fields. This aspect is important in this context since tuning is used to enhance the quantum nonlinearity of the resonator drastically. In chapter 3, a possible implementation is introduced. This setup employs a high-Q microtoroid optical cavity and carbon nanotubes (CNT) as nanomechanical resonators. The coupling mechanism in this combination differs from the standart optomechanical coupling, but adapts the same shape in the mathematical description. This and the corresponding optomechanical coupling strength is also derived in this chapter. Furthermore, possible additional damping and decoherence sources that are specific to this setup are discussed. In chapter 4 we introduce a scheme that allows for the preparation of nonclassical steady states of a single nanomechanical resonator. As this scheme is closely related to the previously mentioned laser cooling technique for mechanical resonators, we start with a short sketch of its underlying principle and its theoretical description. Then we motivate a common concept to distinguish classical states from nonclassical states by considering their Wigner functions. The description of the preparation scheme itself is followed by numerical results that show significant nonclassical character. The chapter is closed with the discussion of possible methods that allow to measure the prepared steady state. In the last chapter of the main part, chapter 5, we introduce the fundamental concepts for the implementation of quantum information precessing with nanomechanical qubits. This includes a short introduction to the concepts of nanomechanical qubits, that can be implemented in the regime of strong mechanical nonlinearities. Operational schemes that are used to perform single qubits gates as well as an entangling two-qubit gate follow. The expected performance of these quantum gates are discussed at hands of numerical results and the chapter is closed with a brief comment on possible intialisation and readout schemes. The thesis is closed with a conlusion and outlook. Details of calculations can be found in the appendix.

Chapter 1

Model

1.1 Introduction

We want to start by introducing the basic model considered in the theoretical investigations that are presented in this thesis. The model considered here is gained by a slight modification, or extension, of what is commonly used as a standard model of optomechanics. Optomechanical systems exist in various implementations, but the Hamiltonian that describes the optomechanical interaction is in most cases of the same shape. This general Hamiltonian can be motivated in an illustrative way by considering a paradigmatic setup that is shown in figure 1.1. The model is then further developed by considering a macroscopic steady state amplitude for the light field inside the cavity that is driven by a laser and subject to photon losses. This scenario gives rise to an enhanced and linearized interaction that is commonly considered in the operation regime of optomechanical setups. After introducing a formalism that includes the description of mechanical and optical damping, the mechanical nonlinearity is added to the model.

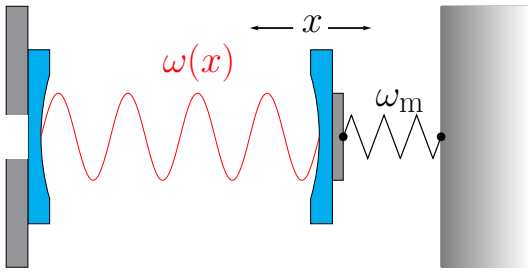

Figure 1.1: Paradigmatic sketch of the standard optomechanical interaction. One mirror of a two-sided cavity is attached to a spring. The position of the mirror determines the cavity resonance frequency, while the radiation pressure inside the cavity acts back on the movable mirror.

1.2 Paradigmatic optomechanical model

The standard optomechanical Hamiltonian describes the dispersive interaction between the light field inside a cavity and a mechanical resonator. Figure 1.1 shows the paradigmatic picture that illustrates the optomechanical interaction: One mirror of an optical cavity is attached to a spring, so that it is movable. The displacment $\mathcal{X}$ of the mirror determines the resonance frequency $\omega(\mathcal{X})$ for the light circulating inside the cavity. For small displacements $\mathcal{X}$, the cavity frequency $\omega(\mathcal{X})$ can be linearized so that the Hamiltonian of that system reads

$$\begin{aligned} H &= \left(\omega(\mathcal{X}=0) + \left.\frac{\partial\omega}{\partial\mathcal{X}}\right|_{\mathcal{X}=0}\mathcal{X}\right) a^\dagger a + H_\mathrm{m} \\ &= \omega_\mathrm{c} a^\dagger a + G_0 a^\dagger a \mathcal{X} + H_\mathrm{m} \\ &= H_\mathrm{c} + H_\mathrm{I} + H_\mathrm{m}\,, \end{aligned} \tag{1.1}$$

where ω_c is the free optical resonance frequency of a considered cavity mode that is described by photon operators a and $a^\dagger$. The frequency shift per oscillator deflection $G_0 = \partial\omega/\partial\mathcal{X}$ constitutes a coupling strength between mechanical motion and the optical field. If the mechanical part H_m describing the spring is a harmonic oscillator with frequency $\omega_\mathrm{m} \ll \omega_\mathrm{c}$, we have

$$H = \omega_\mathrm{c} a^\dagger a + G_0 x_\mathrm{ZPM} a^\dagger a (b^\dagger + b) + \omega_\mathrm{m} b^\dagger b\,, \tag{1.2}$$

where we also introduced phonon operators $b^\dagger$ and b for the mechanical oscillator, as well as its zero point motion x_ZPM. This shape of the optomechanical interaction is very general and found in very different types of realizations [6]. Note that the interaction part in this Hamiltonian is nonlinear, which makes this simple model already quite rich in its dynamics. In order to observe effects of this nonlinear coupling, the single photon-phonon coupling $G_0 x_\mathrm{ZPM}$ has to have a significant strenght, which in most of the realised optomechanical systems is not the case. But the interaction between the resonator and the cavity can also be effectively described for a large number of photons, which will be discussed in the following.

1.3 Laser driven cavity model

To further develop this model, we now have to consider an open system and include photon losses as well as input fields for the cavity. In this section we concentrate on the dynamics of a laser driven cavity as an open quantum system, which is used to motivate a refined picture of the optomechanical interaction. Therefore, mechanical damping will be introduced later.

Cavity losses usually originate from unavoidable imperfections in the mirror reflectivity and absorbtion of photons. In addition, there needs to be an open port where light can be injected into the cavity, which is usually done by a laser drive with a frequency ω_L that is tuned resonantly or close to the cavity resonance. Therefore

one needs to distinguish at least two different loss channels. Here we want to label the loss rate for the laser port by κ_{ex} and the other loss rates by κ_0. Usually the light that exits the cavity through the laser port can be detected, since it decays into known modes. This light can be used to gain information about the field inside the cavity, while the photons that exit through other decay channels are usually lost. There are several possibilites to describe the motion of the cavity including the laser drive and the damping effects. One is the quantum Langevin equation for the cavity field that reads

$$\dot{a} = -\frac{\kappa}{2}a + \mathrm{i}\Delta a + \sqrt{\kappa_{\mathrm{ex}}}a_{\mathrm{in}} + \sqrt{\kappa_0}c_{\mathrm{in}}\,, \tag{1.3}$$

where we introduced the total cavity decay rate $\kappa = \kappa_{\mathrm{ex}} + \kappa_0$ and the laser detuning $\Delta = \omega_{\mathrm{L}} - \omega_{\mathrm{c}}$ and applied a frame that rotates at the laser frequency. The effect of light that enters the cavity is governed by the input fields a_{in} for the laser mode and c_{in} for the other ports. Usually a_{in} represents a coherent state for the laser with $|\langle a_{\mathrm{in}}\rangle| = \sqrt{P_{\mathrm{in}}/\hbar\omega_{\mathrm{L}}}$ for a laser input power P_{in} and c_{in} simply represents vacumm fluctuations of the other sourrounding photon modes that enter the cavity. The outgoing fields have no influence on the cavity field. For the light that exits the cavity at the laser port, the out going field is connected to the cavity field and the input fields by the input-output relation [28]

$$a_{\mathrm{out}} = a_{\mathrm{in}} - \sqrt{\kappa_{\mathrm{ex}}}a\,. \tag{1.4}$$

This relation is very useful to gain information about the cavity field by measurement of the out going field. From equation (1.3) we find the steady state value for $\langle a\rangle$, which is given by

$$\langle a\rangle = \frac{\sqrt{\kappa_{\mathrm{ex}}}\,\langle a_{\mathrm{in}}\rangle}{-\mathrm{i}\Delta + \frac{\kappa}{2}} = \alpha\,. \tag{1.5}$$

Indeed, the steady state for the cavity is reached when the cavity losses and the laser input are balanced, and the cavity is then in a coherent state $|\alpha\rangle$ that contains $\langle a^\dagger a\rangle = |\alpha|^2$ photons. Since the relative phase between the cavity field and the laser field is immaterial here, we choose for convenience a frame such that the Rabi frequency

$$\Omega = -2\mathrm{i}\sqrt{\kappa_{\mathrm{ex}}}\,\langle a_{\mathrm{in}}\rangle \stackrel{!}{=} 2\sqrt{\frac{P_{\mathrm{in}}\kappa_{\mathrm{ex}}}{\hbar\omega_{\mathrm{L}}}} \tag{1.6}$$

is a real number, and therefore we can express the cavity background field by

$$\alpha = \frac{\Omega}{2\Delta + \mathrm{i}\kappa}\,. \tag{1.7}$$

Since for a coherent state, the fluctuations are small compared to the coherent background, it is convenient to separate the fluctuations from the background both for the laser input and for the cavity field by defining

$$\delta a_{\mathrm{in}} = a_{\mathrm{in}} - \langle a_{\mathrm{in}}\rangle\,, \tag{1.8}$$

$$\delta a = a - \alpha\,. \tag{1.9}$$

From that we can derive the Langevin equation for the cavity fluctuations around the coherent background which reads

$$\delta\dot{a} = -\frac{\kappa}{2}\delta a + \mathrm{i}\Delta\delta a + \sqrt{\kappa_{\mathrm{ex}}}\delta a_{\mathrm{in}} + \sqrt{\kappa_0}c_{\mathrm{in}}\,, \tag{1.10}$$

showing exact the same structure as the original equation (1.3), only that the input fields are all vacuum fluctuations now. Since the original photon operators are completely replaced here, we will relabel the fluctuations $\delta_a \rightarrow a$, and treat them like photons in a cavity that is only driven by vacuum fluctuations. This corresponds to simply shifting the photon operators by the coherent background amplitude $a \rightarrow \alpha + a$. Accordingly, we will also use the term "photons" instead of "fluctuations" sometimes.

1.4 Enhanced optomechanical coupling

We can now return to the optomechanical system (1.2) and use the separation (1.9) to study the interaction of the photon fluctuations of a laser driven cavity with the mechanical resonator. After changing to a rotating frame at the laser frequency and dropping constant contributions we find the shifted Hamiltonian

$$H' = -\Delta a^\dagger a + G_0 x_{\mathrm{ZPM}}\left[|\alpha|^2 + \alpha^* a + \alpha a^\dagger + a^\dagger a\right](b^\dagger + b) + \omega_{\mathrm{m}} b^\dagger b\,. \tag{1.11}$$

While the structure of the photon part is still the same, the interaction with the mechanical resoantor now has a different shape: First, we consider the contribution $\sim G_0|\alpha^2|$. This term represents a force of the macroscopic coherent background field onto the resonator that displaces the resonator to a new equilibrium position. In a subsequent chapter, we will introduce a possibility to compensate this term by external forces acting on the resonator, so that we need not to further consider this contribution. The second contribution $\sim G_0(\alpha a^\dagger + \alpha^* a)$ describes the interaction of the cavity fluctutations with the mechanical motion via the mechanical displacment. Compared to the interaction with photons for the original photon field, this interaction is enhanced by the background amplitude α. This allows to tune the coupling strength between photons and mechanical motion via the background field α. The third contribution $\sim G_0 a^\dagger a$ corresponds to the interaction with the cavity without a laser drive. For $\langle a^\dagger a\rangle \ll |\alpha|^2$ we can neglect this contribution, which amounts to a linearization of the optomechanical coupling. This condition is met, as long as the rate of possible population of the photon fluctuations originating from the coupling to the mechanical motion, is exceeded by a faster cavity decay rate. This condition can be expressed as $G_0^2 x_{\mathrm{ZPM}}^2(2\langle n_{\mathrm{m}}\rangle + 1) \ll \kappa^2$, where $\langle n_{\mathrm{m}}\rangle$ is the phonon number in the mechanical mode. Here, we will only consider regimes where this condition is met. With these transformations we can write the optomechanical Hamiltonian

$$H' = -\Delta a^\dagger a + \left(\frac{g_{\mathrm{m}}^*}{2}a + \mathrm{H.c.}\right)\left(b^\dagger + b\right) + H_{\mathrm{m}}\,, \tag{1.12}$$

where we introduced the enhanced optomechanical coupling $g_\mathrm{m} = 2G_0\alpha x_\mathrm{ZPM}$. The shifted Hamiltonian (1.12) describes the unitary time evolution of the optomechanical system, but it lacks in describing damping of the cavity and the mechanical motion. While we already introduced an open system for the cavity and used a quantum Langevin equation to motivate the shifted picture for the photons, for our calculations we will rather consider a quantum master equation to include damping effects.

1.5 Quantum master equation

The loss sources for the cavity field have already been introduced in section 1.3. Damping in nanomechanical devices is mostly caused by clamping losses [29], and due to the relatively low mechanical mode frequencies, that range from kHz to a few GHz, the occupation of the relevant bath modes has to be considered. To minimize the effect of thermal vibrations of the environment that enter the nanoresonator, optomechanical experiments are often conducted at very low tempertures below $1\,\mathrm{K}$. However even at those temperatures, the relevant bath mode occupation is well above unity. We introduce damping for the mechanical resonator and also for the photons phenomenologically using Lindblad damping operators that act on the system state ρ,

$$\mathcal{D}_{\hat{o}}\rho = 2\hat{o}\rho\hat{o}^\dagger - \hat{o}^\dagger\hat{o}\rho - \rho\hat{o}^\dagger\hat{o}\,. \tag{1.13}$$

The dynamics of the systems state ρ is then described by the corresponding master equation for the open system

$$\dot{\rho} = -\mathrm{i}\left[H', \rho\right] + \frac{\kappa}{2}\mathcal{D}_a\rho + \frac{\gamma_\mathrm{m}}{2}\left\{(\overline{n}+1)\mathcal{D}_b\rho + \overline{n}\mathcal{D}_{b^\dagger}\rho\right\}\,. \tag{1.14}$$

Here we introduced the mechanical decay rate γ_m, as well as the thermal occupation of the relevant mechanical bath modes

$$\overline{n} = \frac{1}{\exp\left[\hbar\omega_\mathrm{m}/k_\mathrm{B}T\right] - 1} \tag{1.15}$$

The photon bath is considered to be in the groundstate with zero thermal photons, which is a very good approximation for the considered temperatures $k_\mathrm{B}T \ll \hbar\omega_\mathrm{c}$.

Note that the shifted Hamiltonian H' can also be derived by formulating the master equation for the original Hamiltonian that still explicitly includes the laser drive. That Hamiltonian reads

$$H = -\Delta a^\dagger a + \frac{\Omega}{2}(a^\dagger + a) + G_0 x_\mathrm{ZPM} a^\dagger a(b^\dagger + b) + H_\mathrm{m} \tag{1.16}$$

where the laser drive is modeled using the Rabi frequency Ω introduced earlier. The cavity part has the right form to reproduce the dynamics of equation (1.3) with the

shifted input fields $\sqrt{\kappa_{\rm ex}}a_{\rm in} = \mathrm{i}\Omega/2 + \sqrt{\kappa_{\rm ex}}\delta a_{\rm in}$. Introducing the shift of the photon operators $a \to a + \alpha$ in the corresponding master equation

$$\dot{\rho} = -\mathrm{i}\left[H, \rho\right] + \frac{\kappa}{2}\mathcal{D}_a\rho + \frac{\gamma_{\rm m}}{2}\left\{(\overline{n}+1)\mathcal{D}_b\rho + \overline{n}\mathcal{D}_{b^\dagger}\rho\right\} . \tag{1.17}$$

also leads directly to (1.14). Here the correct value for α can be found by requiring that all terms that are linear in the fluctuations $a, a^\dagger$ cancel out. However, the fact that the shift α corresponds to the steady state amplitude of the cavity, is more explicitly developed via the Langevin approach. The master equation (1.14) is the common description of the optomechanical system that is used in many considerations. It has the advantage that it is a linear model, which means that it involves no terms that are of higher than second order in the system operators for photons and phonons a and b. This fact makes it relatively amenable to analytical solutions. In the next section we continue by introducing a extension of this model by considering a novel kind of nonlinearity.

1.6 Nonlinear mechanical resonator

At this point the system decribed by (1.12) is linear, which means that the corresponding equations of motion in (1.14) can usually be solved analytically. The central new aspect that we want to introduce here, is an additional nonlinear contribution in the mechanical potential that until now has been asumed to be harmonic. This additional contribution to the potential energy of the mechanical resonator is the next higher order correction with respect to the deflection $\mathcal{X}$. According to the symmetry of the problem this correction is proportional to $\mathcal{X}^4$. With that nonlinearity the mechanical part reads

$$H_{\rm m} = \omega_{\rm m} b^\dagger b + \frac{\lambda}{2}\left(b^\dagger + b\right)^4 , \tag{1.18}$$

where λ characterizes the strength of the nonlinearity with respect to single phonons. The nonlinearity prevents finding an exact analytical solution of (1.14). Approximate solutions that exist in certain regimes will be derived in chapters 4 and 5 of this thesis. The approximate solutions that are found analytically will be tested by a numerical solution of (1.14). A numerical treatment aquires the system described by ρ to be in a regime of very few exitations, so that the Hilbert space describing the system can be truncated. For the mechanical resonator, this is not a natural regime, as even at tempertures as low as several tens of milli Kelvin, the thermal occupation is much larger than unity. Therefore we usually have to asume an initial state that is precooled using cavity assisted sideband cooling. Then calculations are restricted to the transient regime for timescales that are much smaller than the mechanical relaxation time $\sim 1/\overline{n}\gamma_{\rm m}$. Another possiblity is that parameters considered in a calculation lead to a mechanical state with low excitation numbers, which has to be checked for consistency in the results. For the photon fluctuations, the constraint to

few excitations is met either by the weak couling regime $g_{\mathrm{m}} < \kappa$ or if the mechanical mode and the photon mode are sufficiently off resonant, $|\omega_{\mathrm{m}} - \Delta| \gg \kappa$.

In some situations, we will consider several cavity modes or several mechanical resonators, which contribute to the Hilbert space dimension. The generalizatons of (1.14) in these cases are straight forward and will be introduced in the respective places. In the next chapter we will describe the nature and origin of the introduced mechanical nonlinearity in detail, since this aspect is novel within the optomechanical context.

Chapter 2

The anharmonic nanomechanical resonator

2.1 Introduction

The central object of interest in this thesis is the physics of the nanomechanical resonator, especially regarding potential nonclassical behaviour or states. In subsequent chapters, we will formulate the mechanical resonator as a quantum object, embedded in a quantum system and subject to quantum mechanical equations of motion. A very important feature that will be brought to use is the existance of a geometric nonlinearity in the deflectional modes of the nanobeam. This leads to a nonlinear spectrum of motional excitations which is a prerequisite for the effects that will be discussed.

However, this kind of nonlinearity is rarely considered in common optomechanical models as its strength is typically too small to be resolved in an experiment as long as no enhancement techniques are applied. To explain the origin of this geometric nonlinearity, we will derive and formulate the classical equations of motion from elasticity theory in section 2.2. Thereby, we start with the harmonic description, also known as *thin beam theory*. We formulate it in a way that allows for an easy extension, where the nonlinearity arises quite clearly as a consequence of geometric constraints. We will find that the harmonic contribution to the potential is associated with the energy cost of bending the nanobeam, while the nonlinear contribution is associated with the energy cost of stretching the nanobeam. Streching naturally arises if the clamping points at both ends of the rod are not allowed to move.

It is worth mentioning that there exists at least one different approach for deriving the nonlinearity, that uses a more systematic expansion of the potential [23]. The derivation given there uses a slightly different model regarding the boundary conditions, which is that one of the end points is allowed to move so that the length of the rod is conserved upon deflection. This leads to a considerably different strength of the nonlinearity for the same beam geometry. However, for the physical realisation

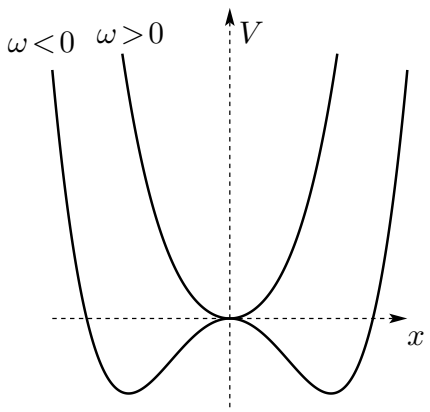

Figure 2.1: Potential for the duffing oscillator. At the critical point $\omega = 0$, the oscillator enters the bistable regime. Here the nonlinear corrections restore stability of the system.

of the nanobeam considered later, this model is not suitable.

After deriving the classical Hamiltonian for the nanobeam, we introduce a quantization of modes in section 2.3. The strength of the quantum nonlinearity, which is basically the growth of energy level spacings with excitation number, is found to be a tunable parameter. This is due to the fact that the spacial extension of phonons, given by the zero point motion, can be enhanced by tuning the resonance of the nanoresonator to lower frequencies. Larger amplitudes for single excitations then lead to higher impact of the nonlinear contribution. After all, it is this tunability that allows to access the regime of large enough nonlinearity, which all the applications that are introduced in this theses rely on.

There exist different approaches to tune the resonance frequency of a mechanical resonator. In [23, 30], tuning of the resonator has been included by additional strain along the rod axis, where compressive strain leads to decrease and tensile strain leads to increase of the mode frequencies. In the regime of high tensile stress the nanobeam behaves like a string, and tuning the resonance frequency is analog to tuning a guitar string. A different, particulary interesting regime is achieved when the fundamental mode frequency vanishes upon compressive strain, leading to the famous buckling instability, see figure 2.1. In this regime, only the nonlinear contributions asure stability of the system.

Here we will follow a different physical approach for tuning the nanoresonator, since the application of compressive strain to nanomechanical devices is probably very challening in an experiment. In section 2.4, we introduce the concept of tuning and driving with electrostatic gradient fields. Even though this approach is quite different with respect to the physical implementation, the effect on the fundamental mode motion is exactly the same, including the possible transition to the bistable regime. As we will see, this approach provides a versatile tool to control the nanomechanical motion, even at the level of single motional excitations.

2.2 Elasticity theory for thin rods

2.2.1 Harmonic description

We consider the rod to be homogenous with constant mass line density μ along the longitudinal axis, which we parametrize by $x \in \{0, L\}$, where L is the length of the undeflected rod. Deflection in the transverse direction is then decribed by a field $y(x)$ with $y(0) = y(L) = 0$, as the end points are fixed, compare figure 2.2**a)**. We also consider thin rods, which means that the transverse dimensions of the rod like width or radius are much smaller than the length of the rod and we are interested in transverse oscillations with wavelengths that are much larger than the transverse dimensions. Upon deflection, there will be regions inside the rod where the material is stretched and some where it is compressed. Those regions are separated by a neutral surface where the strain is zero, compare figure 2.2**b)**. Small transverse dimensions and small deflections asure that the local strain within a cross-sectional plane can be linearized with respect to the distance from this neutral surface. From the geometric sketch in figure 2.2**b)**, we find for the local deformation

$$\mathrm{d}l'/\mathrm{d}l = (R_{\mathrm{CUR}} - \tilde{y})/R_{\mathrm{CUR}}\,, \tag{2.1}$$

where $\mathrm{d}l$ is the height of a small length element along the rod and $\mathrm{d}l'$ is the local distance between the top and botton cross-section when that element is deformed. $R_{\mathrm{CUR}} = 1/y''$ is the local curvature radius and $\tilde{y}$ is the in plane co-ordiante parallel to the direction of deflection so that

$$u_{xx}(\tilde{y}) = \frac{\mathrm{d}l' - \mathrm{d}l}{\mathrm{d}l} = \tilde{y}y''\,, \tag{2.2}$$

with the local strain $u_{xx}(\tilde{y})$ in the longitudinal direction.

The harmonic description is based on considering only the bending energy of the rod, which is usually perfectly valid for small deflections. The energy density is given by

$$\frac{\mathrm{d}E}{\mathrm{d}V} = \frac{1}{2}Y u_{xx}(\tilde{y})^2\,, \tag{2.3}$$

so that we find the Lagrangian for the deflectional motion

$$\mathcal{L}(y(x,t)) = \frac{\mu}{2}\int \mathrm{d}x\dot{y}^2 - V_{\mathrm{b}}[y(x)]\,, \tag{2.4}$$

with a kinetic part as well as the bending energy

$$V_{\mathrm{b}}[y(x)] = \frac{1}{2}\int \mathcal{F}\kappa^2(y'')^2\mathrm{d}x\,. \tag{2.5}$$

The *linear modulus* or *compressional rigidity* $\mathcal{F} = YA$ of the rod is given by the Young's modulus Y of the material times the cross-section area A. The *area rigidity* $\kappa^2 = \frac{1}{A}\int_{\mathrm{cross}} \tilde{y}^2\mathrm{d}A$ is given by the *second moment of area* I_y divided by the cross-section area A. It is also equal to the ratio of *bending rigidity* YI_y to compressional

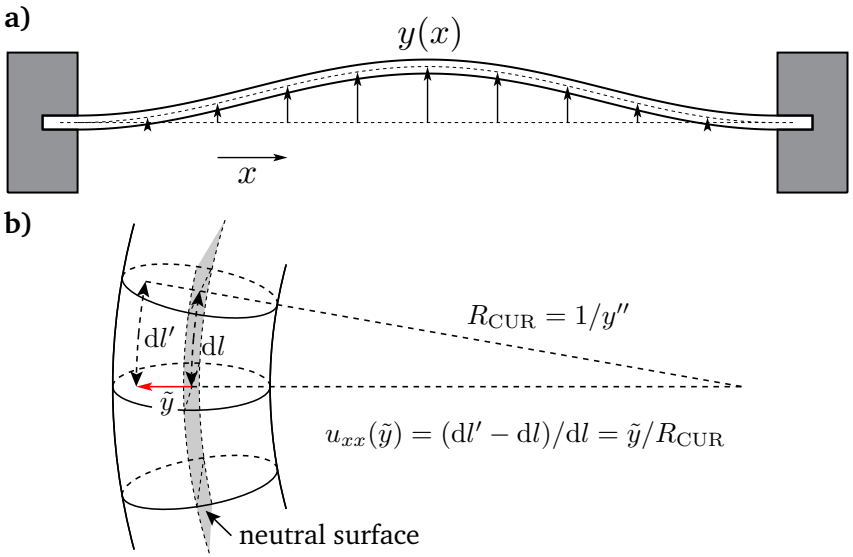

Figure 2.2: **a)**: Sketch of a doubly-clamped beam with deflection described by displacement field $y(x)$. **b)** Local deformation of a deflected rod. The local strain u_{xx} is given by the distance to the neutral surface $\tilde{y}$ and the local curvature y'' and determines the energy density $\mathrm{d}E/\mathrm{d}V = \frac{1}{2}Yu_{xx}^2$.

rigidity. The area rigidity depends on the shape of the cross-section, such that we find $\kappa = d/\sqrt{12}$ for a rectangular cross-section of thickness d and $\kappa = R/2$ for a circular cross-section of radius R. For the implementation of the nanobeam with a carbon nanotube which will be considered later, the cross-section collapses to a circle of radius R. By imposing a small wall width δ, we find $\kappa = R/\sqrt{2}$ for $\delta \to 0$.

The Lagrangian 2.4 leads to the equation of motion

$$\mu\partial_t^2 y + \mathcal{F}\kappa^2\partial_x^4 y = 0\,. \tag{2.6}$$

As this equation is linear in y and its derivatives, it leads to harmonic dynamics. The implementation introduced later is best decribed by clamped boundary conditions $y'(0) = y'(L) = 0$ for the rod. In that case (2.6) has the eigenmodes

$$\phi_n(x) = \frac{1}{C_n}\left[\frac{\sin(\nu_n x/L) - \sinh(\nu_n x/L)}{\sin(\nu_n) - \sinh(\nu_n)} - \frac{\cos(\nu_n x/L) - \cosh(\nu_n x/L)}{\cos(\nu_n) - \cosh(\nu_n)}\right], \tag{2.7}$$

with frequencies

$$\omega_n = c_{\mathrm{s}}\kappa\left(\frac{\nu_n}{L}\right)^2\,, \tag{2.8}$$

where $c_{\mathrm{s}} = \sqrt{\mathcal{F}/\mu}$ is the phase speed of compressional phonons along the rod. The ν_n are the roots of the transcendental equation $\cos(\nu_n)\cosh(\nu_n) = 1$, i.e. $\nu_1 = 4.73$. The C_n are normalization constants chosen such that $\mathbf{max}\{\phi_n(x)\} = 1$. We choose this normalization so that the coefficients in a mode expansion represent the maximum amplitudes of the deflection associated to each mode. With this normalization,

the mode functions satisfy

$$\mu \int_0^L \phi_n(c)\phi_m(x)\mathrm{d}x = \delta_{nm} m_n^* \,, \tag{2.9}$$

where the m_n^* are the effective mode masses. Numerical values for the lowest few mode masses can be found in table A.2 in appendix A.1. Note that in [30], hinged-hinged boundary conditions ($y''(0) = y''(L) = 0$) have been asumed in contrast to the choise presented here, which leads to modes of shape $\sim \sin(n\pi/L)$ with frequencies $\propto (n\pi/L)^2$, where n counts the modes that all have mass $m^* = L\mu/2$. This however again does not correspond to the physical realisation considered later.

We now introduce the canonical momentum $\Pi(x,t) = \delta\mathcal{L}/\delta\dot{y}(x,t)$, as well as the expansion of the field into the modes

$$y(x,t) = \sum_n \phi_n(x)\mathcal{X}_n(t) \,, \tag{2.10}$$

which yields the Hamilton function of a harmonic oscillator for each mode

$$\mathcal{H}_{\mathrm{lin}} = \sum_n \left(\frac{\mathcal{P}_n^2}{2m_n^*} + \frac{1}{2} m_n^* \omega_n^2 \mathcal{X}_n^2 \right) \tag{2.11}$$

with the deflection $\mathcal{X}_n$ and mode momentum $\mathcal{P}_n = m_n^* \partial_t \mathcal{X}_n$ for the n-th mode.

2.2.2 Nonlinear Extension

We now introduce corrections to this harmonic description by considering dynamical stretching of the rod. Any nonzero displacement field $y(x)$ changes the length of the rod from the undeflected length L to a dynamical length L_t with

$$L_t = \int_0^L \sqrt{1 + (y')^2}\mathrm{d}x \approx L + \frac{1}{2}\int_0^L (y')^2 \mathrm{d}x \,, \tag{2.12}$$

where we have used $y' \ll 1$ for small deflections. Therefore the rod experiences a (uniform) longitudinal strain $u_{xx} = (L_t - L)/L$ with energy

$$V_{\mathrm{s}}[y'(x)] = \frac{1}{2}\int_0^L \mathrm{d}x \int \mathrm{d}A \left(Y u_{xx}^2 \right) = \frac{\mathcal{F}}{8L} \left(\int_0^L (y')^2 \mathrm{d}x \right)^2 \,. \tag{2.13}$$

This energy cost leads to a restoring force that is $\mathcal{O}\left(\mathcal{X}^3\right)$ in the deflection and therefore leads to anharmonic dynamics. Inserting the mode expansion (2.10) and adding this part to the Hamiltonian (2.11), we arive at the nonlinear Hamiltonian

$$\mathcal{H} = \mathcal{H}_{\mathrm{lin}} + \frac{\mathcal{F}}{8L} \sum_{i,j,k,l} M_{ij} M_{kl} \mathcal{X}_i \mathcal{X}_j \mathcal{X}_k \mathcal{X}_l \,, \tag{2.14}$$

where $M_{ij} = \int_0^L \phi_i'(x)\phi_j'(x)\mathrm{d}x$. Note that the nonlinearity leads to a coupling of the harmonic modes as the dynamical stretching appears for all motional modes. However, for small enough amplitudes, this effect can be small enough to justify the isolated treatment of the fundamental mode, which then reads

$$H_{\mathrm{m},0} = \frac{\mathcal{P}^2}{2m^*} + \frac{1}{2}m^*\omega_{\mathrm{m},0}^2\mathcal{X}^2 + \frac{\beta}{4}\mathcal{X}^4\,, \tag{2.15}$$

where we introduced the fundamental frequency $\omega_{\mathrm{m},0}$ and the effective mass of the fundamental mode $m^* \approx 0.3965\,\mu L$. The anharmonicity is given by

$$\beta = \frac{(M_{11}L)^2}{2\nu_1^4\,(m^*/\mu L)}\,m^*\frac{\omega_{\mathrm{m},0}^2}{\kappa^2} \approx 0.060\,m^*\frac{\omega_{\mathrm{m},0}^2}{\kappa^2}\,. \tag{2.16}$$

To estimate the strength of the nonlinearity in that classical description, one can compare the contributions to the restoring force $(\partial/\partial\mathcal{X})\,V(\mathcal{X})$. Using (2.16) we find that the ratio of harmonic contribution to nonlinear contribution is given by

$$\frac{F_{\mathrm{nonlin}}}{F_{\mathrm{harm}}} \approx 0.060\left(\frac{\mathcal{X}}{\kappa}\right)^2\,, \tag{2.17}$$

so that the anharmonic corrections are expected to become important if the amplitude $\mathcal{X}$ approches the transverse dimension of the rod given by κ. In principle, this regime can of course always be reached by driving the nanobeam to large amplitudes. However, we are interested in the anharmonic quantum dynamics of the rod and we will particulary concentrate on the few excitation regime, which in terms of deflectional amplitudes usually translates into $\mathcal{X} \ll \kappa$. To understand how the nonlinear contributions can be still important in that regime, we need to consider the quantized model of the system. The later will be introduced in the next section where the strength of nonlinearity will be characterised in terms of contributing energy scales in the spectrum.

2.3 Quantization of modes

In order to estimate the effect of the nonlinear contribution to the energy spectra of the modes, we now turn to the quantum model of the anharmonic nanoresonator. We quantize Hamiltonian (2.14) in the usual way by introducing bosonic mode operators $c_n^\dagger$ and c_n, given by

$$c_n = \frac{1}{2x_{\mathrm{ZPM},n}}\,\mathcal{X}_n + \frac{\mathrm{i}}{\hbar}x_{\mathrm{ZPM},n}\,\mathcal{P}_n\,, \tag{2.18}$$

satisfying the bosonic commutator relations

$$\left[c_m, c_n^\dagger\right] = \delta_{nm}\,. \tag{2.19}$$

Here we introduced the zero point motion amplitudes $x_{\mathrm{ZPM},n} = \sqrt{\hbar/2m_n^*\omega_n}$ for each mode. This leads to the quantum Hamiltonian

$$\mathcal{H} = \sum_n \hbar\omega_n c_n^\dagger c_n + \sum_{ijkl} \hbar\lambda_{ijkl}^0 \left(c_i^\dagger + c_i\right)\left(c_j^\dagger + c_j\right)\left(c_k^\dagger + c_k\right)\left(c_l^\dagger + c_l\right) , \tag{2.20}$$

with the quantum nonlinearity coefficients

$$\lambda_{ijkl}^0 = \frac{\mathcal{F}}{8L\hbar} M_{ij} M_{kl} x_{\mathrm{ZPM},i} x_{\mathrm{ZPM},j} x_{\mathrm{ZPM},k} x_{\mathrm{ZPM},l} \, . \tag{2.21}$$

The nonlinear part couples modes of the same parity, where the coupling strength is given by the nonlinearity. However, for the parameters considered later, the effects of this coupling on the fundamental mode can be negelected, owing to low ambient temperatures where higher modes are in or close to the groundstate. A more detailed analysis of the coupling effects are given in A.1.

Restricting the dynamics to the fundamental mode yields the quantized version of (2.15)

$$H_{\mathrm{m},0} = \hbar\omega_{\mathrm{m},0} b^\dagger b + \hbar\frac{\lambda_0}{2}\left(b^\dagger + b\right)^4 , \tag{2.22}$$

where we have adapted $b^{(\dagger)} = c_1^{(\dagger)}$ as the operator for the fundamental mode. Comparing also to the classical fundamental mode description (2.15) we find

$$\lambda_0 = 2\lambda_{1111}^0 = \frac{\beta}{2} x_{\mathrm{ZPM}}^4/\hbar \, . \tag{2.23}$$

The additional index '0' in the frequencies $\omega_{\mathrm{m},0}$ and the nonlinearity parameter λ_0 refers to the *untuned* resonator, which means those quantites only result from the intrinsic elastic forces without any external forces applied to the resonator. In this case, we find $\lambda_0 \lll \omega_{\mathrm{m},0}$ for most of the physical realisations of nanomechanical resonators commonly used in many experiments. For example for a $500\ \mathrm{nm} \times 20\ \mathrm{nm} \times 10\ \mathrm{nm}$ diamond bar we find $\omega_{\mathrm{m},0} = 1.93\ \mathrm{GHz}$ and $\lambda_0 = 2.83\ \mathrm{Hz}$, which is typical for bulk resonators at that scale. However, there are possibilities to enhance the nonlinearity by tuning the resonance frequency of the nanoresoantor. If the resonator is tuned to lower frequencies $\omega_{\mathrm{m},0} \to \omega_{\mathrm{m}}$ by applying appropriate external forces, the zero point motion of the resonator increases and so does the nonlinearity $\lambda_0 \to \lambda \propto x_{\mathrm{ZPM}}^4 \propto \omega_{\mathrm{m}}^{-2}$. The frequencies ω_{m}, λ shall than refer to the *tuned* resonator.

In the next section, a tuning technique using electrostatic fields will be introduced in detail.

2.4 Tuning and driving via gradient forces

Appling oszillating and stationary electric fields to manipulate and control devices or physical systems on the nanoscale is a very common tool in experimental quantum

physics. Examples reach from creating trapping potentials for single ions, molecules and larger systems like BECs, over optical tweezers to grep dielectric nanoparticels to electrostatic fields, where the field gradient exerts forces onto dielectric materials. The later are called gradient forces, as a constant electric field will have no effect on an uncharged dielectric body. The majority of nanomechanical resonators is fabricated from dieletric materials like for example Si, SiN or diamond. Here, we describe the effect of suitably conducted electrostatic and radio-frequency gradient fields, which are used to tune the resonator and, beyond that, to exert time dependend driving forces.

We consider a pair of tip electrodes that are placed close to the resonator, at each side within the deflectional plane, see figure 2.3. The electrostatic energy associated with the electric fields per unit length along the rod is given by

$$W(x,y) = -\frac{1}{2}[\alpha_{\parallel} E_{\parallel}^2(x,y) + \alpha_{\perp} E_{\perp}^2(x,y)]\,, \tag{2.24}$$

where x, y are the co-ordinates along the resonator axis and the direction of its deflection. $E_{\parallel,\perp}$ are external field components parallel and perpendicular to the beam axis and $\alpha_{\parallel,\perp}$ the respective screened polarizabilities. Note the minus sign in $W(x,y)$ which says that the gradient force points towards stronger fields. We expand $W(x,y)$ to second order in the displacement y (compare Appendix A.2) and get an additional contribution to the Hamiltonian of the nanobeam that reads

$$\begin{aligned} V_{\mathrm{el}} =& V_{\mathrm{el}}^{(1)} + V_{\mathrm{el}}^{(2)} \\ =& \int_0^L \left[\left.\frac{\partial W}{\partial y}\right|_{y=0} y + \frac{1}{2} \left.\frac{\partial^2 W}{\partial y^2}\right|_{y=0} y^2 \right] \mathrm{d}x\,, \end{aligned} \tag{2.25}$$

where we dropped the displacement independent constant $W(x,0)$ which is irrelevant for the dynamics. Inserting the modes defined in equation (2.10) we get

$$V_{\mathrm{el}} = \sum_n F_n \mathcal{X}_n + \frac{1}{2} \sum_{lk} W_{lk} \mathcal{X}_l \mathcal{X}_k\,, \tag{2.26}$$

with

$$F_n = \int_0^L \partial_y W(x,y)\big|_{y=0}\, \phi_n \mathrm{d}x\,, \tag{2.27}$$

$$W_{lk} = \int_0^L \partial_y^2 W(x,y)\Big|_{y=0}\, \phi_l \phi_k \mathrm{d}x\,. \tag{2.28}$$

The second order coefficients W_{lk} induce a weak coupling between modes of same parity. Diagonalizing the combined quadratic potential $V_{\mathrm{b}} + V_{\mathrm{el}}^{(2)}$, we find that the main effect is that the fundamental eigenfrequency is reduced to a smaller frequency,

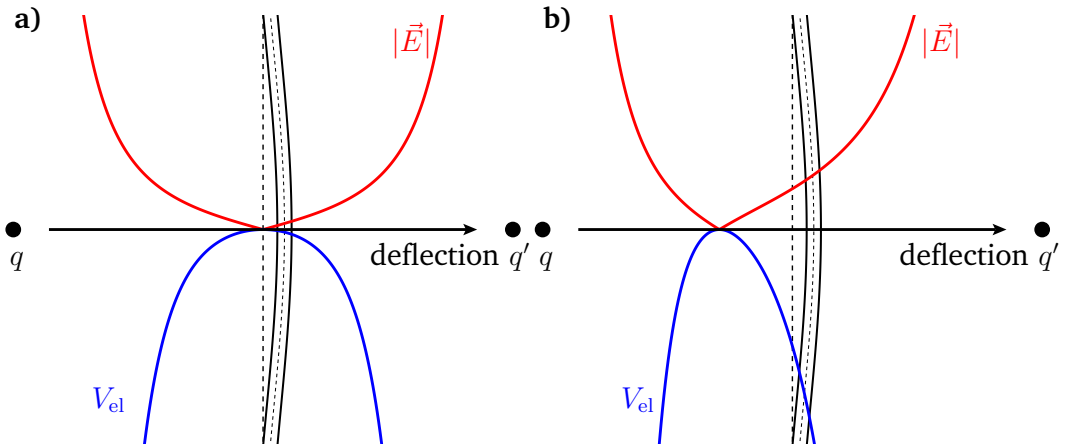

Figure 2.3: Resonator with electrodes modeled by point charges q, q'. **a)** $|q| = |q'|$: The field profile (red) leads to an inverted parabola for the dielectric potential (blue) around the equilibrium position. This potential effectively reduces the mode frequency. **b)** $|q| \neq |q'|$ At the position of the resonator, the lowest order of the dielectric potential is linear, corresponding to external drive force.

see Appendix A.2. The higher mode frequencies are significantly less reduced and corrections to the eigenmodes are found to be small enough to be neglected. This allows us again to focus on the fundamental mode contributions F_1 and W_{11} with $W_{11} < 0$. It is convenient for later purposes to divide the dielectric potential into static and time dependent parts, both for the first order and the second order contributions

$$F_1 = F_1^{\mathrm{s}} + F_1(t) \tag{2.29}$$
$$W_{11} = W_{11}^{\mathrm{s}} + W_{11}(t)\,. \tag{2.30}$$

The time dependend contributions can be used to apply temporary forces onto the resonator, for example driving pulses, which will come to use and will be explained in part 5. The static contributions will be used to tune the resonator. Here, the contribution of W_{11}^{s} leads to the aforementioned reduction of the fundamental frequency

$$\omega_{\mathrm{m}}^2 \approx \omega_{\mathrm{m},0}^2 - \frac{|W_{11}^{\mathrm{s}}|}{m^*}\,. \tag{2.31}$$

We shall refer to this effect as *softening*, since a lower frequency corresponds to a rod with lower elastic modulus Y. Consequently, we want to introduce a quantity called the *softening factor* $\zeta = \omega_{\mathrm{m},0}/\omega_{\mathrm{m}}$, which describes the relative amount of frequency reduction and is useful to analyze the scaling of other physical quantities that change upon softening. Note that for $|W_{11}^{\mathrm{s}}| > m^*\omega_{\mathrm{m},0}^2$, we enter the bistable regime, or buckling regime, for the the nanobeam.

The contribution of F_1^{s} leads to a static deflection, or a shift of the equilibrium position of the nanobeam. In the next chapter, we will introduce a setup where a

nanobeam interacts with the photon field of an optical cavity. A side effect of this interaction is a similar static deflection caused by radiation pressure of the photon field. In that case, the force F_1^{s} can be chosen such that this unwanted effect is compensated and the nanobeam remains undeflected.

The fundamental mode Hamiltonian including both static contributions is then given by

$$H_{\mathrm{m}} = \frac{\mathcal{P}^2}{2m^*} + \frac{1}{2}m^*\omega_{\mathrm{m}}^2\mathcal{X}^2 + \frac{\beta}{4}\mathcal{X}^4\,, \tag{2.32}$$

which from now on will be refered to as the *tuned* Hamiltonian. In a phononic description, this Hamiltonian reads

$$H_{\mathrm{m}} = \hbar\omega_{\mathrm{m}} b^\dagger b + \hbar\frac{\lambda}{2}(b^\dagger + b)^4\,, \tag{2.33}$$

where the nonlinearity $\lambda = \zeta^2\lambda_0$ is now increased by a factor ζ^2 compared to the untuned resonator (2.22). More generally, we find

$$\lambda_{ijkl} = \sqrt{\zeta_i\zeta_j\zeta_k\zeta_l}\,\lambda^0_{ijkl}\,, \tag{2.34}$$

where ζ_i is the softening factor for mode i and usually $\zeta_i \approx 1$ for $i > 1$, compare figure A.2. This can be easily understood with the increase of the zero point motion x_{ZPM} by a factor $\sqrt{\zeta}$ for any mode. Note that within the given expansion of the electric field energy, the classical nonlinearity parameter β does not change upon softening.

For $\zeta \gg 1$, it is convenient to express all mechanical observables in the energy eigenbasis of (2.33), so that

$$H_{\mathrm{m}} = \sum_n E_n|n\rangle\langle n|\,, \qquad \mathcal{X} = \sum_{nm} X_{nm}|n\rangle\langle m|\,, \tag{2.35}$$

where the energy eigenstates $\{|n\rangle\}$ and energy levels E_n, as well as the displacement matrix elements X_{nm} need to be determined numerically. In this regime, λ is not necessarily a good measure for the physical nonlinearity, since λ diverges for $\zeta \to \infty$. The physical nonlinearity is the mismatch of the transition frequencies $\delta_{21} - \delta_{10}$, where $\delta_{nm} = E_n - E_m$. This quantity shows the ζ^2-dependency as long as $\lambda \ll \omega_{\mathrm{m}}$, and saturates at a finite value for $\zeta \to \infty$, compare figure 2.4.

For small nonlinearities $\lambda \ll \omega_{\mathrm{m}}$, which follow from moderate softening factors, an analytical expression can be obtained as the Hamiltonian (2.33) is approximately diagonal in Fock basis. This can be seen by apply a rotating wave approximation in the nonlinear part

$$H_{\mathrm{m}} \to H'_{\mathrm{m}} = \hbar\omega'_{\mathrm{m}} b^\dagger b + \hbar\frac{\lambda'}{2} b^\dagger b^\dagger b b\,, \tag{2.36}$$

where $\omega'_{\mathrm{m}} = \omega_{\mathrm{m}} + 2\lambda'$, $\lambda' = 6\lambda$ and the eigen-energies are given by

$$E_n \approx n\left(\hbar\omega'_{\mathrm{m}}\right) + \frac{n(n-1)}{2}\left(\hbar\lambda'\right)\,. \tag{2.37}$$

In that regime, $\lambda' = \delta_{21} - \delta_{10}$ is the physical nonlinearity of the nanobeam.

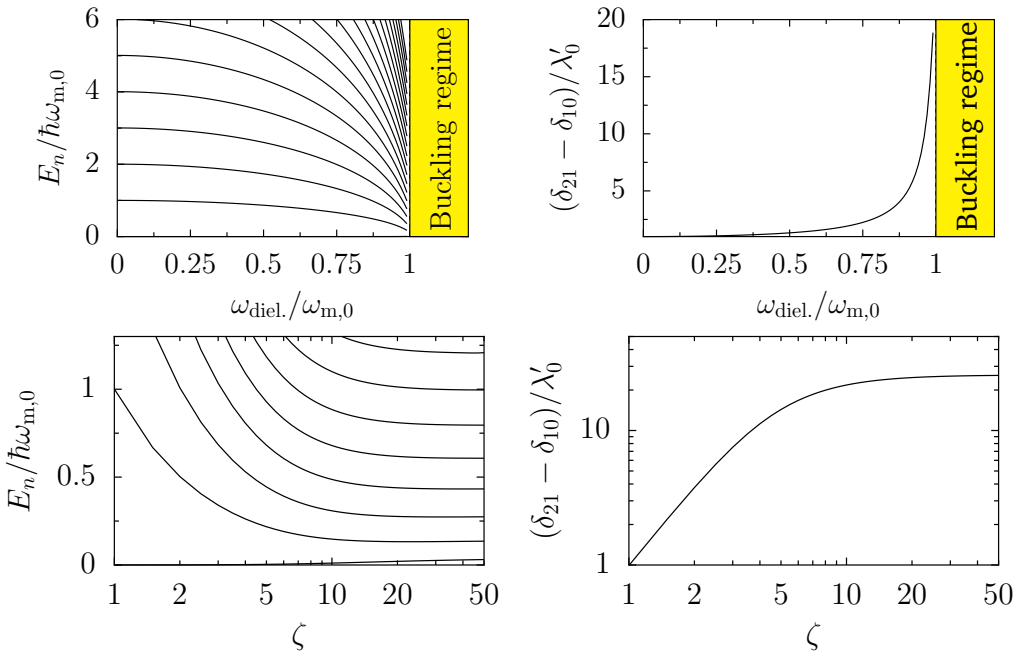

Figure 2.4: Typical spectrum (left column) and physical nonlinearity (right column) plottet vs $\omega_{\mathrm{diel.}} = \sqrt{|W_{11}^{\mathrm{s}}|/m^*}$ which is proportional to the strength of the electric softening field (top row) and vs softening factor ζ (bottom row). While the softening factor ζ, as well as $\lambda = \zeta^2\lambda_0$ diverges for $\omega_{\mathrm{diel.}} \to \omega_{\mathrm{m},0}$, the spectrum saturates towards the solution for a pure X^4-potential. For larger fields, the resonator crosses the buckling instability. The shape of the curves in these plots only depends on the inital ratio $\lambda_0/\omega_{\mathrm{m},0}$, but is otherwise universal. For larger initial nonlinearities, the spectrum saturates faster. Here that initial ratio is $\lambda_0/\omega_{\mathrm{m},0} = 0.32 \times 10^{-3}$, which corresponds to a CNT of 3 μm length (see next chapter).

Chapter 3

Optoelectromechanical setup

3.1 Introduction

In the previous chapter, we have introduced the concept of the anharmonic nanomechanical resonator. In this chapter we want to describe a possible implementation of such a nanoresonator, embedded in an optomechanical setup. This setup constitutes a combination of devices that exist and have been used in experminents. However the combination presented here is novel and demands a careful consideration of certain aspects. The first component is of course a nanomechanical device, which includes the resonator itself, as well as the electrodes for the gradient fields, all integrated into a nanoelectromechnical system (NEMS) on chip. This topic will be described in section 3.2. The second component is a laser driven, high-Q microtoroid optical cavity, described in section 3.3. The nanoresonator can couple to the photons inside the micro toroid via the evanescent part of the photon field, thereby establishing an optomechanical system. The coupling mechanicsm is described in section 3.4. However, the combination of a high-Q optical cavity with conducting electrodes on the NEMS chip nearby has to be investigated with care, since the electrodes may interact with the evanescent photon field. This could lead to large additional photon losses if the setup is designed in an unconvenient way. Aspects of this difficulty are treated in section 3.5.

3.2 CNT and nanoelectromechanical chip

In order to investigate the quantum behaviour of a system, it is usually necessary to keep thermal noise as small as possible. In most cases this means that one prefers a regime where the ratio of environmental temperature to system frequencies $k_{\mathrm{B}}T/\hbar\omega$ is kept as small as possible. This already motivates to fabricate mechanical resonators with high frequencies, up to the GHz domain [31]. This can, for instance, be achieved by using materials with high elasticity and small lengths. In addition, by considering the scaling of the nonlinearity in (A.1), we conclude that the best

option is to use devices with low mass and low transveral dimensions. All those demands are excellently met by carbon nanotubes (CNTs). They feature an enormous stiffness, a quality they share with the corrsponding "bulk material" diamond. They are hollow and thus have a small mass and typical diameters for single walled nanotubes are less then one nanometer. But beyond that, carbon nanotubes can feature very high mechanical Q-factors [32], which is very important to successfully maintain and observe possible quantum behaviour. Interestingly, the Q-factors of CNTs have been found to depend on the ambient temperature, which results from nonlinear damping [33, 34]. This means that the Q-factors at the single phonon level may be even much higher than the Q-factors observed in the experiments.

On the experimental side, CNTs have been succesfully placed on SI-chips, in a way that a fraction is suspended freely over a gap in the substrate, see figure 3.1. This way it was possible to study the mechanical properties of deflectional modes [35, 36, 37, 38]. In [36], tuning of the mechanical resonance frequency using electric fields was already applied, even though the tuning effect results from the fact that the tube is pulled towards the ground plate, which induces tensile strain.

Here, a similar NEMS is proposed as a possible implementation of the system decribed in this work. The nanomechanical chip consists of a single-walled CNT that is mounted on a chip and is spanning over a gap. In addition there are tip electrodes to supply dielectric gradient forces, that may be implemented by conducting nanotubes. The electrodes and the CNT are arranged in a specific geometric alignment within the chip surface, see figure 3.2. This results from optimizing a tradeoff between maximizing optomechanical coupling and avoiding additional losses in the nearby optical cavity. Details of that will be discussed in sections 3.4 and 3.5.

We choose a $(10, 0)$-nanotube with radius $R = 0.39\,\mathrm{nm}$. The phase speed of compressional phonons in such a nanotube is $c_\mathrm{s} = 21 \times 10^3\,\mathrm{m/s}$, so that we find $\omega_{\mathrm{m},0} = 20.6\,\mathrm{MHz}$ and $\lambda_0 = 2.24\,\mathrm{kHz}$ for a tube of one micrometer length. We choose the $(10, 0)$-type, as this type has a relatively high polarizability α. Table 3.1 shows polarizability values for different types of nanotubes that have been taken from [39]. The static polarisabilities for our choice of nanotube are $\alpha_{||} = 143\,\text{Å}^2$ and $\alpha_\perp = 10.9\,\text{Å}^2$, where $\alpha_{||}$ ($\alpha_\perp$) is the polarisability parallel (perpendicular) to the tube axis. The given values are screened polarizabilities per unit length, which have already been used in section 2.4. A high polarizability is needed in order to maximize the sensitivity to tuning fields and the optomechanical coupling introduced in section 3.4. With such a tube implementing the nanomechanical resonator, it is possible to enter the buckling regime by applying softening fields. Figure 3.3**a)** shows a typical profile for electric field strength along the rod axis, while figure 3.3**b)** shows how the field strength reqired to enter the buckling regime depends on the length of nanotube.

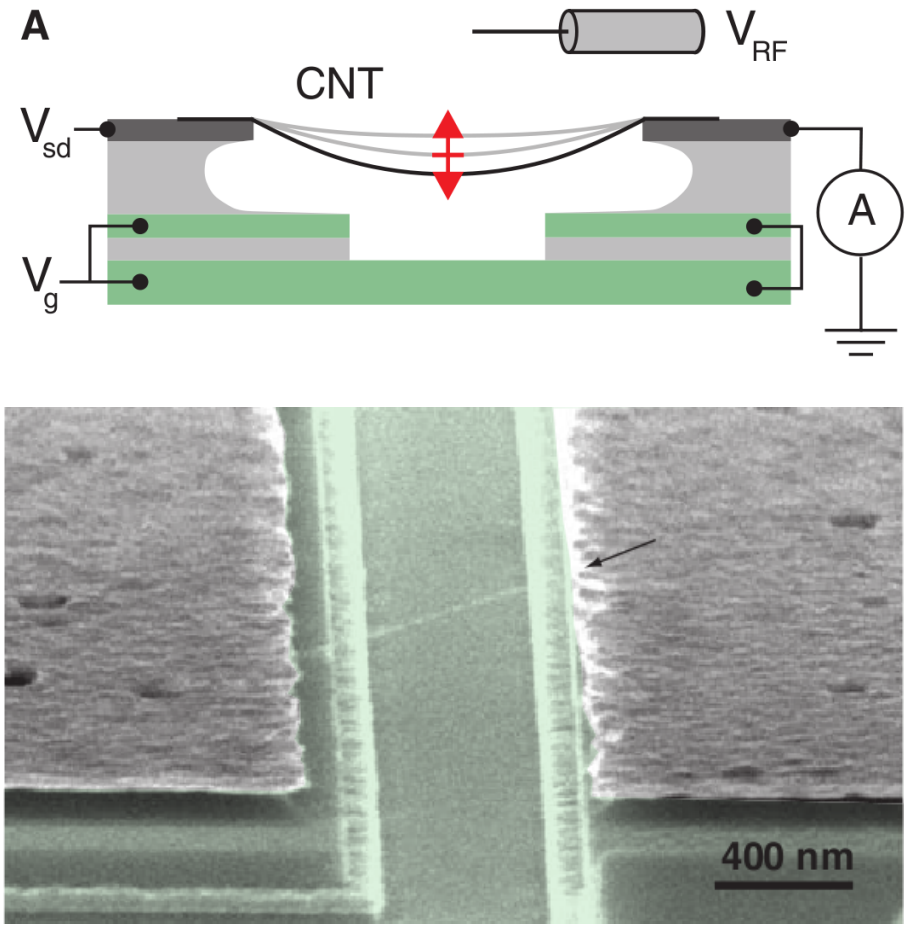

Figure 3.1: Picture of an experiment at Delft University, 2009 [36]: A carbon nanotube suspended over a gap in the substrate. The CNT has been excited into mechanical motion by the rf-field of a nearby antenna. A gate voltage $\mathbf{V}_g$ is used to tune the mechanical resonance frequency. The oscillations have been monitored using a dc current throught the nanotube.

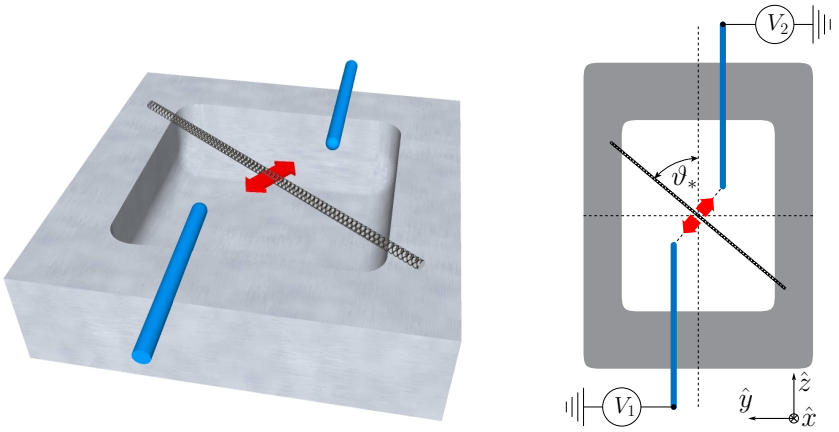

Figure 3.2: Schematic sketch of the NEMS chip. The nanotube's oscillation can be tuned or driven by gradient forces that are produced by the electrodes (blue). The special relative alignment is characterized by the optimized angle ϑ_*, see sections 3.4, 3.5 for details.

(n,m)	R_0 (Å)	Δ_g (eV)	$\alpha_\perp$ (Å^2)	$\alpha_{\|\|}$ (Å^2)
(7,0)	2.73	0.48	6.47	83.0
(8,0)	3.15	0.57	7.80	104
(9,0)	3.58	0.17	9.32	1460
(10,0)	3.95	0.91	10.9	142
(11,0)	4.34	0.77	12.7	186
(12,0)	4.73	0.087	14.3	6140
(13,0)	5.09	0.72	16.3	224
(14,0)	5.48	0.63	18.4	279
(15,0)	5.88	0.041	20.3	11 100
(16,0)	6.27	0.61	22.9	326
(17,0)	6.66	0.53	25.2	395
(8,0)+(17,0)	···	···	25.8	499
(8,0)+(16,0)	···	···	23.6	427
(4,4)	2.71	(0)	6.41	(∞)
(5,5)	3.40	···	8.71	···
(6,6)	4.10	···	11.6	···
(7,7)	4.76	···	8.71	···
(8,8)	5.45	···	14.7	···
(9,9)	6.12	···	21.8	···
(10,10)	6.78	···	26.1	···
(12,12)	8.14	···	35.8	···
(14,14)	9.50	···	47.2	···

Table 3.1: Radius, band gap and transverse and longitudinal polarizabilities (per unit length) of different carbon nanotubess, taken from [39].

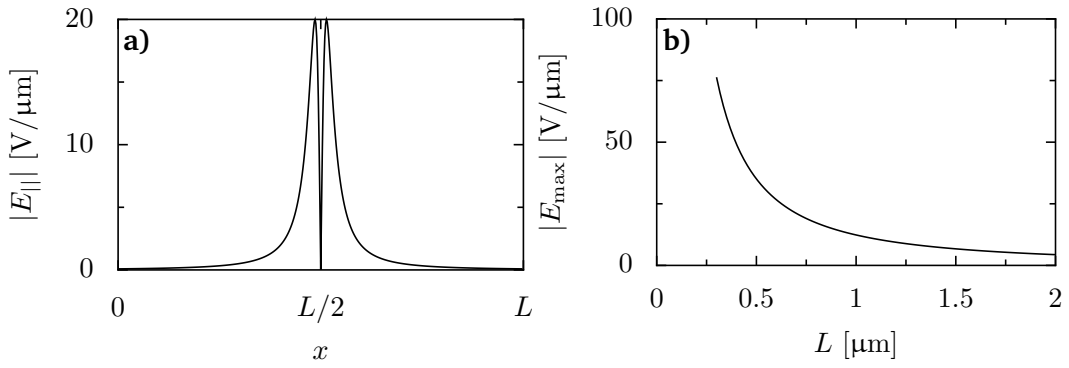

Figure 3.3: Electric fields for softening the fundamental mode: **a)** Typical field profile. Since $\alpha_{||} \gg \alpha_{\perp}$ we choose a configuration with charges $q = q'$ or $\epsilon = 0$, so that the maximum field is displaced from the middle of the nanotube and the field points along the tube axis. **b)** The electric field maxima required to enter the buckling regime, e.g. leading to $\omega_{\text{diel.}} = \omega_{\text{m},0}$, depending on the length of the tube. Here we asumed a distance of $20\ \text{nm}$ between electrodes and tube axis as well as a $(10, 0)$-tube as described in the text.

3.3 Micro toriod cavity

In order to establish an optomechanical system, in addtion to the NEMS, we also need an optical cavity that can be coupled to the nanomechanical motion. Here, we choose a micro toroid optical cavity [40]. This is a resonator, which is essentially a tiny disk with a toroidal shaped rim where the photons travel within a whispering gallery mode (WGM) around the rim, see figure 3.4. These kind of optical resonators feature very high Q-values at low optical mode volumes [41], which is favourable for many applications. The cavity is driven by a laser field that is usually guided to the cavity with an optical fiber. The fiber is tapered to a smaller diameter to asure efficient coupling between fiber mode and cavity mode. This way the fiber-WGM coupling rate κ_{ex} can by far exceed other photon loss mechanicsm [42]. But the most important feature is that the supported photon modes, similar to an optical fiber, have an evanescent field fraction outside the rim. This provides a relatively elegant way to establish coupling to different (quantum) systems via that evanescent field [40, 43, 44], which for our NEMS system will be described in the next section.

The spacial shape of the evanescent field can be locally described by modelling the rim as a straight cylindrical wave guide with radius a_{c}. This approxiamtion is good as long as the size of the object interacting with that field is considered to be much smaller than the cavity. We introduce cylindrical co-ordiantes (r, ϕ, z) associated with the wave guide and consider $\text{TE}_{0,n}$ modes, as a transverse electric field is advantagous regarding possible unwanted interaction with the NEMS electrodes,

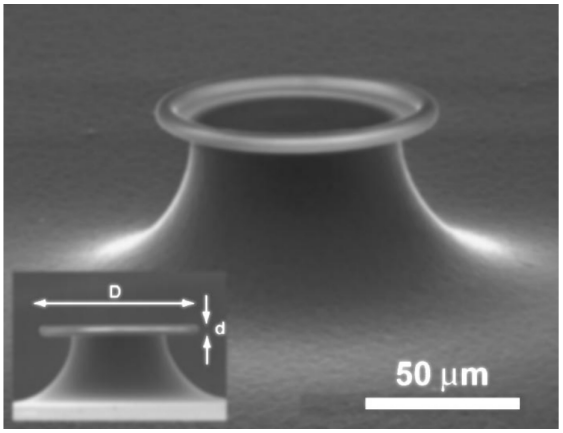

Figure 3.4: Left: Scanning-electron-microscopy image of a toroid micro cavity. Picture taken from [41]. Right: To view of a toroid micro cavity with an optical fiber. Picture taken from `http://quantumoptics.caltech.edu/qoptics_old/index.html`

compare section 3.5. The corresponding transverse fields inside and outside the rim are given by [45]

$r < a_\mathrm{c}$:

$$B_r = -\mathrm{i}\frac{k_{||}}{\gamma^2}\frac{\partial B_z}{\partial r}\,, \tag{3.1}$$

$$E_\varphi = -\frac{\omega}{k_{||}}B_r\,, \tag{3.2}$$

$r > a_\mathrm{c}$:

$$B_r = -\mathrm{i}\frac{k_{||}}{\kappa_\perp^2}\frac{\partial B_z}{\partial r}\,, \tag{3.3}$$

$$E_\varphi = -\frac{\omega}{k_{||}}B_r\,, \tag{3.4}$$

The axial field reads

$$B_z(r,z) = B_z(0)J_0(\gamma r)\mathrm{e}^{\mathrm{i}k_{||}z}\,, \qquad r < a_\mathrm{c}\,, \tag{3.5}$$

$$B_z(r,z) = \tilde{\xi}B_z(0)\frac{K_0^{(1)}(\kappa_\perp r)}{K_0^{(1)}(\kappa_\perp a_\mathrm{c})}\mathrm{e}^{\mathrm{i}k_{||}z}\,, \qquad r > a_\mathrm{c}\,, \tag{3.6}$$

with the modified Bessel function $K_0^{(1)}$ and the Bessel function of first kind J_0. $k_{||}$ is the wavevector component parallel to the waveguide axis and γ and $\kappa_\perp$ are the transverse wave vectors inside and outside the waveguide, respectively. The wavevectors have to satisfy

$$k_{||}^2 - \kappa_\perp^2 = \left(\frac{\omega}{c}\right)^2 \tag{3.7}$$

$$k_{||}^2 + \gamma^2 = n_\mathrm{c}^2\left(\frac{\omega}{c}\right)^2 \tag{3.8}$$

The ratio of the field maximum inside the waveguide to the field at $r = a_\mathrm{c}$ is given by $\tilde{\xi} = B_z(a_\mathrm{c})/B_z(0) \approx 0.4$ if $a_\mathrm{c}\gamma$ coincides with the first zero of $J_1(x)$, which is

$a_c\gamma \approx 3.8$. We further approximate the evanescent electric field for $r > a_c$, using $2\kappa_\perp a_c \gg 1$ and assume a frequency well above cutoff, so that $k_{||} \approx n_c k \gg 1/a_c$. With these approximations, the evanescent field can be written

$$E_\varphi(r) \approx -\mathrm{i}\frac{\omega}{\kappa_\perp}\tilde{\xi}B_z(0)\sqrt{\frac{a_c}{r}}\mathrm{e}^{-\kappa_\perp(r-a_c)}\mathrm{e}^{\mathrm{i}nkz}\,. \tag{3.9}$$

This expression for the evanescent field will be used for further calculations in the next sections. Typical parameters values for the silica toroids considered here, are the index of refraction of silicia $n_c = 1.44$, an optical wavelength $\lambda_c \approx 1.1\ \mu\mathrm{m}$, a rim radius $a_c = 1.4\ \mu\mathrm{m}$ and the evanescent decay length $2\pi/\kappa_\perp \approx (2\pi c/\omega)/\sqrt{n_c^2 - 1} \approx \lambda_c$.

3.4 Optomechanical coupling

The optomechanical coupling between the NEMS and the micro toroid is achieved by placing the NEMS chip close to the cavity rim, inside the evanescent field. The nanoresonator, as a dielectric subject to an external field, contributes an energy that depends on the field strength. As the evanescent field decays exponentially with distance to the rim, a displacement of the nanosoesonator results in a change of energy. That change of energy can be interpreted as a shift of the cavity frequency, which describes the influence of the nanoresonator onto the cavity dynamics, or as an additional force acting on the nanoresoantor, which describes the backaction of the cavity onto the resonator. To obtain the standart dispersive optomechanical coupling, this energy is linearized about the equilibrium of the position of the nanoresonator.

The dielectric energy of the nanoresonator inside an electric field is given by

$$H_c = -\frac{1}{2}\int \vec{P}(\vec{r})\cdot\vec{E}(\vec{r})\mathrm{d}V\,, \tag{3.10}$$

with the polarization $\vec{P}(\vec{r}) = \overleftrightarrow{\alpha}\cdot\vec{E}(\vec{r})$ of the nanoresonator, $\overleftrightarrow{\alpha}$ the screened polarizability tensor and $\vec{E}$ the external field. The integration is taken over the resonator volume. For our implementation with a CNT, $\overleftrightarrow{\alpha} \equiv \mathrm{diag}\{\alpha_{||}, \alpha_\perp\}$ and $\vec{P}(\vec{r})$ is the total polarization of the crossection at $\vec{r}$ and the integration is taken along the nanotube axis instead.

In order to estimate the strength of optomechanical coupling, we consider the quantized electric field, which in the evanescent part is directed along $\hat{\varphi}$

$$\vec{E}(\vec{r}) = \sqrt{\frac{\hbar\omega_c}{2\epsilon_0}}(a^\dagger + a)U(r)\hat{\varphi}\,, \tag{3.11}$$

where we introduced photon creation and annihilation operators $a^\dagger$ and a as well as the normalized photon shape

$$U(r) = \sqrt{\frac{\epsilon(r)|\vec{E}(r)|^2}{\int \mathrm{d}\vec{r}'\epsilon(r')|\vec{E}(r')|^2}}\,. \tag{3.12}$$

We also introduce the optical mode volume

$$V_{\mathrm{mode}} = \int \mathrm{d}V \frac{|\vec{E}(r)|^2}{|\vec{E}_{\mathrm{max}}|^2}\,, \tag{3.13}$$

but neglect the small contribution of the evanescent part by integrating over the rim volume only. With the electric field solution given in (3.2) we find for the field maximum

$$|\vec{E}_{\mathrm{max}}| = \frac{\omega}{\gamma} B_z(0) J_1\left(\gamma \frac{a_{\mathrm{c}}}{2}\right) \approx \frac{\omega}{\gamma} \frac{B_z(0)}{1.72}\,, \tag{3.14}$$

so that the shape of the photon mode can be expressed as

$$U(r) \approx \frac{1.72\,\xi}{n_{\mathrm{c}}\sqrt{V_{\mathrm{mode}}}} \sqrt{\frac{a_{\mathrm{c}}}{r}}\, \mathrm{e}^{-\kappa_\perp (r - a_{\mathrm{c}})}\,. \tag{3.15}$$

For the mode volume we find $V_{\mathrm{mode}} \approx 0.5\,\pi a_{\mathrm{c}}^2 L_{\mathrm{c}}$ and $1.72\,\xi$ is the ratio of the field at the waveguide surface to the maximum electric field inside the waveguide with $\xi = (\gamma/\kappa_\perp)\,\tilde{\xi}$.

We insert the quantized electric field (3.11) into the Hamiltonian (3.10) and apply a linearization of $U^2(r)$ around the equilibrium position of the nanoresonator. This linearization is valid since the typical deflectional amplitude of the nanoresonator on the order of the zero point motion x_{ZPM} is much smaller than the evanesent decay length $1/\kappa_\perp$. We also neglect the deflectional mode shapes of the resonator and for convenience asume the same field for entire nanobeam volume, so that the integration along the tube axis directly translates into the nanotube length L_{tube}. Thus, by comparing the result to (1.1), we extract the optomechanical coupling rate

$$G_0 \approx 3.0\, \frac{\omega_{\mathrm{c}} \alpha_{||} \kappa_\perp L_{\mathrm{tube}} \xi^2}{n_{\mathrm{c}}^2 \epsilon_0 V_{\mathrm{mode}}} \mathrm{e}^{-2\kappa_\perp d} C_{\mathrm{corr}}\,. \tag{3.16}$$

Here, we also neglected the contribution of the perpendicular fields since $\alpha_\perp \ll \alpha_{||}$. The geometric alignment of nanotube has been accounted for in the correction factor C_{corr}, where $C_{\mathrm{corr}} = 1$ would correspond to situation where the nanotube is aligned along the electric field vector, and the direction of deflection is aligned in radial direction, which is the along the electric field gradient. However, the deflectional plane for the fundamental mode of the nanoresonator is the plane of the NEMS chip surface, which at the point of closest distance d is necessarily the tangential with respect to the rim co-ordinates, compare figure 3.5. To still achieve linear coupling, the resonator has to be displaced from the closest point, which is described by the angle φ and the actual distance is $d' = (a_{\mathrm{c}} + d)/\cos\varphi - a_{\mathrm{c}}$. The orientation of the nanotube within the NEMS plane is described by the angle ϑ, where $\vartheta = 0$ corresponds to an orientation along the rim axis $\hat{z}$. It is helpful to introduce the relevant directions, which are the alignment of the nanotube $\hat{e}_{\mathrm{tube}}$, the direction of

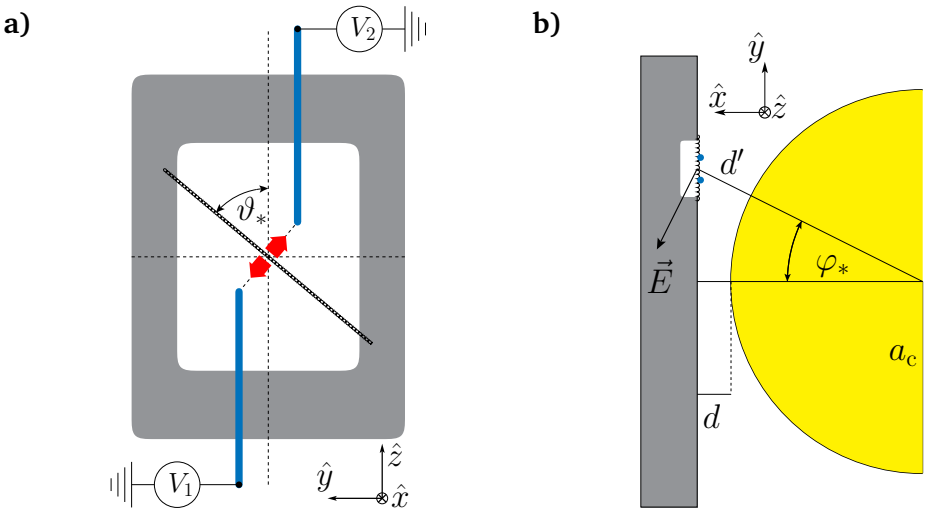

Figure 3.5: Geometrical arrangement of the setup. **a)** The orientation of the nanotube within the chip plane. **b)** The position of the resonator has to be displaced from the point of closest distance to the cavity wave guide (yellow) d to d' to allow for linear coupling. The angles ϑ_*, φ_* are optimized to maximize the optomechanical coupling rate.

its deflection $\hat{e}_{\text{defl.}}$ and the directions $\hat{\varphi}$ and $\hat{r}$ of the evanescent field and its gradient,

$$\hat{e}_{\text{tube}} = \sin\vartheta\hat{y} + \cos\vartheta\hat{z}\,, \tag{3.17}$$
$$\hat{e}_{\text{defl.}} = \cos\vartheta\hat{y} - \sin\vartheta\hat{z}\,, \tag{3.18}$$
$$\hat{\varphi} = -\sin\varphi\hat{x} + \cos\varphi\hat{y}\,, \tag{3.19}$$
$$\hat{r} = \cos\varphi\hat{x} + \sin\varphi\hat{y}\,. \tag{3.20}$$

Now perfect alignment between nanotube and electric field $\hat{e}_{\text{tube}}\cdot\hat{\varphi} = 1$ leads to $\hat{e}_{\text{defl.}}\cdot\hat{r} = 0$ and vice versa. Including the imperfect alignments, the correction factor reads

$$C_{\text{corr}} = \mathrm{e}^{-2\kappa_\perp(d'-d)}\,(\hat{e}_{\text{tube}}\cdot\hat{\varphi})^2\,(\hat{e}_{\text{defl.}}\cdot\hat{r}) \tag{3.21}$$
$$\approx \mathrm{e}^{-2\kappa_\perp(d+a_c)(\sec\varphi-1)}\sin^2\vartheta\cos\vartheta\cos^2\varphi\sin\varphi\,. \tag{3.22}$$

This correction factor is maximized for $\sin^2\vartheta_* = 2/3$ and $\varphi_* \approx 1/\sqrt{2\kappa_\perp(d+a_c)} \approx 0.24$ (see A.3), resulting in $1/C_{\text{corr}} \approx 17.7$ for a refracting index $n_c = 1.44$.

3.5 Setup specific loss mechanisms

3.5.1 Cavity losses induced by NEMS electrodes

In this section, we describe the influence of the NEMS electrodes onto the photon field inside the cavity, regarding possible additional loss channels. As electrodes have to be conducting, it is a natural concern that either absorbtion, which is due to induced currents inside the electrodes, or scattering can have a significant impact on the cavity finesse. Here, we show that for sufficiently good alingment, those effects lead to additional loss rates that are smaller than the intrinsic photon losses that also exist without the electrodes. One crucial aspect is the transverse dimension of the electrodes, which has to be much smaller than the wave length of the evanescent field. This leads to a strong suppression of higher scattering modes of the electrode. We will discusses different possible loss channels, being scattering by the electrodes, dipole scattering by the gap between the two electrodes and absorption in the electrodes. Each of these loss channels can be characterized by a respective finesse $\mathcal{F}_i$, so that by asuming independent channels the total resulting cavity finesse is given by

$$\frac{1}{\mathcal{F}} = \sum_i \frac{1}{\mathcal{F}_i} \,. \tag{3.23}$$

If a calculated finesse $\mathcal{F}_i$ proves to be much larger than the original, intrinsic finesse $\mathcal{F}_0 \sim 10^6$, the corresponding contribution to the cavity losses can be neglected. for each loss channel, the finesse will be determined as the ratio of incident power to lost power, where the later is scattered or aborbed. Therefore we start by formulating the incident fields and the incident power.

Incident field and incident power

We model the electrodes as metallic cylinders of radius R with $R \ll 1/\kappa_\perp$, that are aligned along the axis of the wave guide with a small misalignment angle θ. In addition to the cylindrical co-ordinates (r, ϕ, z) introduced for the wave guide, we now introduce cylindrical co-ordinates (r', ϕ', z') for the electrode, so that $\hat{z} \cdot \hat{z}' = \cos\theta$, see figure 3.6. We express the incident evanescent field (3.9) at the electrode in the electrode co-ordinates, which translates as

$$E^{(\mathrm{in})}_{z'}(z') = \hat{z}' \cdot \hat{\varphi}\; E_\varphi\big|_{r'=0} \,. \tag{3.24}$$

We asume $E^{(\mathrm{in})}_{z'}(z')$ to be constant inside the cross-section of the electrode. This field component along the electrode axis is the only relevant, since the transverse fields are completely determined by the wave equation for the scattering modes. The origin of the prime co-ordinates lies at $(-d - a_\mathrm{c}, 0, 0)$ and directions translate as

$$\hat{z}' \quad = \sin\theta\hat{y} + \cos\theta\hat{z} \tag{3.25}$$

$$\hat{\varphi} \;\; = -\sin\varphi\hat{x} + \cos\varphi\hat{y} \,. \tag{3.26}$$

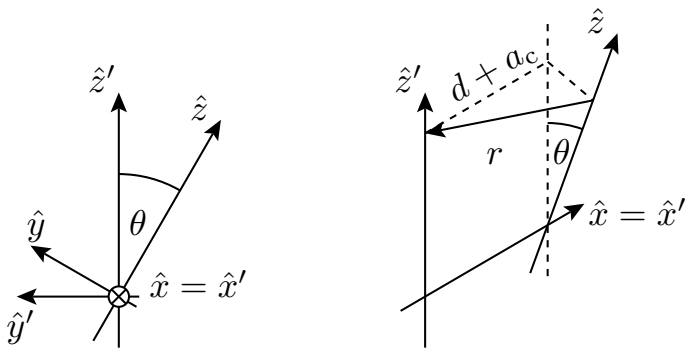

Figure 3.6: Relative orientation of the co-ordinate systems of the wave guide (r, ϕ, z) and the eletrode (r', ϕ', z') .

For points on the electrode, represented by $\hat{z}'$-axis, we find

$$r = \sqrt{(d + a_c)^2 + z'^2 \sin^2\theta}\,, \tag{3.27}$$

$$\cos\varphi = \frac{d + a_c}{r}\,, \tag{3.28}$$

$$z = z' \cos\theta\,. \tag{3.29}$$

For our further calculations it is convenient to express the incident field via its Fourier transform

$$E_{z'}^{(\mathrm{in})}(k') = \int_{-\infty}^{\infty} E_{z'}^{(\mathrm{in})}(z') \mathrm{e}^{-\mathrm{i}k'z'}\,\mathrm{d}z'\,, \tag{3.30}$$

which can be evaluated using an approximation for the Fourier integral (see A.4) to yield

$$E_{z'}^{(\mathrm{in})}(k') \approx \frac{-\mathrm{i}\omega}{\kappa_\perp}\sqrt{\frac{2\pi a_c}{\kappa_\perp}}\tilde{\xi} B_z(0) \mathrm{e}^{-\kappa_\perp d} \mathrm{e}^{(d+a_c)\frac{n_c k - k'}{|\theta|}}\,, \tag{3.31}$$

where we used $\cos\theta \approx 1$ and $\sin\theta \approx \theta$ for a small misalignment angle $\theta \ll 1$. This Fourier component of the input field is maximized for $k' = k$, which can be used as an upper bound for $E_{z'}^{(\mathrm{in})}(k')$. Next, we want to estimate the incident power which is the amount of energy per time that passes the rim cross-section. This power is identical to the circulating power in the cavity, which can be calculated from the solution (3.5) using the Poynting vector $S = E_\varphi^* B_r/\mu_0$, which yields

$$P_\mathrm{I} = \int \mathrm{d}A \cdot |S| \approx 0.51 \frac{c n_c}{\mu_0} \left(\frac{k a_c}{\gamma}\right)^2 |B_z(0)|^2\,. \tag{3.32}$$

Scattering losses

We estimate an upper bound for the scattering losses by modelling the electrodes as perfectly conducting cylinders, as this maximizes the scattering. We expand the scattered field into solutions of the wave equation in cylindrical coordinates for the

electrode. As the radius of the electrode R is much smaller than the wavelength of the incident field λ, all contributions are supressed like $(R/\lambda)^4$, as can be seen by a Taylor expansion of the corresponding cylindrical harmonics, except s-wave scattering of TM modes, for which the supression is only logarithmic.

We determine the scattered field by use of the boundary condition

$$E_{z'}(r'=R,\varphi',z') = E_{z'}^{(\mathrm{in})} + E_{z'}^{(s)} = 0 \tag{3.33}$$

at the surface of the electrode. The transverse fields of TM solutions for the scattered field with z'-dependence $\exp(\mathrm{i}k'z')$ are given by

$$\vec{E}_{\perp}^{(s)} = \mathrm{i}\frac{k'}{k^2-k'^2}\nabla_{\perp}E_{z'}^{(s)}\,, \tag{3.34}$$

$$\vec{H}_{\perp}^{(s)} = c\epsilon_0\frac{k}{k'}\hat{z}'\times\vec{E}_{\perp}^{(s)}\,, \tag{3.35}$$

where k is the wave vector in vacuum. Since we focus only on s-wave scattering, the scattered field reads

$$E_{z'}^{(s)}(k') \propto H_0^{(1)}\left(\sqrt{k^2-k'^2}r'\right)\,, \tag{3.36}$$

with $k'^2 < k^2$. For $k'^2 > k^2$ the solution is evanescent and does not contribute the scattered power. After fixing the amplitude in (3.36) with the boundary condition (3.33), we apply the inverse Fourier transform to find the spatial scattered field

$$E_{z'}^{(s)}(r',\varphi',z') \approx -\int_{-k}^{k}\frac{\mathrm{d}k'}{2\pi}E_{z'}^{(\mathrm{in})}(k')\frac{H_0^{(1)}(\sqrt{k^2-k'^2}r')}{H_0^{(1)}(\sqrt{k^2-k'^2}R)}\mathrm{e}^{ik'z'}\,. \tag{3.37}$$

Now the scattered power can be calculated by integrating the scattered energy flux across a cylinder with infinite radius $R_*\to\infty$ that enwraps the electrode, from which we find an upper bound for the scattered power (see A.4), given by

$$P_{\mathrm{s}} \lesssim \frac{\pi c\epsilon_0}{2|\ln(2kR)|}\max\left\{\left|E_{z'}^{(\mathrm{in})}(k')\right|^2\right\}\Big|_{|k'|\le k} \tag{3.38}$$

The maximum of the incident field in that expression is found for $k'=k$, and by using $d \ll a_{\mathrm{c}}$ and $a_{\mathrm{c}} \sim \lambda = 2\pi/k$ in (3.31), we can estimate the finesse associated to scattering losses by

$$\mathcal{F}_{\mathrm{s}} \gtrsim \frac{\mathrm{e}n_{\mathrm{c}}\sqrt{n_{\mathrm{c}}^2-1}}{\pi\xi^2}\ln\left(\frac{\lambda}{4\pi R}\right)\mathrm{e}^{4\pi\frac{n_{\mathrm{c}}-1}{|\theta|}}\,, \tag{3.39}$$

where we again used the field reduction factor ξ introduced earlier. For the cavity parameters introduced earlier and an electrode radius of $R = 10\,\mathrm{nm}$, as well as a misalignment of $\theta = 10^\circ$, this still results into $\mathcal{F}_{\mathrm{s}} > 4\cdot 10^{15}$.

Dipole scattering from the gap

Here, the gap of size D between the two ends of the eletrodes that are facing each other at the nanoresoantor, is modelled by a radiating dipole that is induced by the incident field. To get an upper bound for the induced dipole, we model the gap by a perfectly conducting sphere of radius $D/2$. The induced dipole is then given by [45]

$$p \sim \frac{\pi}{2}\epsilon_0 D^3 E^{(\mathrm{in})}_{\varphi'} \cos\vartheta_* \,, \tag{3.40}$$

leading to the amount of power lost via dipole radiation

$$P_\mathrm{g} \lesssim \frac{\pi}{48}\epsilon_0 c k^4 D^6 \left(\frac{\omega\xi}{\gamma}\,|B_z(0)|\right)^2 \mathrm{e}^{-2\kappa_\perp d'} \cos^2\vartheta'_* \,. \tag{3.41}$$

This can be again compared to the incident power leading to a lower bound for the finesse associated to the gap

$$\mathcal{F}_\mathrm{g} \gtrsim \frac{4.5}{\pi^5}\frac{n_\mathrm{c} a_\mathrm{c}^2 \lambda^4}{D^6 \xi^2}\mathrm{e}^{2\kappa_\perp d'} \,. \tag{3.42}$$

For a gap of $D = 40\ \mathrm{nm}$, we thus find $\mathcal{F}_\mathrm{g} \gtrsim 1.3 \times 10^9$, which still much larger then the intrinsic finesse.

Absorption losses

Absorption losses are generated by induced currents in the electrodes. We consider transparent electrodes with conductivity σ. Here σ is a 2D-conductivity that for CNTs is bound by a maximum value given by $\sigma_\mathrm{max} = 8\,\mathrm{e}^2/\mathrm{h}$ [46]. Therefore we asume a conductivity $\sigma = \overline{\sigma}\sigma_\mathrm{max}$ with $\overline{\sigma} < 1$. The lost power is then given by

$$P_\mathrm{a} = \frac{1}{2}\int_{-\infty}^{\infty} \mathrm{d}z' \Re\left\{I^* E^{(\mathrm{in})}_{z'}\right\} \,, \tag{3.43}$$

where the current in the electrode is given by $I = 2\pi R\sigma E^{(\mathrm{in})}_{z'}$. Evaluating the absorbed power (3.43) and relating it to the incident power (3.32) leads to a finesse

$$\mathcal{F}_\mathrm{a} \gtrsim \frac{\mathrm{e}^{2\kappa_\perp d}}{32\pi\alpha_\mathrm{F}\xi^2\overline{\sigma}}\sqrt{\frac{\kappa_\perp a_\mathrm{c}}{\pi}}\frac{n_\mathrm{c} a_\mathrm{c}}{R\sin\theta} \,, \tag{3.44}$$

with the fine structure constant $\alpha_\mathrm{F} \approx 1/137$. Evaluating $\mathcal{F}_\mathrm{a}$ shows that absorption is the dominant additional loss effect. For an asumed conductivity $\overline{\sigma} = 1/20$ and an improved alignment precision of $\theta = 3°$, as well as an electrode radius $R = 2.5\ \mathrm{nm}$, we still find $\mathcal{F}_\mathrm{a} \gtrsim 3.7 \times 10^7$.

3.5.2 Mechanical decoherence induced by electrical noise

With the presented setup, we want to enable the observation and usage of quantum effects in the mechanical motion. A natural effect that always complicates the observation and use of quantum effects is decoherence due to coupling of the quantum degree of freedom to the surrounding environment. In common nanomechanical resonators, including nanotube resonators, the dominant source of damping and decoherence are clamping losses [29]. Here, we are addressing the motion of the nanotube via electric gradient fields using the polarizability of the tube. Usually, when nanosystems are sensitive to electrical fields, various sources of electrical noise have to be faced and overcome by experimentalists. Here, we show that in our setup, the most common noise sources, which are voltage noise in the electrodes (Johnson-Nyquist noise) and fluctuating charges on the chip surface ($1/f$-noise), are negligible compared to the well known clamping losses. This is mainly because the CNT is not charged and the sensitivity to electric fields is due of the polarisability only, so that applied fields need to be rather large to affect significantly affect the resonator motion. We calculate the decoherence rates corresponding to the specific noise spectra by

$$\Gamma_i = \frac{x_{\mathrm{ZPM}}^2}{\hbar^2} S_{\delta F_i}(\omega_{\mathrm{m}})\,, \tag{3.45}$$

where the noise spectra are given by the force fluctuations δF_i acting on the resonator

$$S_{\delta F_i}(\omega) = \mathrm{Re}\int_0^\infty \mathrm{d}\tau\, \langle \delta F_i(\tau)\delta F_i(0) + \delta F_i(0)\delta F_i(\tau)\rangle\, \mathrm{e}^{\mathrm{i}\omega\tau}\,. \tag{3.46}$$

The electric field gradient force acting on a resonator can be expressed by

$$F_{\mathrm{el.}} = \frac{\alpha}{2}\frac{\partial}{\partial X}\int E^2 \mathrm{d}l \approx \alpha a E\left(\frac{E}{a}\right)\,, \tag{3.47}$$

where we estimated the field gradient at a distance a from the electrode by E/a and used the fact that the field mainly acts on the nanotube in a region of length $a \ll L$. For an electric field with fluctuations associated to different independent sources $E + \sum_i \delta E_i$, the force fluctuations are then given by

$$\delta F_i \approx 2\alpha E \delta E_i\,. \tag{3.48}$$

Thus, the resulting decoherence rates read

$$\Gamma_i \approx \frac{x_{\mathrm{ZPM}}^2}{\hbar^2} S_{\delta F_i} = 4\frac{x_{\mathrm{ZPM}}^2}{\hbar^2}\alpha^2 E^2 S_{\delta E_i}\,, \tag{3.49}$$

where the $S_{\delta E_i}$ are the noise spectra for the different electric field fluctuations.

Johnson-Nyquist noise

For Johnson-Nyquist noise [47], we have fluctuating voltages δU with

$$S_{\delta U} \simeq 4k_{\mathrm{B}}TR \quad \text{and thus} \quad S_{\delta E} \approx S_{\delta U}/a^2\,, \tag{3.50}$$

for an ambient temperature T and an electrode resistance R. For our setup we find $\Gamma_{\delta U}/R < 10^{-2}\ \mathrm{Hz}/\Omega$ at $T = 20\ \mathrm{mK}$, which is well below the mechanical damping $\gamma_{\mathrm{m}}\overline{n} \approx 0.1\ \mathrm{kHz}$ for a large range of possible resistances.

$1/f$-noise

The origin of $1/f$-noise is usually associated with surface charge fluctuations in the device. An electric field noise density $S_E(\omega/2\pi = 3.9\,\mathrm{kHz}) \approx 4\ \mathrm{V^2 m^{-2} Hz^{-1}}$ has been measured at $T = 300\ \mathrm{K}$ and at a distance of $20\ \mathrm{nm}$ between a charged resonator and a gold surface [48]. For a scaling $S_E(\omega) \sim T/\omega$ [48, 15] this corresponds to $S_E \approx 2\cdot 10^{-7}\ \mathrm{V^2 m^{-2} Hz^{-1}}$ for our conditions with $T = 20\,\mathrm{mK}$ and $\omega_{\mathrm{m}}/2\pi \approx 5.2\ \mathrm{MHz}$. For the associated decoherence rate we thus find $\Gamma_{1/f} < 0.15\ \mathrm{Hz}$, which is again well below the mechanical damping $\gamma_{\mathrm{m}}\overline{n}$.

Chapter 4

Stationary nonclassical states

4.1 Introduction

One major goal in the field of quantum physics in general, that has led to large efforts on the experimental side and has always come along with fundamental theoretical questions, is the preparation of different physical systems in distinct quantum states. This reaches from photons over single atoms, ions or molecules to larger systems like condensates. In 2012 two experimental physicists, Serge Haroche and David Wineland, recieved the nobel price "for ground-breaking experimental methods that enable measuring and manipulation of individual quantum systems" [49], which the both developed in their respective fields, being cavity quantum electrodynamics with single atoms and experiments with trapped ions [50, 51].

But also in the field of optomechanics, during the last decade there has been large progress towards introducing mechanical resonators into the realm of quantum physics. The efforts, that in large parts have been technical improvements in the top-down fabrication of micro- and nanomechanical resonators, have been rewarded only in the recent few years, where different experimental groups reported that they have reached the quantum regime of mechanical motion [52, 19, 11, 12, 13]. The quantum regime is the regime of only few excitations, which means that the resonator is close to the quantum ground state. This sets the stage for further investigations in this regime. One natural next step is the controlled preparation of different classes of quantum states. Clearly, the interest in the preparation of quantum states for single ions or atoms is already large, even though there is no doubt that these systems behave according to quantum mechanics. For nanomechanical systems, the situation is different, since quantum behaviour in these devices is something totally new to be observed. Therefore the controlled preparation of nonclassical states in these systems should be of even larger interest. The scheme that was proposed in [53] and will be presented here is meant to contribute to this goal.

In most of the above mentioned experiments, the quantum regime was reached by applying resolved sideband cooling of the mechanical resonator [54, 55]. This tech-

nique is similar to laser cooling of ions or atoms, where photons scattering from the target are used to extract quanta of motional energy. The scheme that is presented here, works in a similar way and the theory can be understood in close analogy to the sideband cooling technique used in optomechanical experiments. However, involving a nonlinear nanomechanical resonator, causes richer dynamics that resolves individual mechanical energy eigen states. Therefore this chapter is organized as follows: In section 4.2 a brief introduction to sideband cooling is given. After that, in section 4.3, a short introduction to Wigner functions is given. They are used to demonstrate an important connection between nonlinear quantum systems and noncassicality. In 4.4 we turn to the aforementioned scheme, which involves the derivation of a reduced equation of motion for the nonlinear nanoresonator, its steady state solution, as well as a analytic and numerical results. Finally, methods to measure the quantum state of the mechanical resonator are presented in section 4.8.

4.2 Sideband cooling of mechanical motion

Here we give a short introduction of cavity-assisted sideband cooling of nanomechanical resonators. This procedure is a necessary preliminary step before applying any of the schemes introduced later. It brings the nanomechanical resonator from a thermal state with many excitations to the quantum regime of few excitations. Note that also numerical calculations that operate in a Hilbert space that is represented by Fock states or energy eigen states can only be carried out in this regime, so that a pre-cooled state is always asumed in the calculations. Furthermore, the scheme presented in this part, can be viewed as an extention of the sideband cooling scheme presented in [54] to the case of a nonlinear resonator.

The coupled system of cavity and mechanical resonator is described by an open quantum system and the motion of the systems state is governed by the master equation (1.14), where we asume a harmonic mechanical resonator here, using the system Hamiltonian (1.12). In the weak optomechanical coupling regime $g_\mathrm{m} \ll \kappa$, the cavity degree of freedom can be adiabatically eliminated [54, 56], since in the shifted picture the cavity remains in the ground state $\langle a^\dagger a \rangle \ll 1$. This elimination leads to a reduced master equation for the mechanical motion, that reads

$$\dot{\mu} \approx -\frac{\mathrm{i}}{\hbar}\left[\omega_\mathrm{m} b^\dagger b, \mu\right] + \frac{1}{2}\left(\gamma_\mathrm{m}\left[\overline{n}+1\right] + A_-\right)\mathcal{D}_b\mu + \frac{1}{2}\left(\gamma_\mathrm{m}\overline{n} + A_+\right)\mathcal{D}_{b^\dagger}\mu\,, \tag{4.1}$$

with the reduced mechanical state μ, the thermal occupation of mechanical bath modes $\overline{n} = 1/(\exp[\hbar\omega_\mathrm{m}/k_\mathrm{B}T])$ at temperature T and the cooling (heating) rates associated to the cavity

$$A_\pm = g_\mathrm{m}^2 \frac{\kappa}{4\left(\Delta \mp \omega_\mathrm{m}\right)^2 + \kappa^2}\,. \tag{4.2}$$

This equation describes perturbative cooling for $\Delta = -\omega_\mathrm{m}$. In the resolved sideband regime $\kappa < \omega_\mathrm{m}$, the total cooling rate $\Gamma = A_- - A_+$ can overcome heating by

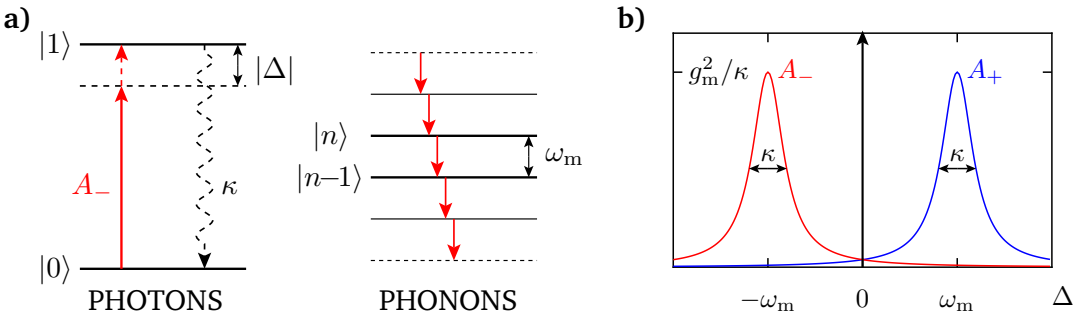

Figure 4.1: Illustration of the cooling process. **a)**: A red detuned laser photon with energy $\hbar(\omega_c - \omega_m)$ can only enter the cavity by absorbing the energy of one phonon. Therefore the laser resonantly drives the transition $|0,n\rangle \rightarrow |1,n-1\rangle$, where the first entry is the photon number and the second the phonon number. The photon decays quickly $|1,n-1\rangle \rightarrow |0,n-1\rangle$ so that the whole cycle is $|0,n\rangle \rightarrow |0,n-1\rangle$. **b)** The sidebands have to resolved $\kappa < \omega_m$ so that only the cooling process is adressed and $A_- \gg A_+$.

the environment $\overline{n}\gamma$ and the steady state of the resonator is a thermal state with a reduced occupation $n_f = \overline{n}\gamma_m/(\Gamma + \gamma_m)$, which corresponds to a thermal state at a lower temperature. The process of cooling can be regarded as successive absorption of phonons by photons that enter the cavity and immediately (with respect to mechanical timescales) decay again, thereby transporting mechanical energy out of the system, see figure 4.1.

Wether the groundstate has been reached, can be measured from the output power spectrum of a resonant probe laser ($\Delta = 0$), which shows red and blue detuned sideband peaks. The relative weights of the blue and red sideband peaks, corresponding to up and down converted photons, is given by $n_f/(n_f+1)$ [54]. The blue detuned sideband peak vanishes when approaching the groundstate $n_f \rightarrow 0$, since up-converting photons aquires the absorption of phonons, which is of course not possible if the resonator is already in the motional groundstate. This sideband effect has been used in experiments to identify the mechanical resonators in (or close to) the mechanical groundstate [12, 52]. But while successfully cooling into the motional ground state is the first step, it is not sufficient to verify distinct quantum behaviour of the cooled mechanical motion. We want to elaborate on this important aspect in the next section.

4.3 Wigner functions, nonclassicality and nonlinearity

In this section we want to introduce the concept of the Wigner function as a phase space distribution that entirely represents the quantum state of a particle or a mode [57]. This representation has the advantage that it is capable of providing a nice

visualisation of a quantum state and a quite intuitive interpretation of some features of the state. One aspect we will be looking at here very briefly, is a possible classification of quantum states with respect to *nonclassicality*, that uses the Wigner representation. Using this classification one can then demonstrate a very important connection between the excistance of nonlinearities in a quantum system and its possibilities to aquire nonclassical states.

The Wigner function for a certain quantum state ρ is defined by

$$W(x,p) = \frac{1}{\pi\hbar}\int_{-\infty}^{\infty} \mathrm{d}y \langle x-y|\rho|x+y\rangle \mathrm{e}^{-2\mathrm{i}py/\hbar} \tag{4.3}$$

where $|x\rangle$ is the position eigenstate for the position x and p is the momentum. It contains the same information as the density operator ρ and satisfies

$$\int_{-\infty}^{\infty} \mathrm{d}p\, W(x,p) = \langle x|\rho|x\rangle\,, \tag{4.4}$$

$$\int_{-\infty}^{\infty} \mathrm{d}x\, W(x,p) = \langle p|\rho|p\rangle\,, \tag{4.5}$$

$$\int_{-\infty}^{\infty} \mathrm{d}x \int_{-\infty}^{\infty} \mathrm{d}p\, W(x,p) = 1\,, \tag{4.6}$$

so that $W(x,y)$ has similarities to a classical probability distribution. There exist different phase space distributions to describe a quantum state like the for instance the P and Q distributions, but the Wigner distribution can be considered to be closest to a classical probability distribution, since it is a real function that is normalized and bound from below and above. The only striking feature that prevents from replacing it by a classical distribution is the fact that the Wigner function can have negative regions for certain quantum states. This is in accordance with the uncertainty principle of quantum mechanics, since the probability for a quantum particle to be at an exact location with an exact momentum *at the same time* is inherently prevented from being a physical quantity to be measured. But it restricts any interpretation as a classical probability distribution in the general case. In general, single points of the Wigner function can not be interpretated easily by a physical quantity. The entire Wigner distribution however, is physical in the sense that it can be measured using homodyne schemes, including negative regions. To do so, the complete information of a quantum state is collected by determining the (positive) distributions for all quadratures $X_\theta = \cos\theta x + \sin\theta p$, a process that is called quantum state tomography. Then the Wigner function and thus the density operator can be obtained by mathematical transformation of the results [58]. By the argumentation given above, one can define nonclassicality of a quantum state by the appearance of negative regions in the Wigner function [59, 60], which is today a widely accepted convention [1].

[1] Note that the situation becomes more difficult for multipartite systems, where nonclassical correlations still can exist between the subsystems, even if the composite Wigner function is Gaussian [61].

To discuss the connection between nonlinearities in a system and nonclassicality, it is convenient to introduce a certain class of quantum states called Gaussian states. They are called Gaussian since their Wigner distribution is a Gaussian function. Thermal states, sqeezed states and coherent states belong to this class, compare first row of figure 4.2. Coherent states are considered closest to a classical picture as they have minimum uncertainty and their Wigner function is closest to a classical point in phase space. One important aspect of Gaussian states is their time evolution in linear systems. One can show that any initial input state that is Gaussian remains Gaussian if the considered system is linear and driven only with classical fields. This means that the Hamiltonian has no terms higher than second order in the involved operators. This can be understood by considering the dynamics of the Wigner function of the system, which in that case is given by a linear Fokker-Planck equation. Therefore also the dynamics of Gaussian states can be described by classical equations of motion for a probability distribution. In particular, it follows that groundstate cooling of a mechanical mode, which comprises a linearized optomechanical coupling, is not sufficient to obtain a nonclassical quantum state.

Different classes of quantum states are for example Fock states or macroscopic superpositions states, sometimes called Schrödinger cat states. These states are considered highly nonclassical and are usually difficult to prepare in an experiment. They all show distinct negative regions in the Wigner representations, see figure 4.2.

In order to obtain nonclassical states from the dynamics of a system, a nonlinear element has to be introduced into a quantum system. In some systems, like for instance microwave resonators, this was achieved by coupling to nonlinear ancilla systems [21, 62, 20]. For optomechanical systems, nonlinearities naturally arise in the strong optomechanical coupling regime, where the coupling term becomes nonlinear, compare (1.2). Here, we instead choose a different approach by using the intrinsic nonlinearity of the nanomechanical resonator while the coupling remains linear. This has the advantage that the possibility to drive transitions in the mechanical spectrum in a controlled way, as it is also applied in sideband cooling scheme, is preserved. In the next section we will describe how this can be exlpoited.

4.4 Preparation of nonclassical states

While the successful cooling of a mechanical resonator close to the ground state is the starting point for observing quantum effects, the cooled state itself still has to be considered a classical state. This fact is underpinned by the fact that the Wigner function for any thermal state and even for the ground state is a non-negative Gaussian function. Here, we introduce a scheme to prepare a mechanical resonator in a distinct nonclassical steady state, using an enhanced mechanical nonlinearity as introduced in part 2. The mechanical nonlinearity is the necessary ingredient in this scheme to prepare non-Gaussian states. The nonclassicality is then identified by a negative Wigner function.

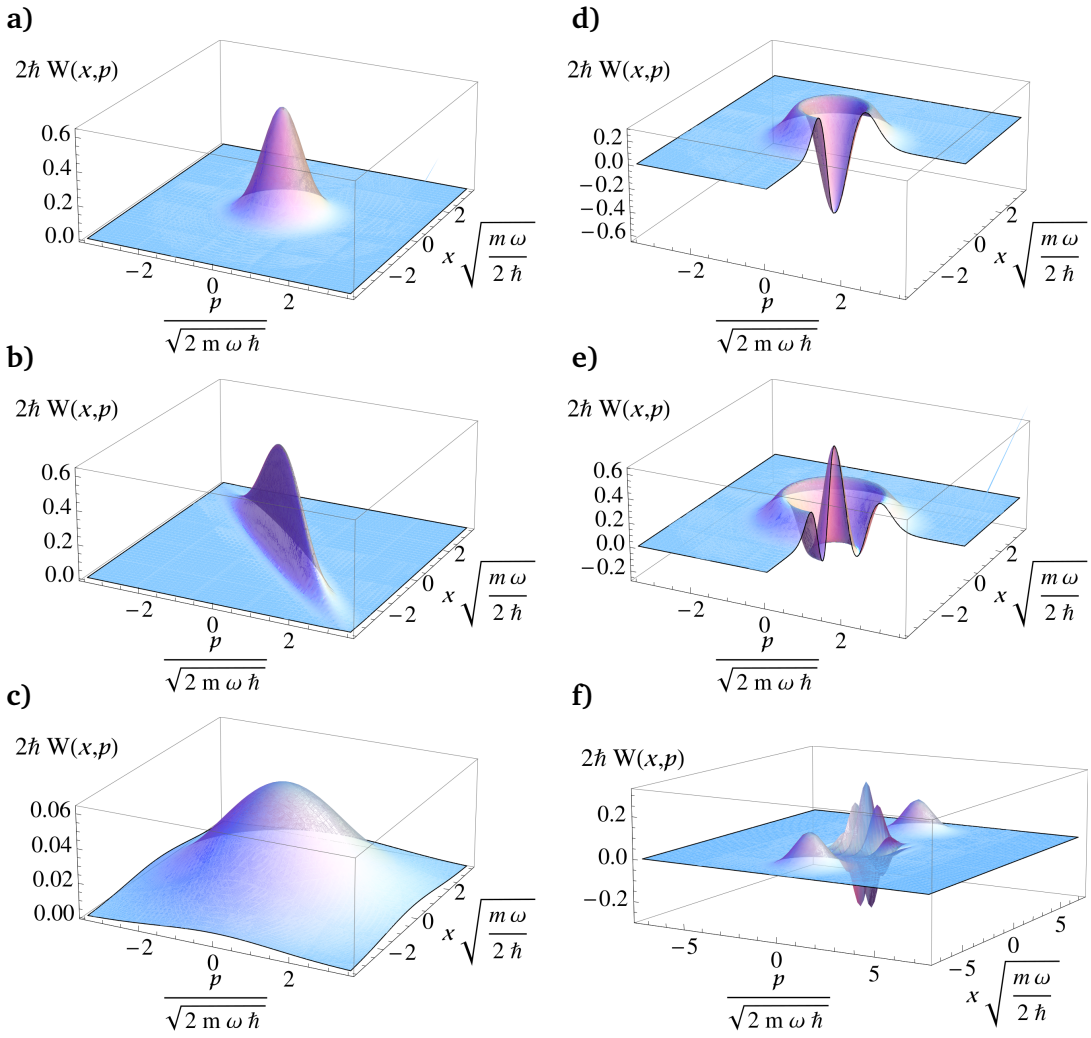

Figure 4.2: Wigner functions for different quantum states. The states in the left column are classical Gaussian states, the ones in the right column are nonclassical states: **a)** The vacuum state $|0\rangle$. A coherent state $|\alpha\rangle$ is obtained by displacing the vacuum state by $(\Re[\alpha], \Im[\alpha])$ along the normalized (x, p) axes. **b)** A squeezed quadrature state. **c)** A thermal state at Temperature $k_{\mathrm{B}}T = 5\,\hbar\omega$ which corresponds to $n_{\mathrm{th}} \approx 4.5$ excitations. **d)** Fock state $|1\rangle$ **e)** Fock state $|2\rangle$. **f)** A cat state $\sqrt{1/2}(|\alpha\rangle + |-\alpha\rangle)$ with $\alpha = 5$.

The scheme works in close analogy to the sideband cooling technique introduced above, but there are some differences: Instead of only one cavity mode, we here involve several laser driven cavity modes, labeled by an index j, that interact with the mechanical resonator. Furthermore we add the nonlinearity to the mechanical part, so that the Hamiltonian for that system reads

$$H = \sum_j -\Delta_j a_j^\dagger a_j + \sum_j \left(\frac{g_{\mathrm{m},j}}{2} a_j^\dagger + \mathrm{H.c.}\right)\left(b^\dagger + b\right) + \omega_\mathrm{m} b^\dagger b + \frac{\lambda}{2}(b^\dagger + b)^4 \,. \tag{4.7}$$

Here we introduced the multiple cavity modes $j = 1, 2, \ldots$ described by photon operators a_j that are each coherently driven by laser with a detuning $\Delta_j = \omega_{\mathrm{L},j} - \omega_{\mathrm{c},j}$. We already used the shifted representation for the photons (compare chapter 1) and the linearized optomechanical couplings at strengths $g_{\mathrm{m},j} = 2\alpha_j G_0 x_\mathrm{ZPM}$, with $\alpha_j = \Omega_j/(2\Delta_j + \mathrm{i}\kappa_j)$ being the steady state coherent amplitde in cavity mode j, Ω_j the laser drive Rabi frequency and κ_j the photon decay rate of that mode. Note that we already asumed a tuned resonator. This means that the nonlinearity λ is tuned to a sufficient strength by using gradient fields and the static deflection of the resonator due to the cavity field is compensated by choosing $F_1^\mathrm{s} = -\hbar G_0 |\alpha|^2$.

The cavity decay as well as the mechanical damping at rate γ_m are described by the master equation

$$\dot{\rho} = -\mathrm{i}\,[H, \rho] + \sum_j \frac{\kappa_j}{2}\mathcal{D}_{a_j}\rho + \frac{\gamma_\mathrm{m}}{2}\left\{\overline{n}\mathcal{D}_b\rho + (\overline{n}+1)\mathcal{D}_{b^\dagger}\rho\right\} \tag{4.8}$$

For the following analysis it is convenient to apply a rotating wave approximation for $\lambda \ll \omega_\mathrm{m}$ so that the mechanical part reads

$$H_\mathrm{m} \to H'_\mathrm{m} = \omega'_\mathrm{m} b^\dagger b + \frac{\lambda'}{2} b^\dagger b^\dagger b b \,. \tag{4.9}$$

with $\omega'_\mathrm{m} = \omega_\mathrm{m} + 2\lambda'$ and $\lambda' = 6\lambda$, compare (2.36). In this approximation the eigen states of the resonator remain Fock states $|n\rangle$. Applying the Heisenberg picture for the mechanical operators already reveals Fock state resolved dynamics, since

$$\mathrm{e}^{\mathrm{i}H'_\mathrm{m}t} b \mathrm{e}^{-\mathrm{i}H'_\mathrm{m}t} = \sum_n \mathrm{e}^{-\mathrm{i}\delta_n t} b_n \,, \tag{4.10}$$

where we introduced the projectors $b_n = \sqrt{n}|n-1\rangle\langle n|$, as well the transition frequencies $\delta_n = (E_n - E_{n-1})/\hbar = n\lambda'$. Note that since the transition frequencies now depend on the Fock number n, the shape of the mechanical damping terms as considered in (4.8) can only be an approximate description. The details of the mechanical damping actually depend on the bath model one considers in deriving the Lindblad form. Here we neglected any frequency dependence in the microscopic couplings between bath modes and resonator and considered only one number for the thermal occupation of bath modes, which is the thermal occupation $\overline{n}$ at the tuned mechanical frequency ω_m. However, the impact of the differences between

possible damping models on the results are expected to be small enough to be neglected within this analysis. In fact, calculations using different thermal occupations $\overline{n}(\delta_n)$ for the slightly different transition frequencies δ_n have been done. Relative deviations from calculations with the model (4.8) were found to be well below 10^{-3}. Because of this. and also since the main focus here is not the analysis of damping mechanisms, we do not further address that interesting topic and in particular do not consider a model that describes nonlinear damping.

4.5 Reduced master equation

Now we want to carry out an adiabatic elimination of the photon mode, wich can be done for $g_{\mathrm{m},j} \ll \kappa_j$. We also asume $g_{\mathrm{m},j} \gg \overline{n}\gamma_{\mathrm{m}}$, necessary for groundstate cooling and $\kappa < \lambda'$, which we want to call the *resolved nonlinearity regime* in analogy to the resolved sideband regime for $\kappa < \omega_{\mathrm{m}}$. In deriving a reduced master equation for the mechanical motion, we follow the projection operator technique [56]. Do to so it is convenient to write the master equation (4.8) in terms of the Liouville operator $\mathcal{L}$

$$\dot{\rho}(t) = \mathcal{L}(t)\rho(t) \tag{4.11}$$

with

$$\mathcal{L}(t) = \zeta^2\mathcal{L}_0 + \zeta\mathcal{L}_1(\zeta^2 t) + \mathcal{L}_2(\zeta^2 t)\,. \tag{4.12}$$

Here we split the Liouvillian into parts that are associated to different timescales in the dynamics. The later are labeled with a dimensionless parameter $\zeta \gg 1$, that will be used for a systematic expansion. The fastest time scale, labeled by ζ^2, is the mechanical motion and the cavity motion, where the timescale is set by $\omega_{\mathrm{m}} \approx |\Delta|$ and κ_j. The slowest time scale is set by mechanical damping $\overline{n}\gamma_{\mathrm{m}}$ and in between there is the timescale of the optomechanical coupling, labeled by ζ, for which we have $\overline{n}\gamma_{\mathrm{m}} \ll g_{\mathrm{m},j} \ll \kappa_j$. As we will find, the separation between $\mathcal{L}_0$ and $\mathcal{L}_1$ leads to the Born-Markov approximation for $\zeta \to \infty$. The different parts of the Liouvillian therefore read

$$\mathcal{L}_0\rho = \sum_j \left\{ \mathrm{i}\left[\Delta_j {a_j}^\dagger a_j, \rho\right] + \frac{\kappa_j}{2}\left[2a_j\rho{a_j}^\dagger - {a_j}^\dagger a_j\rho - \rho{a_j}^\dagger a_j\right]\right\}, \tag{4.13}$$

$$\mathcal{L}_1(\zeta^2 t)\rho = \sum_n \left[\mathrm{e}^{\mathrm{i}\zeta^2\delta_n t}\mathcal{L}_{1n}^{(+)} + \mathrm{e}^{-\mathrm{i}\zeta^2\delta_n t}\mathcal{L}_{1n}^{(-)}\right], \tag{4.14}$$

$$\mathcal{L}_2(\zeta^2 t)\rho = \frac{\gamma_{\mathrm{m}}}{2}\sum_{n,m}\left[(\overline{n}+1)\mathrm{e}^{\mathrm{i}\lambda(n-m)\zeta^2 t}\mathcal{D}_{nm}^{-}\rho + \overline{n}\mathrm{e}^{-\mathrm{i}\lambda(n-m)\zeta^2 t}\mathcal{D}_{nm}^{+}\rho\right]. \tag{4.15}$$

Here, we changed to an interaction picture with respect to H'_{m}, where the nonlinearity is responsible for the separation of terms involving different Fock states

$$\mathcal{L}_{1n}^{(+)} = -\mathrm{i}\sum_j \left[\left(\frac{g_{\mathrm{m},j}^*}{2}a_j + \mathrm{H.c.}\right) b_n^\dagger, \rho\right] , \tag{4.16}$$

$$\mathcal{L}_{1n}^{(-)} = -\mathrm{i}\sum_j \left[\left(\frac{g_{\mathrm{m},j}^*}{2}a_j + \mathrm{H.c.}\right) b_n, \rho\right] , \tag{4.17}$$

$$\begin{aligned}\mathcal{D}_{nm}^{-}\rho &= 2b_n\rho b_m^\dagger - b_m^\dagger b_n\rho - \rho b_m^\dagger b_n \,, \\ \mathcal{D}_{nm}^{+}\rho &= 2b_n^\dagger\rho b_m - b_m b_n^\dagger\rho - \rho b_m b_n^\dagger \,. \end{aligned} \tag{4.18}$$

We now define projection operators $\mathcal{P}$ and $\mathcal{Q}$ by

$$\mathcal{P}\rho = \mathrm{Tr}_{\mathrm{c}}\{\rho\}\otimes\rho_{\mathrm{c}}^{(\mathrm{th})} \,, \qquad \mathcal{Q} = \mathbb{1} - \mathcal{P} \,, \tag{4.19}$$

where the thermal state for cavity modes is given by

$$\rho_{\mathrm{c}}^{(\mathrm{th})} = \bigotimes_j \rho_{\mathrm{c},j}^{(\mathrm{th})} \,, \qquad \rho_{\mathrm{c},j}^{(\mathrm{th})} = \frac{1}{n_{\mathrm{c},j}+1}\sum_{n=0}^{\infty}\left[\frac{n_{\mathrm{c},j}}{n_{\mathrm{c},j}+1}\right]^n |n\rangle\langle n|_{\mathrm{c},j} \,, \tag{4.20}$$

and can be taken as the vacuum state ($n_{\mathrm{c},j}=0$) for each cavity and the trace $\mathrm{Tr}_{\mathrm{c}}\{.\}$ is taken over all cavity modes. We call $\mathcal{P}\rho$ the relevant part of the system, which is the mechanical state, and $\mathcal{Q}\rho$ is called the irrelevant part. Using the projections $\mathcal{P}$ and $\mathcal{Q}$ in (4.11) it is possible to derive a closed equation for the relevant part, see A.5 for details. Using certain assumptions about the initial state of the system at $t=0$, this leads to the Nakashima-Zwanzig equation [56, 63]

$$\mathcal{P}\dot{\rho} = \mathcal{P}\mathcal{L}(t)\mathcal{P}\rho + \mathcal{P}\mathcal{L}(t)\int_0^t \mathrm{d}\tau \mathcal{T}_+\left[\mathrm{e}^{\int_0^t \mathrm{d}\tau' \mathcal{Q}\mathcal{L}(\tau')\mathcal{Q}}\right]\mathcal{T}_-\left[\mathrm{e}^{-\int_0^\tau \mathrm{d}\tau'' \mathcal{Q}\mathcal{L}(\tau'')\mathcal{Q}}\right]\mathcal{Q}\mathcal{L}(\tau)\mathcal{P}\rho(\tau) \,. \tag{4.21}$$

This equation is exact so far. We now apply the limit $\zeta\to\infty$ and keep only the lowest nontrivial order in $1/\zeta$, see A.5. In this limit all fast rotating terms drop out which amounts to a RWA. Inserting (4.14) we get

$$\mathcal{P}\dot{\rho} = \mathcal{P}\tilde{\mathcal{L}}_2\mathcal{P}\rho + \sum_n n\left[\mathcal{P}\mathcal{L}_{1n}^{(+)}\int_0^\infty \mathrm{d}\tau' \mathrm{e}^{\mathrm{i}\delta_n\tau'}\mathrm{e}^{\mathcal{L}_0\tau'}\mathcal{Q}\mathcal{L}_{1n}^{(-)}\mathcal{P}\rho + \mathrm{H.c.}\right] , \tag{4.22}$$

with $\tilde{\mathcal{L}}_2$ containing only the non rotating terms

$$\tilde{\mathcal{L}}_2\rho = \frac{\gamma_{\mathrm{m}}}{2}\sum_n\left[(\overline{n}+1)\mathcal{D}_{b_n}\rho + \overline{n}\mathcal{D}_{b_n^\dagger}\rho\right] . \tag{4.23}$$

The integral contains the cavity two-time correlations, which can be seen by inserting the definitions of $\mathcal{L}_0, \mathcal{L}_{1n}^{(\pm)}$ and by applying the projection $\mathcal{P}$, which yields

$$\mathcal{P}\mathcal{L}_{1n}^{(+)} \int_0^\infty \mathrm{d}\tau' \mathrm{e}^{\mathrm{i}\delta_n\tau'} \mathrm{e}^{\mathcal{L}_0\tau'} \mathcal{Q}\mathcal{L}_{1n}^{(-)} \mathcal{P}\rho =$$

$$= \sum_j \left(-\frac{|g_{\mathrm{m},j}|^2}{2} \right) \int_0^\infty \mathrm{d}\tau \mathrm{e}^{\mathrm{i}\delta_n\tau} \mathrm{Tr}_\mathrm{c} \left\{ \left[X_j b_n^\dagger, \mathrm{e}^{\mathcal{L}_0\tau} \left[X_j b_n, \mu \otimes \rho_\mathrm{c}^{(\mathrm{th})} \right] \right] \right\} . \tag{4.24}$$

Here we introduced the density operator for the mechanical mode $\mu = \mathrm{Tr}_\mathrm{c}\{\rho\}$, and the cavity-quadratures $X_j = \left(\alpha_j^* a_j + \alpha_j {a_j}^\dagger \right) / \sqrt{2}|\alpha_j|$. Note that this expression is of second order in the optomechanical couplings $g_{\mathrm{m},j}$, which corresponds to the Born approximation. Since within the interaction picture, the mechanical operators evolve much slower than the integrand decays due to the loss part in $\mathcal{L}_0$, the mechanical operators can be pulled out of the trace and the integrals. This corresponds to the Markov approximation. The remaining integrals over the cavity correlation function can be expressed by defining

$$G_j(\omega) = \int_0^\infty \mathrm{d}\tau \mathrm{e}^{\mathrm{i}\omega\tau} \mathrm{Tr}_\mathrm{c} \left\{ X_j \mathrm{e}^{\mathcal{L}_0\tau} X_j \rho_\mathrm{c}^{(\mathrm{th})} \right\} = \frac{1}{-2\mathrm{i}(\omega + \Delta_j) + \kappa_j} , \tag{4.25}$$

where the integral has been evaluated using the correlations functions for the free cavity. Note that all contributions that correspond to cross correlations between the cavity modes $\mathrm{Tr}_\mathrm{c} \left\{ X_i \mathrm{e}^{\mathcal{L}_0\tau} X_j \rho_\mathrm{c}^{(\mathrm{th})} \right\}$ with $i \neq j$ drop out. With this definition, (4.24) becomes

$$\ldots = -\sum_j \frac{|g_{\mathrm{m},j}|^2}{2} \left\{ G_j(\delta_n) \left[b_n^\dagger, b_n \mu \right] - G_j^*(-\delta_n) \left[b_n^\dagger, \mu b_n \right] \right\} . \tag{4.26}$$

Now all those contributions in (4.22) can be rearranged to Lindblad form and after changing back to the Schrödinger picture we find a reduced master equation for the mechanical motion that reads

$$\dot{\mu} = -\mathrm{i} \left[H_\mathrm{m}' + \sum_{n,j} \left(\Delta_{\mathrm{m},j}^{n,+} b_n^\dagger b_n + \Delta_{\mathrm{m},j}^{n,-} b_n b_n^\dagger \right), \mu \right] +$$

$$+ \frac{1}{2} \sum_n \left\{ \left[\sum_j A_{-,j}^n + \gamma_\mathrm{m} (\overline{n} + 1) \right] \mathcal{D}_{b_n} \mu + \left[\sum_j A_{+,j}^n + \gamma_\mathrm{m} \overline{n} \right] \mathcal{D}_{b_n^\dagger} \mu \right\} . \tag{4.27}$$

This master equation governs the motion of the mechanical state, where the main influence of the laser driven cavity modes is found by additional Lindblad terms proportional to the transition rates

$$A_{\pm,j}^n = \frac{|g_{\mathrm{m},j}|^2}{2} \Re \left\{ G_j(\mp\delta_n) \right\} = g_{\mathrm{m},j}^2 \frac{\kappa_j}{4(\Delta_j \mp \delta_n)^2 + \kappa_j^2} . \tag{4.28}$$

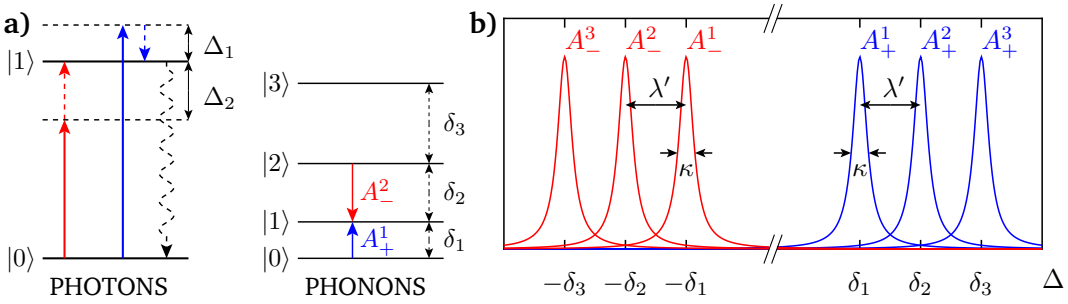

Figure 4.3: Illustration of the state preparation process for a nonlinear mechanical resonator, compare also figure 4.1. **a)** By adjusting the laser detuning for each cavity mode, specific transitions in the mechanical spectrum can be adressed. **b)** The nonlinearity λ' has to be resolved by the cavity linewidths κ_j.

In close analogy to the sideband cooling scheme these rates dominate over the mechanical dampling rate γ_m, while the small spectral shifts

$$\Delta_{\mathrm{m},j}^{n,\pm} = \frac{|g_{\mathrm{m},j}|^2 \left(\Delta_j \pm \delta_n\right)}{4(\Delta_j \pm \delta_n)^2 + \kappa_j^2}\,, \tag{4.29}$$

have no further relevance in this context and can be neglected compared to the order of ω_m. The dissipators $\mathcal{D}_{b_n^{(\dagger)}}$ describe the incoherent population transfer between neighboring Fock states $|n\rangle \leftrightarrow |n-1\rangle$. To be able to address specific transitions selectively by choosing the detuning resonantly to the corresponding sideband, we need the resolved nonlinearity $\kappa_j < \lambda'$, compare figure 4.3.

4.6 Steady state solution

Here we derive relations that describe the stationary state of the mechanical resonator. This state remains stable as long as the driving lasers are on and the environmental temperature can be kept stable. The energy eigen states of the resonator within the RWA (4.9) are Fock states and the Liouvillian associated to the reduced master equation (4.27) maps a state μ that is diagonal in Fock basis on to another diagonal state. Thus, the steady state for that reduced master equation can be found using the ansatz

$$\mu = \sum_n P_n |n\rangle\langle n|\,, \tag{4.30}$$

for a diagonal density matrix μ. For this ansatz the unitary part vanishes, so that we need to solve

$$0 = \sum_n \left[\left\{ \sum_j A^n_{-,j} + \gamma_\mathrm{m} \left[\overline{n}+1\right] \right\} P_n \left(b_n b_n^\dagger - b_n^\dagger b_n \right) \right.$$
$$\left. + \left\{ \sum_j A^n_{+,j} + \gamma_\mathrm{m} \overline{n} \right\} P_{n-1} \left(b_n^\dagger b_n - b_n b_n^\dagger \right) \right] . \tag{4.31}$$

Thus, the coefficient of $|n\rangle\langle n|$ for each n in the sum has to vanish, which leads to the steady state relations

$$\frac{P_n}{P_{n-1}} = \frac{\sum_j A^n_{+,j} + \gamma_\mathrm{m} \overline{n}}{\sum_j A^n_{-,j} + \gamma_\mathrm{m} \left[\overline{n}+1\right]} \equiv F(n) \, . \tag{4.32}$$

These relations together with $\sum_n P_n = 1$, which follows from normalization, determine the steady state of the mechanical oscillator. It can be calculated numerically by introducing a cutoff number n_0, satisfying $\sum_{n=n_0+1}^{\infty} P_n \ll 1$, using

$$P_0 = \left[\sum_n^{\infty} \prod_{i=0}^{n-1} F(i+1) \right]^{-1} \approx \left[\sum_n^{n_0} \prod_{i=0}^{n-1} F(i+1) \right]^{-1} \tag{4.33}$$

and calculating the other P_n successively using the recursion relation (4.32). Note that for lasers switched off, the $A^n_{\pm,j}$ vanish and we obtain relations characterising a thermal state at the bath temperature. If instead we let $\lambda \to 0$, the ratio P_n/P_{n-1} becomes n-independent, implying a thermal state at a different temperature depending on the laser detunings and amplitudes.

4.7 Results

By looking at the relations (4.32), it becomes clear that in contrast to the sideband cooling scheme, the steady state can not be a thermal state any more, since for thermal states, P_n/P_{n-1} does not depend on n. The Fock state resolved structure of the reduced master equation now suggests to choose the laser detunings such that a Fock state $|n\rangle$ is prepared. Here, n has to be a small number to be consistent with the RWA (4.9). Fock states with $n > 0$ are highly nonclassical states, which can be nicely illustrated by their Wigner representation, see figure 4.2. Fock states with an odd excitation number n show a negative dip at the origin. The minimum value there is $\hbar W(0,0) = -2/\pi$, which is the minimum value that can be reached for any quantum state.

In order to obtain a steady state close to a Fock state $|n\rangle$, it turns out that at least three different laser driven cavity modes are needed. Two modes are used to drive

the transitions $|n-1\rangle \rightarrow |n\rangle$ and $|n+1\rangle \rightarrow |n\rangle$ in a balanced manner. In order to stabilize the system in the regime of single phonons, we need a third cavity mode driving the transition $|n+2\rangle \rightarrow |n+1\rangle$ to suppress the occupation of states $|n'\rangle$ with $n' > n+1$. This is achieved by choosing the laser detunings $\Delta_1 = \delta_n$, $\Delta_2 = -\delta_{n+1}$ and $\Delta_3 = -\delta_{n+2}$, respectively, where the driving strength Ω_i has been chosen equally for all lasers.

Using more than three cavity modes, even mixtures of Fock states can be created. Figure 4.4 shows results that have been calculated using (4.32) and by solving for the steady state of the entire system described by (4.8). For the numerical analysis of the full system, the involved level spacings δ_n have been calculated by numerical diagonalization of H_m and the applied laser detunings Δ_j have been adjusted to these values. This is necessary since the corrections of the rotating terms in the nonlinear part to the RWA energies are already comparable to the linewith κ for these parameters. Note that the approximation of the eigen states by Fock states $|n\rangle$ is still good, since the corrections for the states are second order in the small parameter $\lambda/\omega_\mathrm{m}$, while the corrections to the energies are first order.

The parameters that have been used in the calculations correspond to a CNT nanoresonator of length $L_\mathrm{tube} = 1\ \mu\mathrm{m}$ with a unsoftened frequency $\omega_{\mathrm{m},0}/2\pi = 20.7\ \mathrm{MHz}$ that has been tuned by a softening factor $\zeta \approx 4.0$ down to $\omega_\mathrm{m}/2\pi = 5.23\ \mathrm{MHz}$. The enhanced nonlinearity is then $\lambda'/2\pi = 209\ \mathrm{kHz}$ and we asumed a mechanical Q-factor of $Q_\mathrm{m} = 5\times10^6$. The ambient temperature is $T = 20\ \mathrm{mK}$ which is in reach of dilution refrigerators. The cavity is a micro toriod as described in section 3.3 with circumference $L_\mathrm{c} \approx 1.47\ \mathrm{mm}$ and a finesse $\mathcal{F}_\mathrm{c} = 3\times10^6$. The total photon loss rate is then given by the sum of losses into the fiber at rate κ_ex and the intrinsic losses that are given by

$$\kappa_0 = \frac{2\pi c}{n_\mathrm{c} L_\mathrm{c} \mathcal{F}_\mathrm{c}}\,, \tag{4.34}$$

where we asumed subcritical coupling of $\kappa_\mathrm{ex} = 0.1\,\kappa$. This gives a total cavity linewidth of $\kappa/2\pi = 52.3\ \mathrm{kHz}$ which resolves the nonlinearity $\kappa < \lambda'$. At an input power of $P_\mathrm{in} = 1.2\ \mathrm{W}$ an enhanced optomechanical coupling strength of $|g_{\mathrm{m},j}|/2\pi = 20.9\ \mathrm{kHz}$ and an absorbed power of $P_\mathrm{abs} = 10.8\ \mu\mathrm{W}$ is reached for each applied laser. The absorbed power P_abs is the power that reaches into the cooling chamber through the intrinsic cavity losses and is given by

$$P_\mathrm{abs} = \hbar\omega_\mathrm{c}|\alpha|^2\kappa_0 \approx \frac{\kappa_0\kappa_\mathrm{ex}}{\Delta^2+\kappa^2/4}P_\mathrm{in}\,. \tag{4.35}$$

The negativity of the Wigner function for the single phonon Fock state reaches $2\hbar\,W(0,0) = -0.53$ which is about 83% of the minimal attainable value $-2/\pi$. For more moderate parameters $L = 1.7\ \mu\mathrm{m}$, $\zeta = 3.3$, which implies $\omega_\mathrm{m}/2\pi = 2.13\ \mathrm{MHz}$, $\lambda'/2\pi = 85.5\ \mathrm{kHz}$ for the nanobeam, as well as $\mathcal{F}_\mathrm{c} = 2\times10^6$, $L_\mathrm{c} \approx 1.80\ \mathrm{mm}$, $P_{\mathrm{in},1/2} = 22\,\mathrm{mW}$, $P_{\mathrm{in},3} = 44\,\mathrm{mW}$, $Q_\mathrm{m} = 1.5\times10^6$ and $T = 30\,\mathrm{mK}$, one still finds a significant negative peak of depth $2\hbar\,W(0,0) = -0.15$.

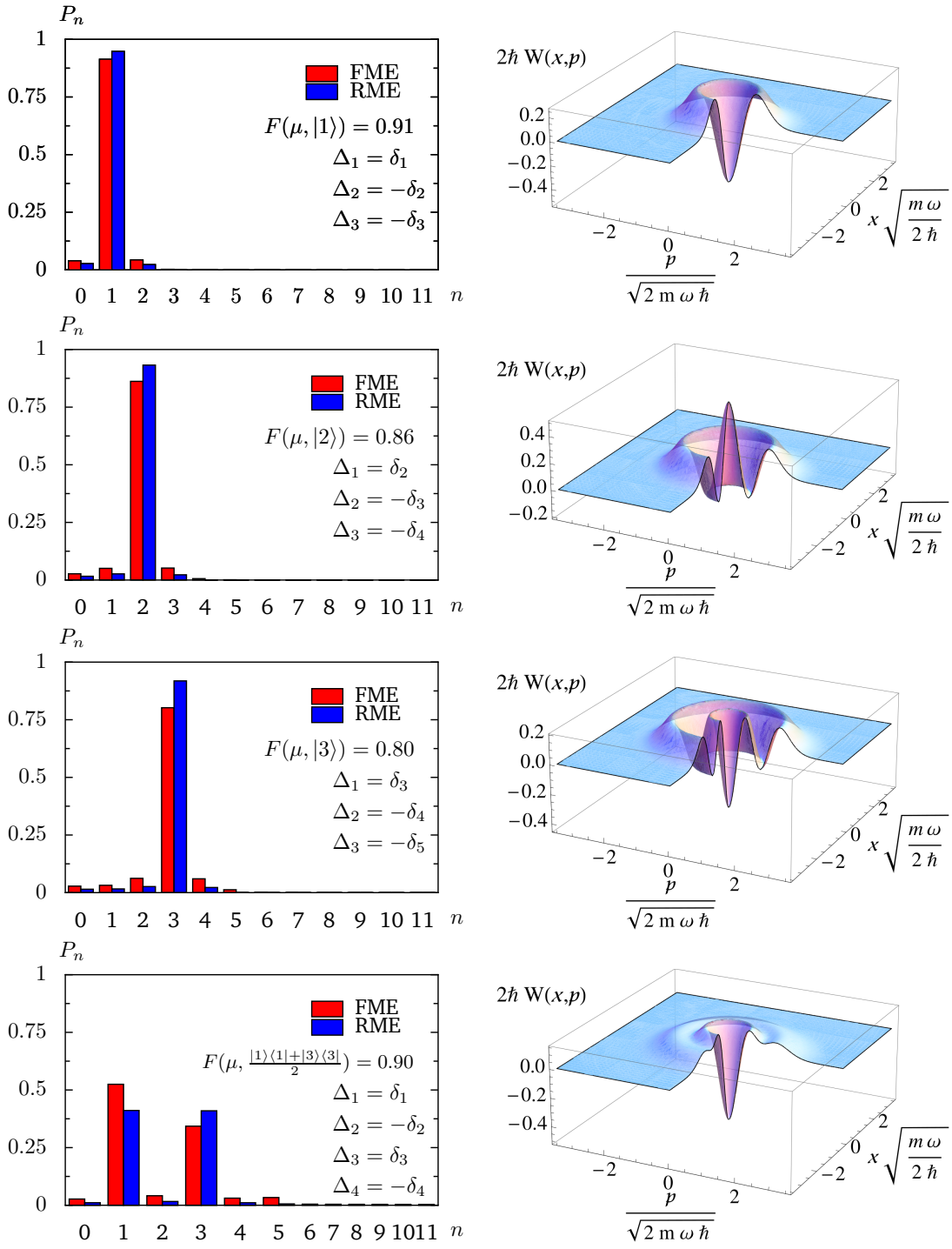

Figure 4.4: Steady state results for the parameters given in the text and for the given Detunings. Left: Occupation probabilities P_n and the state preparation fidelites. The results have been calculated by solving for the steady state of the reduced master equation (RME) using (4.32) and are compared to the exact result for the full master equation (4.8) (FME). Right: The corresponding Wigner functions.

4.8 Readout methods

Here we introduce two methods to measure the prepared stationary state. Both methods benefit from the fact that the prepared states are stationary and in principle can be stable for as long as needed to collect enough data necessary to reconstruct the mechnical state ρ. The first method is similar to the detection scheme used in sideband cooling experiments, where the cooled temperature can be read off the side bands in a power spectrum. It represents a generalization of that scheme to the case of a nonlinear mechanical resonator. The characteristic power spectrum for the cooling scheme can for example found in [64]. The second scheme is a quantum state tomography scheme that has also been adapted for a nonlinear resonator. It allows to reconstruct the characteristic function of the mechanical state, which in turn allows to calculate the Wigner distribution and hence the mechanical state.

4.8.1 Output power spectrum

We analyze the output of an additional weak probe laser a_{in} that resonantly drives an independent cavity mode, while the preparation lasers are on. The output power spectrum for the light of that probe laser that is scattered back into the fiber is given by

$$S(\omega) = \frac{1}{2\pi} \int_{-\infty}^{\infty} \mathrm{d}\tau \mathrm{e}^{-\mathrm{i}(\omega-\omega_{\mathrm{L}})\tau} \left\langle {a_{\mathrm{out}}}^{\dagger}(t+\tau) a_{\mathrm{out}}(\tau) \right\rangle_{\mathrm{SS}} , \tag{4.36}$$

where the output field a_{out} is related to the input field by the input-output relation [28]

$$a_{\mathrm{out}} = a_{\mathrm{in}} - \sqrt{\kappa_{\mathrm{ex}}} a \, . \tag{4.37}$$

The dynamics of the intra cavity field in that probe mode can be described by a quantum Langevin equation for the shifted photon operators

$$\dot{a} = -\frac{\kappa}{2} a - \mathrm{i} \frac{g_{\mathrm{m}}}{2} \left(b^{\dagger} + b \right) + \sqrt{\kappa_{\mathrm{ex}}} \delta a_{\mathrm{in}}(t) + \sqrt{\kappa_0} c_{\mathrm{in}}(t) \, , \tag{4.38}$$

where we introduced the vacuum fluctuations for the input laser δa_{in} and the photon environment c_{in} that is also in a vacuum state. We also neglected again the nonlinear contribution for $|\alpha|^2 \gg \langle a^{\dagger} a \rangle$. This equation of motion is solved by

$$a(t) = a^{(0)}(t) - \mathrm{i} \frac{g_{\mathrm{m}}}{2} \int_0^t \mathrm{e}^{-\frac{\kappa}{2}(t-\tau)} \left[b^{\dagger}(\tau) + b(\tau) \right] \mathrm{d}\tau \tag{4.39}$$

where $a^{(0)}(t)$ is the solution for the decoupled cavity mode which is obtained for $g_{\mathrm{m}} = 0$ in equation 4.38 and which includes the input fields. After changing to the Heisenberg picture (4.10), the steady state motion of the mechanical operators is slow compared to the photon decay. Therefore in this picture, they can be pulled

out of the integral and the upper integration limit can be extended to infinity for a quickly decaying integrand. After changing back to the original picture, we find

$$a(t) \approx a^{(0)}(t) - \mathrm{i}\frac{g_\mathrm{m}}{2}\sum_n \left[\frac{b_n(t)}{\mathrm{i}\delta_n + \kappa/2} + \mathrm{H.c.}\right] \tag{4.40}$$

Besides the contributions to the main line at $\omega = \omega_\mathrm{L}$, the spectrum shows sideband peaks due to the imprint of the mechanical motion onto the photons inside the cavity as described by equation (4.40). The corresponding relevant contributions are given by the mechanical two-time correlatin functions, which can be evaluated using the reduced master equation (4.27). They read

$$\left\langle b_n^\dagger(t+\tau)b_n(t)\right\rangle_\mathrm{SS} = \mathrm{e}^{\left[\mathrm{i}\delta_n - \gamma_\mathrm{eff}^n/2\right]\tau} nP_n\,, \tag{4.41}$$

$$\left\langle b_n(t+\tau)b_n^\dagger(t)\right\rangle_\mathrm{SS} = \mathrm{e}^{\left[-\mathrm{i}\delta_n - \gamma_\mathrm{eff}^n/2\right]\tau} nP_{n-1}\,, \tag{4.42}$$

$$\left\langle b_n^\dagger(t+\tau)b_n^\dagger(t)\right\rangle_\mathrm{SS} = 0\,, \tag{4.43}$$

$$\left\langle b_n(t+\tau)b_n(t)\right\rangle_\mathrm{SS} = 0\,, \tag{4.44}$$

where we neglected the contributions of the $\Delta_\mathrm{m}^{n,\pm}$ as they induce only a small shift of the peak positions. Using $\langle A(t-\tau)B(t)\rangle_\mathrm{SS} = \langle A(t+\tau)B(t)\rangle_\mathrm{SS}^*$ for the negative time integration part, we obtain

$$S(\omega \neq \omega_\mathrm{L}) = \sum_n \frac{\kappa_\mathrm{ex}|g_\mathrm{m}|^2}{4\delta_n^2 + \kappa^2}\left[\mathrm{L}_n(\omega+\delta_n)nP_{n-1} + \mathrm{L}_n(\omega-\delta_n)nP_n\right] \tag{4.45}$$

with Lorentzian sideband peaks at $\omega = \omega_\mathrm{L} \pm \delta_n$,

$$\mathrm{L}_n(\omega) = \frac{1}{\pi}\frac{\gamma_\mathrm{eff}^n/2}{\left[\omega-\omega_\mathrm{L}\right]^2 + \left(\gamma_\mathrm{eff}^n/2\right)^2}\,. \tag{4.46}$$

The weight of these sideband peaks is proportional to the respective occupations P_n, compare figure 4.5. The effective linewidth in the spectrum is broadened by the presence of the preparation lasers and reads

$$\gamma_\mathrm{eff}^n = \sum_j \left\{n\left(A_{-,j}^n + A_{+,j}^n + A_{-,j}^{n-1} + A_{+,j}^{n+1}\right) + A_{+,j}^{n+1} - A_{-,j}^{n-1}\right\} + \gamma_\mathrm{m}(2n+1)(2\overline{n}-1)\,. \tag{4.47}$$

For levels with Fock numbers n that interact with the state preparation lasers, this linewidth is of the order of several $g_{\mathrm{m},j}^2/\kappa$. However for small Fock numbers one still finds $\gamma_\mathrm{eff}^n < \lambda'$, so that the sideband peaks can be resolved.

The ratios P_n/P_{n-1} can now be determined by measuring the integrated peak intensities $I(\omega)$ at positions $\omega - \omega_\mathrm{L} = \pm\delta_n$. From equation (4.45) we find

$$\frac{I(\delta_n)}{I(-\delta_n)} = \frac{P_n}{P_{n-1}}\,. \tag{4.48}$$

These ratios have to be measured until a Fock number n_0, above which it is clear that there is no more influence by the laser drives. In this Fock number regime the ratios are given by the thermal condition

$$\frac{P_n}{P_{n-1}} = \mathrm{e}^{-\beta(E_n - E_{n-1})}\,, \qquad n > n_0\,. \tag{4.49}$$

In order to determine the occupations from the measured ratios one has to calculate P_0, which is given by

$$P_0 = \left(1 + \frac{P_1}{P_0} + \frac{P_1}{P_0}\frac{P_2}{P_1} + \ldots + \frac{P_1 P_2 \ldots P_{n_0}}{P_0 P_1 \ldots P_{n0-1}} + \sum_{n'>n_0} \frac{P_{n'}}{P_0}\right)^{-1}\,. \tag{4.50}$$

The contributions above $n = n_0$ can be estimated

$$\sum_{n'>n_0} \frac{P_{n'}}{P_0} = \frac{P_{n_0}}{P_0} \sum_{l=1}^{\infty} \mathrm{e}^{-\beta\left(E_{n_0+l} - E_{n_0}\right)} \tag{4.51}$$

and should satisfy $\sum_{n'>n_0} P_{n'} \ll 1$ to give a reliable result. The ratio P_{n_0}/P_0 is known from the measurement and an upper bound for the sum $\sum_{n'>n_0} P_{n'}$ can be found by ignoring the nonlinear contribution to the energy. This results into $\sum_{n'>n_0} P_{n'} < \overline{n} P_{n_0}$, while the actual result can be much smaller than that.

4.8.2 Quantum state tomography

Now we turn to the second way to determine the steady state properties. This method applies a state tomography of the output light field of a weak probe laser at several detunings. The full quantum state information of the output can be used to reconstruct the mechanical state. The different detunings can be implemented at once by choosing multiple lasers driving different cavity modes, or by measuring the output for different detunings one after the other. We start again from the Langevin equation (4.38), but now involving a finite detuning Δ_j. In the steady state limit its solution reads

$$a_j(t) = \int_0^t \mathrm{e}^{(\mathrm{i}\Delta_j - \kappa_j/2)(t-\tau)} \left[-\mathrm{i}\frac{g_{\mathrm{m},j}}{2}(b^\dagger(\tau) + b(\tau)) + \sqrt{\kappa_{\mathrm{ex}}}\delta a_{\mathrm{in},j}(\tau) + \sqrt{\kappa_0} c_{\mathrm{in}}(\tau)\right] \mathrm{d}\tau\,, \tag{4.52}$$

where we kept the contributions of the fluctuations explicit this time. Note that those equations of motion for the cavity modes are each given in an interaction picture with the respective laser frequencies. In that picture the coherent shift α_j is a constant. Along the same lines that brought us from equation (4.39) to (4.40), we find

$$\begin{aligned} a_j(t) = &-\mathrm{i} g_{\mathrm{m},j} \sum_n \left[G_j(\delta_n) b_n(t) + G_j(-\delta_n) b_n^\dagger(t)\right] \\ &+ 2G_j(0)\left[\sqrt{\kappa_{\mathrm{ex}}}\delta a_{\mathrm{in},j}(t) + \sqrt{\kappa_0} c_{\mathrm{in}}(t)\right]\,. \end{aligned} \tag{4.53}$$

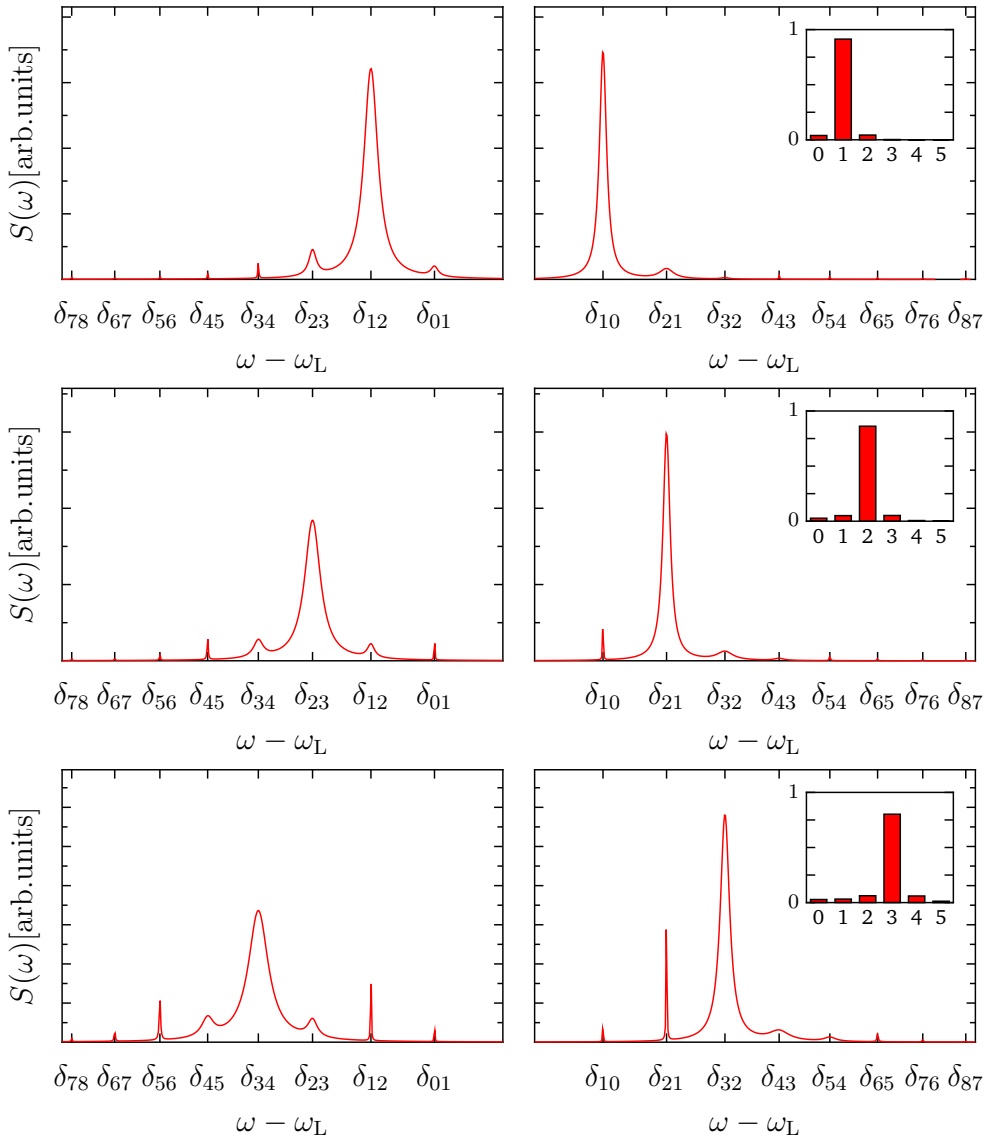

Figure 4.5: Red (left column) and blue (right column) sidebands of the output power spectrum of a weak probe laser measuring different steady states. The steady states are shown in the inset and correspond to the ones in the first column of figure 4.4, which are close to the Fock states $|1\rangle$, $|2\rangle$ and $|3\rangle$. Since the respective state preparation lasers are active, the levels that interact with the state preparation lasers show a broadened linewidth γ_{eff}^{n}. The peak intensities contain the information about the steady state occupations P_n.

Here we used the definition for $G_j(\omega)$ given in (4.25). In the following we merge the cavity fluctuations $\delta a_{\mathrm{in},j}$ and $c_{\mathrm{in}}(t)$ for convenience and express them by a single operator

$$\sqrt{\kappa_{\mathrm{ex}}}\delta a_{\mathrm{in},j}(t) + \sqrt{\kappa_0}c_{\mathrm{in}}(t) \to \sqrt{\kappa_j}\tilde{c}_{\mathrm{in},j}\,. \tag{4.54}$$

It is straight forward to see that this does not affect the results that are following. If we choose the detuning $\Delta_j = -\delta_n$, we can negelect the contributions proportional to $b_n^\dagger(t)$, since $G_j(\delta_n) \gg G_j(\delta_n) =$. Together with the Input-Output-relation (4.37) the output field corresponding to a distinct laser mode reads

$$\begin{aligned} a_{\mathrm{out},j} &= a_{\mathrm{in},j} - \sqrt{\kappa_{\mathrm{ex}}}\left(a_j(t) + \alpha_j\right) && (4.55)\\ &\approx a_{\mathrm{in},j} - \sum_n \mathcal{A}_{nj} b_n - \mathcal{B}_j \tilde{c}_{\mathrm{in},j} - \sqrt{\kappa_{\mathrm{ex}}}\alpha_j\,, && (4.56)\end{aligned}$$

with

$$\mathcal{A}_{nj} = \mathrm{i}\frac{g_{\mathrm{m},j}}{2}\frac{\sqrt{\kappa_{\mathrm{ex}}}}{\mathrm{i}(\Delta_j + \delta_n) - \kappa_j/2}\,, \qquad \mathcal{B}_j = \frac{\sqrt{\kappa_{\mathrm{ex}}\kappa_j}}{\mathrm{i}\Delta_j - \kappa_j/2}\,. \tag{4.57}$$

Here we have neglected only the contribution proportional to $b_n^\dagger(t)$. In the case of well resolved nonlinearity, $\mathcal{A}_{nj}$ is approximately diagonal if we choose detunings $\Delta_j = -\delta_j$ with $j = \{1, 2, 3\ldots\}$. If $\mathcal{A}_{nj}$ as a matrix is invertible, we get

$$b = \sum_n b_n = \sum_{n,j}\left(\mathcal{A}^{-1}\right)_{nj}\left[a_{\mathrm{in},j} - a_{\mathrm{out},j} - \sqrt{\kappa_{\mathrm{ex}}}\alpha_j - \mathcal{B}_j\tilde{c}_{\mathrm{in},j}\right]\,. \tag{4.58}$$

This linear relation allows for the reconstruction of the mechanical state. To show that, we consider the characteristic function $\chi(\xi)$ of quantum state, which is defined by

$$\chi(\xi) = \mathrm{Tr}\left\{\mathrm{e}^{\xi c^\dagger - \xi^* c}\rho\right\} = \mathrm{Tr}\left\{D(\xi)\rho\right\}\,, \tag{4.59}$$

with the shift operator $D_c(\xi) = \exp\{\xi c^\dagger - \xi^* c\}$ and where c and $c^\dagger$ are the operators for the considered mode. The Wigner function is given by the complex Fourier transform of the characteristic function

$$W(\alpha) = \frac{1}{\pi^2}\int \mathrm{d}^2\xi \chi(\xi)\mathrm{e}^{\xi^*\alpha - \xi\alpha^*}\,. \tag{4.60}$$

Using equation (4.58) in the characteristic function for the mechanical mode, we find

$$\begin{aligned}\chi_{\mathrm{m}}(\xi) &= \mathrm{Tr}\left\{D_b(\xi)\rho\right\} = \mathrm{Tr}\left\{\mathrm{e}^{\xi b^\dagger - \xi^* b}\rho\right\}\\ &= \mathrm{Tr}\left\{\prod_j D_{a_{\mathrm{in},j}}(\tilde{\xi}_j) D_{a_{\mathrm{out},j}}(-\tilde{\xi}_j) D_{\tilde{c}_{\mathrm{in},j}}(-\tilde{\xi}_j\mathcal{B}_j^*)\mathrm{e}^{-\sqrt{\kappa_{\mathrm{ex}}}\tilde{\xi}_j\alpha^* + \sqrt{\kappa_{\mathrm{ex}}}\tilde{\xi}_j^*\alpha}\rho\right\}\\ &= \prod_j \chi_{\mathrm{in},j}(\tilde{\xi}_j)\chi_{\mathrm{out},j}(-\tilde{\xi}_j)\chi_{\tilde{c}_{\mathrm{in},j}}(-\tilde{\xi}_j\mathcal{B}_j^*)\mathrm{e}^{-\sqrt{\kappa_{\mathrm{ex}}}\tilde{\xi}_j\alpha^* + \sqrt{\kappa_{\mathrm{ex}}}\tilde{\xi}_j^*\alpha}\,. \end{aligned} \tag{4.61}$$

where we introduced

$$\tilde{\xi}_j = \sum_{n.j} \left(\mathcal{A}^{-1}\right)_{nj} \xi \,. \tag{4.62}$$

The characteristic functions of the input fields and the cavity fluctuations are given by the known functions for the coherent state of the lasers $|\alpha_{\mathrm{L},j}\rangle$ and the vacuum state, respectively. They read

$$\chi_{\mathrm{in},j}(\beta) = \mathrm{e}^{-\frac{|\beta|^2}{2}} \mathrm{e}^{\alpha^*_{\mathrm{L},j}\beta - \alpha_{\mathrm{L},j}\beta^*} \,, \qquad \chi_{\tilde{c}_{\mathrm{in},j}}(\beta) = \mathrm{e}^{-\frac{|\beta|^2}{2}} \,. \tag{4.63}$$

The characteristic functions $\chi_{\mathrm{out},j}$ of the output fields can be measured using homodyne detection schemes and therefore the mechanical state can be reconstructed.

Chapter 5

Quantum information processing

5.1 Introduction

The concept that has been introduced in the last chapter is intended as a tool to explore the nature of mechanical motion in devices that are much larger than typical or "well-established" quantum systems. Therefore its application hopefully supports investigations of rather fundamental character in the field of "macroscopic" quantum systems. Nevertheless, a large part of nowadays investigations that concern the design and control of individual quantum systems aims at the realization of very well defined technical benchmarks. Those benchmarks are set by the requirements for performing quantum simulation and quantum computation [65], and have become a common criterion for the evaluation of the state of the art in the different respective fields. At the same time, high-Q micro- and nanomechanical resonators are also subject to investigations with a much more technical focus. For example, their outstanding quality factors and the ability to couple to electromagnetic fields in a large frequency range via their polarizability have also been used for approaches to logic elements in classical information processing [66, 67]. If we look at carbon nano tubes, in spite of significant difficulties that are associated with precise and controlled integration of many nanotubes in the design of a chip, it was posssible to build a functional computer based on 178 CNT-transistors very recently [68]. The functionality of that approach does not rely on the mechanical properties of the CNTs, but it gives a promising perspective for the feasibility of on-chip applications comprising a larger number of CNTs.

Here, we want combine those qualities with the concept of a mechanical nonlinearity to introduce elementary ideas for quantum information processing with nanomechanical qubits [69]. The quantum information in this approch is stored in the motion of nonlinear nanomechanical resonators. To be able to work as qubits, they are cooled to the groundstate and are tuned into the nonlinear regime, compare section 2.4. While there exists a similar approach to nanomechanical qubits that works inside the buckling regime [70], we here do not rely on a charged resonator, which

makes it much less susceptible to electrical noise, compare section 3.5. Quantum information is processed using the previously introduced gradient forces, as well as optomechanical coupling to a common cavity mode. In order to address only those specific transitions that are needed for the different gate operations, the electrostatic gradient fields are used to individually tune each resonator to a suitable frequency. The further explanations are organized as follows: In section 5.2, we introduce the concept of nanomechanical qubits. In section 5.3, we explain the implementation of single qubit operatios, while in section 5.4 we continue with a fundamental entangling gate. In section 5.6 a brief sketch of a possible initialisation and a readout scheme is given. In sectio 5.5 we finally present numerically obtained results for the gate performance together with a discussion.

5.2 Nanomechanical Qubits

The original definition of a qubit is a two level system formed by two states that are usually labeled by $|0\rangle$ and $|1\rangle$. A perfect qubit can be interpreted as a system with an infinite nonlinearity, where the third and all higher levels have effectively disappeared. A less restrictive, but more practical definition for a qubit is a system, that is controlled in such a way that only two distinct levels are populated, or contribute to the dynamics of a system, while other levels may exist but can be neglected. One prominent example are superconducting qubits, where a nonlinear element, being the Josephson junction turns an originally harmonic superconducting circuit into a system that can be used as a qubit [71]. Here, we introduce a similar approach to establish a nanomechanical qubit. To do so, we tune the nanoresonator to show a sufficiently large enough nonlinearity λ, compare figure 5.1, using the static parts of the tuning fields given in section 2.4, equation (2.30). Usually in this regime, the eigen states and energies of the resonator have to be determined numerically and it is convenient to express all observables in the energy basis, also compare section 2.4. The qubit states are then formed by the ground state $|0\rangle$ and the first excited state $|1\rangle$ and the qubit energy is $\hbar\delta_{10}$. The effective nonlinearity is then rather given by $\delta_{21} - \delta_{10}$. Provided the nanoresonator is initially in the ground state, quantum gates can be applied to one or multiple qubits without leaving the manifold of the qubit states. In the following, concepts for single qubit rotations and a two qubit entangling gate are introduced.

5.3 Single Qubit Gates

A universal set of single qubit gates is given by rotations about all three axes of the Bloch sphere representing the qubit state. The rotations are generated by the Pauli-matrices

$$\hat{\sigma}_x = \begin{pmatrix} 0 & 1 \\ 1 & 0 \end{pmatrix} \qquad \hat{\sigma}_y = \begin{pmatrix} 0 & -\mathrm{i} \\ \mathrm{i} & 0 \end{pmatrix} \qquad \hat{\sigma}_z = \begin{pmatrix} 1 & 0 \\ 0 & -1 \end{pmatrix}, \tag{5.1}$$

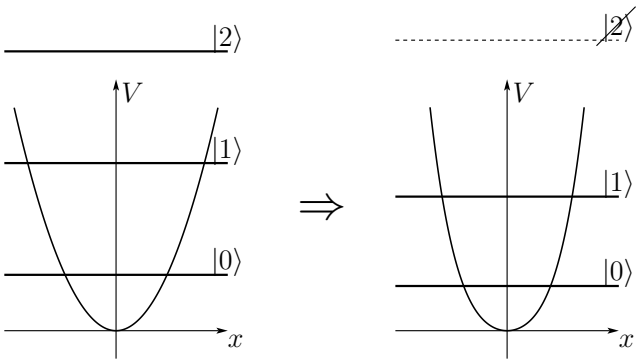

Figure 5.1: A nanomechanical qubit is formed by tuning the nanobeam to be strongly nonlinear. The qubit states are then formed by the two lowest energy levels.

A rotation about an angle ϕ around an axis j is then obtained by implementing an operation $\exp[-\mathrm{i}\phi/2\hat{\sigma}_j]$ that is applied to the current state of the qubit, which is represented by the states

$$\begin{pmatrix}1\\0\end{pmatrix} = |1\rangle\,, \qquad\qquad \begin{pmatrix}0\\1\end{pmatrix} = |0\rangle\,. \tag{5.2}$$

Naturally, this is implemented by the unitary time evolution $\exp[-\mathrm{i}H_\mathrm{G}t/\hbar]$ with a gate Hamiltonian $H_\mathrm{G}(t)$ that is designed to have the shape of the respective Pauli-matrix. For the discussion of gate operations on the qubits it is convenient to choose the interaction picture for the tuned mechanical mode, in which the qubit state is time independent if no gates are applied. Then the only contributions to the Hamiltonian are the time dependent gate pulses that are conducted by the time dependent parts of the gradient fields as introduced in section 2.4, equations (2.29) and (2.30).

We start with rotations about the z-axis. A $\hat{\sigma}_z$-rotation corresponds to a relative phase shift between the two qubit states and is obtained by temporarily tuning the qubit to a different frequency, i.e. adding the time dependend second order contribution $\sim W_{11}(t)\mathcal{X}^2$ to the dielectric potential, compare equations (2.26) and (2.30). Considering the operator $\mathcal{X}^2$ in the rotating frame using the representation (2.35) we find

$$\mathcal{X}^2 \approx \left(\sum_n X_{0n}^2|0\rangle\langle 0| + \sum_n X_{1n}^2|1\rangle\langle 1| + \dots\right)\,, \tag{5.3}$$

where we dropped fast rotating terms and focus only on the qubit subspace. Note that for a nonlinear resonator, there are nonzero higher off-diagonal matrix elements like X_{03}, X_{05}, ..., but the sum

$$c_m = \sum_n X_{nm}^2\,, \tag{5.4}$$

always converges. Thus, by subtracting an irrelevant constant $(c_0 + c_1)/2$ we find

$$\mathcal{X}^2 \approx \left(\frac{c_0 - c_1}{2}|0\rangle\langle 0| + \frac{c_1 - c_0}{2}|1\rangle\langle 1| + \ldots \right) \approx \frac{c_1 - c_0}{2}\hat{\sigma}_z \,. \tag{5.5}$$

The temporary change of the qubit frequency can be expressed by $\delta_{10} \to \delta_{10} + \delta_{10}^1(t)$. Using first order perturbation theory it can be approximated by

$$\delta_{10}^1(t) \approx \frac{1}{2}W_{11}(t)\left[\langle 1|\mathcal{X}^2|1\rangle - \langle 0|\mathcal{X}^2|0\rangle\right] = \frac{1}{2}W_{11}(t)(c_1 - c_0)\,. \tag{5.6}$$

Thus, if $\int \delta_{10}^1(t)\mathrm{d}t = \phi$, the resonator collects a phase shift ϕ during the gate operation and we find

$$\mathrm{e}^{-\mathrm{i}\int \frac{1}{2}W_{11}(t)\mathcal{X}^2\mathrm{d}t/\hbar} \approx \mathrm{e}^{-\mathrm{i}\hat{\sigma}_z\phi/2} \equiv -[\,\phi\,]_{\overline{z}}\,. \tag{5.7}$$

In contrast, rotations about the $\hat{\sigma}_x$- and $\hat{\sigma}_y$-axis are conducted using a time dependend gradient force $\tilde{F}_1(t)$. This force is modulated at the qubit frequency δ_{10}, $F_1(t) = \cos(\delta_{10}t + \theta)\tilde{F}_1(t)$, to drive the transition between the qubit states. Thus, we find for that contribution to the dielectric potential

$$\begin{aligned} F_1(t)\mathcal{X} &= \cos\left(\delta_{10}t + \theta\right)\tilde{F}_1(t)X_{01}\left(\mathrm{e}^{\mathrm{i}\delta_{10}t}|1\rangle\langle 0| + \mathrm{e}^{-\mathrm{i}\delta_{10}t}|0\rangle\langle 1| + \ldots\right) \\ &\approx \tilde{F}_1(t)\frac{X_{01}}{2}\left(\cos\theta\hat{\sigma}_x + \sin\theta\hat{\sigma}_y\right)\,, \end{aligned} \tag{5.8}$$

where we again dropped fast rotating terms. Here we rely on the nonlinearity that causes the transition $|1\rangle \to |2\rangle$ that leads out of the qubit sub space to be off resonant with respect to the drive. Note that for a single $\hat{\sigma}_x$ or $\hat{\sigma}_y$ rotation, the phase θ is irrelavant, since it leads only to a global phase factor. Only for multiple successive $\hat{\sigma}_x$ or $\hat{\sigma}_y$ rotations, the relative phase θ in the gate pulses becomes important. With that in mind, we find for $\theta = 0$ and $\int \mathrm{d}t\tilde{F}_1(t) = \phi/X_{01}$

$$\mathrm{e}^{-\mathrm{i}\int \mathrm{d}tF_1(t)\mathcal{X}} \approx \mathrm{e}^{-\mathrm{i}\hat{\sigma}_x\phi/2} \equiv -[\,\phi\,]_{\overline{x}}\,, \tag{5.9}$$

and for $\theta = \pi/2$ and $\int \mathrm{d}t\tilde{F}_1(t) = \phi/X_{01}$

$$\mathrm{e}^{-\mathrm{i}\int \mathrm{d}tF_1(t)X} \approx \mathrm{e}^{-\mathrm{i}\hat{\sigma}_y\phi/2} \equiv -[\,\phi\,]_{\overline{y}}\,. \tag{5.10}$$

5.4 A Two-Qubit Entangling Gate

In order to implement an entangling two-qubit gate, we employ the interaction of the qubits with a common cavity mode that is driven by a far off resonant laser drive. The Hamiltonian that describes this scenario reads

$$H = -\hbar\Delta a^\dagger a + \hbar\sqrt{2}G_0|\alpha|X_\mathrm{c}(\sum_j \mathcal{X}_j) + \sum_j H_{\mathrm{m},j}\,. \tag{5.11}$$

where we labeled the different resonators or qubits by an index j. Again we already asumed tuned resonators. This means that the effects of the static gradient fields, which is softening and the compensation of static deflection due to the cavity field, are already included in $H_{\mathrm{m},j}$. Furthermore, for the purpose of implementing a two qubit gate we asume that two qubits, e.g. those with indices $j = 1, 2$, are tuned to the same qubit frequency ω_{G} ("gate qubits"), while all the other qubits are tuned to a different frequency ω_{S} ("saved qubits").

For a large detuning $\Delta \gg \{\omega_{\mathrm{G}}, \omega_{\mathrm{S}}\}$, there are no resonant processes between the qubits and the cavity fluctuations and so the later remain in or close to the ground state. This allows to eliminate the photon fluctuations adiabatically which yields an effective interaction Hamiltonian

$$H_{\mathrm{eff}}(t) \approx \frac{1}{\mathrm{i}\hbar} H_{\mathrm{I}}(t) \int_{t_0}^{t} H_{\mathrm{I}}(t')\mathrm{d}t' \,, \tag{5.12}$$

where $H_{\mathrm{I}}(t)$ is the interaction part of the Hamiltonian (5.11) in an interaction picture with respect to $H_0 = -\hbar\Delta a^\dagger a + \sum_j H_{\mathrm{m},j}$. For an derivation of the effective Hamiltonian see appendix A.6. Evaluating equation (5.12) and dropping fast rotationg terms, we find separate effective interactions between gate qubits and saved qubits

$$H_{\mathrm{eff}} \approx H_{\mathrm{G}} + H_{\mathrm{S}} \,, \tag{5.13}$$

where

$$H_{\mathrm{G}} = \hbar \sum_{nm} \sum_{i,j=1}^{2} \frac{G_0^2 |\alpha^2| X_{nm,j}^2}{\Delta - \delta_{mn,j}} |n\rangle\langle m|_i \, |m\rangle\langle n|_j \,, \tag{5.14}$$

$$H_{\mathrm{S}} = \hbar \sum_{nm} \sum_{i,j>2} \frac{G_0^2 |\alpha^2| X_{nm,j}^2}{\Delta - \delta_{mn,j}} |n\rangle\langle m|_i \, |m\rangle\langle n|_j \,. \tag{5.15}$$

For an inital state where all resonators are in the manifold of the qubit states $|0\rangle$ and $|1\rangle$ we can neglect terms involving higher excitations, which allows to adapt this Hamiltonian to the form

$$H_{\mathrm{G}} = \hbar \frac{g_{\mathrm{G}}^2 \Delta}{2(\Delta^2 - \omega_{\mathrm{G}}^2)} \left(\hat{\sigma}_1^+ \hat{\sigma}_2^- + \mathrm{H.c.}\right) + \hbar \sum_{i=1}^{2} \frac{\phi_{\mathrm{G}}}{2} \hat{\sigma}_{z,i} \,, \tag{5.16}$$

$$H_{\mathrm{S}} = \hbar \sum_{i>j>2} \frac{g_{\mathrm{S}}^2 \Delta}{2(\Delta^2 - \omega_{\mathrm{S}}^2)} \left(\hat{\sigma}_i^+ \hat{\sigma}_j^- + \mathrm{H.c.}\right) + \hbar \sum_{i>2} \frac{\phi_{\mathrm{S}}}{2} \hat{\sigma}_{z,i} \,. \tag{5.17}$$

Here we introduced the coupling strength $g_{\mathrm{G/S}} = 2G_0|\alpha|X_{\mathrm{G/S}}$, where $X_{\mathrm{G/S}}$ is the matrix element X_{01} for gate qubits and saved qubits, respectively. For small nonlinearity $\lambda \to 0$, this corresponds to the previously used coupling strength g_{m}, since $X_{01} \to x_{\mathrm{ZPM}}$. The operators $\hat{\sigma}_j^\pm$ are given by

$$\hat{\sigma}_j^\pm = \frac{1}{2}\hat{\sigma}_{x,j} \pm \mathrm{i}\hat{\sigma}_{y,j} \,. \tag{5.18}$$

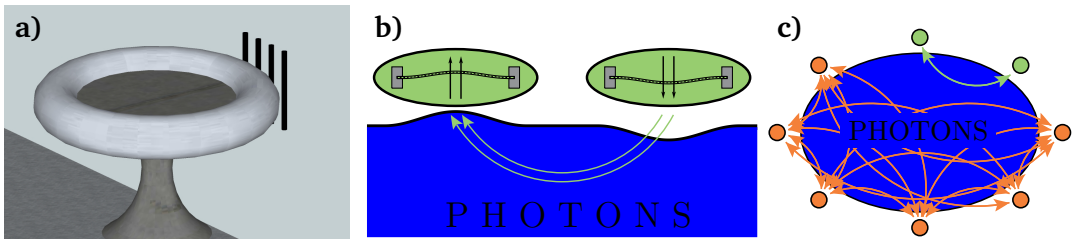

Figure 5.2: **a)** Multiple nanoresonators interacting with a single cavity mode. **b)** Illustration of the effective interaction. The interaction is of $\mathcal{X}_i\mathcal{X}_j$ type and is mediated by the cavity background field. Since the cavity fluctuations do not exchange energy with the resonators, any energy change caused by the deflection of one resonator is compensated by causing forces onto the other resonators. **c)** By tuning the resonators to different frequencies, isolated sets of interacting qubits can be defined. This is used to single out pairs of qubits that are subjected to two-qubit gate operations.

Furthermore we introduced the qubit frequency shifts $\phi_{\mathrm{G/S}}$ that result from the interaction with the cavity fluctuations. They are given by

$$\phi_{\mathrm{G/S}} = G_0^2|\alpha|^2 \sum_m \left(\frac{X_{1m}^2}{\Delta - \delta_{m1}} - \frac{X_{0m}^2}{\Delta - \delta_{m0}} \right)_{\mathrm{G/S}}, \tag{5.19}$$

where the notation $(.)_{\mathrm{G/S}}$ says that the bracket has to be evaluated with the respective parameters for gate qubits and saved qubits. These phase shifts are unwanted but necessarily appear during an entangling gate operation. However the phase shift parts commutate with the rest of the Hamiltonain. Therefore they can always be reversed using local $\hat{\sigma}_z$ operations after, or even during the gate operation, and we will ignore their contribution for the rest of the analysis.

The shape of the Hamiltonian (5.16) is that of a swapping interaction. It preserves the number of excitations and by applying it for a certain amount of time it implements an iSWAP-gate [72], which is a fundamental entangling gate. The interaction strength can be tuned by tuning the optomechanical coupling $g_{\mathrm{G}}(t)$ via the laser input power. If the laser pulse shape is chosen such that the condition

$$\int g_{\mathrm{G}}^2(t')\mathrm{d}t' = \pi \frac{(\Delta^2 - \omega_{\mathrm{G}}^2)}{\Delta} \approx \pi\Delta \tag{5.20}$$

is met, we find for the operation on the gate qubits

$$\mathrm{e}^{-\mathrm{i}\int H_{\mathrm{G}}(t')\mathrm{d}t'/\hbar} = \begin{pmatrix} 1 & 0 & 0 & 0 \\ 0 & 0 & \mathrm{i} & 0 \\ 0 & \mathrm{i} & 0 & 0 \\ 0 & 0 & 0 & 1 \end{pmatrix} \equiv \boxed{\text{iSWAP}} \tag{5.21}$$

However, during the gate operation the saved qubits experience a similar but of course unwanted operation, compare figure 5.2. Since the relevant parameters for

the saved qubits differ from those for the gate qubits, the corresponding operation is some fraction of a generalized iSWAP-gate operation for multiple qubits. We denote it with the symbol

$$\mathrm{e}^{-\mathrm{i}\int H_{\mathrm{S}}(t')\mathrm{d}t'/\hbar} \equiv$$ 

, (5.22)

that here represents an arbitrary number of saved qubits. In order to resolve this problem, the iSWAP operation can be split into two steps of equal time duration, where the second step is the time-reversed operation of the first step. This is achieved by changing the sign of the laser detuning $\Delta \to -\Delta$ in the second step, which changes the sign of the Hamiltonians (5.16) and (5.17). The second inverse operation restores the original state for the saved qubits. In order to prevent this to happen for the gate qubits, local operations can be used. The entire gate operation then reads

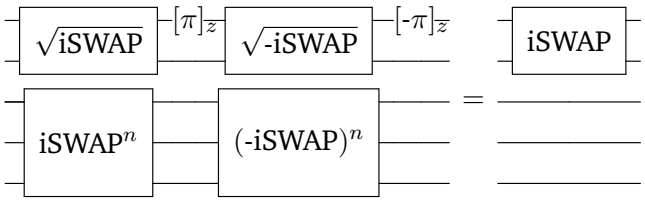

(5.23)

Here, the $\sqrt{\pm\mathrm{iSWAP}}$ operation is achieved by the condition $\int g_{\mathrm{G}}^2(t')\mathrm{d}t' = \pm\pi/2 \times (\Delta^2 - \omega_{\mathrm{G}}^2)/\Delta$. The identity for the gate qubits that has been used in (5.23) can be easily understood by multiplying the corresponding matrix representations.

5.5 Results and discussion

In this section we present results for the gate fidelities that have been obtained by numerical integration of the system dynamics. The nanomechanical resonators that act as the qubits, as well as the cavity are subject to damping at rates γ_{m} and κ, respectively. Therefore we consider the master equation

$$\dot{\rho} = -\frac{\mathrm{i}}{\hbar}\left[H(t),\rho\right] + \frac{\kappa}{2}\mathcal{D}_a\rho + \sum_j \frac{\gamma_{\mathrm{m}}}{2}\left\{(\overline{n}+1)\mathcal{D}_{b_j}\rho + \overline{n}\mathcal{D}_{b_j^\dagger}\rho\right\}, \tag{5.24}$$

with the system Hamiltonian

$$\begin{aligned} H(t) = &-\hbar\Delta a^\dagger a + \hbar\sqrt{2}G_0|\alpha(t)|X_{\mathrm{c}}\left(\sum_j \mathcal{X}_j\right) + \sum_j H_{\mathrm{m},j} \\ &+ \sum_j\left[F_{1,j}(t)\mathcal{X}_j + \frac{1}{2}W_{11,j}(t)\mathcal{X}_j\right], \end{aligned} \tag{5.25}$$

where the local fields are switched off during entangling gates, $F_{1,j} \equiv 0, W_{11,j} \equiv 0$, and the cavity drive is switched off during local gates, $\alpha \equiv 0$. Note that the only time dependent local fields that are active during entangling operations are the once that are used to compensate the photon induced forces.

The effects of the single qubit gates and the iSWAP sequence (5.23) have been calculated by numerical integration of the master equation (5.24). The elementary gates are modelled by rectangular pulses for the relevant control parameters $\alpha(t)$, $F_{1,j}(t)$, $W_{11,j}(t)$ where the gates duration and amplitude is chosen according to the desired operation. Note that the numerical treatment includes the local $\hat{\sigma}_z$-gates for the correction of the unwanted phase shifts $\phi_{\mathrm{G/S}}$ during the entangling gates. For the iSWAP gate, different initials states for the qubit register have been used, with the cavity fluctuations being initially in the groundstate. Each qubit has been modelled using the three lowest levels $|0\rangle, |1\rangle, |2\rangle$, where the third level is needed since population of that level is important source of gate errors. The cavity has been modeled by two levels. In the resulting final state, the cavity degree of freedom is traced out to yield the state of the qubit register ρ_{r}. This state is compared to the result ρ_{i} of the ideal operation by calculating the fidelity

$$F(\rho_{\mathrm{r}}, \rho_{\mathrm{i}}) = \mathrm{Tr}\left\{\sqrt{\sqrt{\rho_{\mathrm{r}}}\rho_{\mathrm{i}}\sqrt{\rho_{\mathrm{r}}}}\right\} . \tag{5.26}$$

The fidelity depends on the choice of initial state, where the lowest fidelity is typically obtained if the gate qubits are in the state $|11\rangle$. This state is most susceptible to the unwanted transition $|1\rangle \to |2\rangle$. In order to give a reasonable measure for the gate performance, we average over the results for a set of states involving of all possible basis states as initial states. To be sure that the gate preserves relative phases in superpositions states, those states are explixitly chosen as $\rho_0 = |\psi_0\rangle\langle\psi_0|$ with

$$|\psi_0\rangle = \frac{1}{\sqrt{2}}\left(|00\ldots\rangle + |ij...\rangle\right) . \qquad i, j, .. \in \{0, 1\} . \tag{5.27}$$

All this has been done for two qubits, which involves four initial states and with four qubits, which involves 16 initial states. The results are shown in figure 5.3, where the following parameters have been used: The qubits are formed by $(10, 0)$-CNTs of radius $R = 0.39\ \mathrm{nm}$, and length $L = 3\ \mu\mathrm{m}$. The untuned frequency of the fundamental deflectional mode is then $2.3\ \mathrm{MHz}$, which is tuned to a qubit frequency of $357\ \mathrm{kHz}$ using electrostatic fields with a maximum at the order of $2\ \mathrm{V}/\mu\mathrm{m}$, compare figure 3.3. For the nonlinearity we then find $\delta_{21} - \delta_{10} \approx 110\ \mathrm{kHz}$. Furthermore we asumed a mechanical Q-factor of 5×10^6 for the qubits and an environmental temperatur of $T = 20\ \mathrm{mK}$. For the cavity we asumed a finesse of 3×10^6, which for a circumference of $97\ \mu\mathrm{m}$ gives an intrinsic photon loss rate of $\kappa_0 = 713\ \mathrm{kHz}$. Together with a fiber-cavity coupling rate of $\kappa_{\mathrm{ex}} = 500\ \mathrm{kHz}$, this gives an total cavity linewidth of $\kappa = 1.21\ \mathrm{MHz}$. For the considered qubit parameters, we find an optimal gate time $T_{\mathrm{G}} = 8.9\ \mu\mathrm{s}$ for both local $\hat{\sigma}_{x,y}$-rotations and the $\sqrt{\pm\mathrm{iSWAP}}$ gates. This optimum results from a trade-off between unwanted excitation of the non-qubit level $|2\rangle$ for too large coupling strengths on the one side and damping losses for too long

gate times on the other side, compare figure 5.3 **a)** and equation (5.20). The field strength for the local $\sigma_{x,y}$ operations are then found at the order of 5×10^{-4} V/μm.

The $\hat{\sigma}_z$-rotations can be performed much faster, so that the duration of the complete iSWAP is approximately $2\ T_{\mathrm{G}}$. We considered a laser detuning of $\Delta = (\pm)53$ MHz and the coupling strength that follows according to the condition (5.20) is $g_{\mathrm{G}} = 1.22$ MHz. This coupling strength is reached for a laser input power of $P_{\mathrm{in}} = 1.1$ W which produces heating in the device due to the absorbed power $P_{\mathrm{abs}} = 137$ μW, compare equation (4.35). Note that in contrast to section 4.4, here the large detuning asures that the cavity fluctuations remain in the ground state, so that the coupling strength may be comparable to κ. However, the interaction via the cavity photons gives rise to an additional decoherence source for the qubits at a rate

$$A_{01} \approx \kappa \left(\frac{g_{\mathrm{G}}}{\Delta}\right)^2 . \tag{5.28}$$

This is found by employing an adiabatic elimination of the cavity fluctuations to derive the effective Hamiltonian (5.13), compare appendix A.7. Here it follows $A_{01} \approx 0.63$ kHz.

For these parameters we find an average gate fidelity of $F = 0.92$ for two qubits and $F = 0.86$ for four qubits. Actually, the saved qubits in this example have not been tuned at all, so that $\omega_{\mathrm{S}} \approx \omega_{\mathrm{m},0}$. This does not affect the scheme, since for negligible nonlinearity, i.e. for harmonic "saved qubit" resonators we find

$$H_{\mathrm{S}} = \frac{g_{\mathrm{m}}^2}{2} \frac{\Delta}{\Delta^2 - \omega_{\mathrm{m},0}^2} \left[\sum_{i>j>2} (b_i^\dagger b_j + \mathrm{H.c.}) + \sum_i (2 b_i^\dagger b_i + 1) \right] \tag{5.29}$$

Therefore the unitary time evolution is also reversed for $\Delta \to -\Delta$ even thought non-qubit states may be populated temporarily during the gate.

The main obstacle that makes it difficult to reach higher gate fidelites are the available optomechanical coupling strengths. Since carbon nanotubes are still very tiny objects compared to solid state nanomechanical resonators, their volume is small compared to the optical mode volume. This can only be compensated by a large coherent cavity field which leads to large amounts of circulating power inside the cavity and is therefore limited. Furthermore the scheme performance relies on employing a relatively large laser detuning, which demands a large laser input power especially for a high finesse cavity. As a consequence, the given example comprises a relatively long CNT in order to increase G_0 and also preferably a cavity with small optical mode volume. The long CNT results into the very low qubit frequency which is much more susceptible to thermal decoherence as one that is close to the GHz regime. Furthermore, reducing the cavity length increases the intrinsic photon decay rate κ_0, compare equation 4.34. Therefore, in the given example, damping losses are the dominant source of gate errors. Without damping, i.e. for $\kappa = \gamma_{\mathrm{m}} = 0$, we find $F = 0.9861$ for two qubits and $F = 0.9860$ for four qubits. This shows the excellent scaling properties of the operational scheme in absence of damping. The relatively large deviation between the two qubit results and the four qubits results

in the presence of damping can be understood from the scaling properties of the fidelity measure, which yields

$$F(\rho_1 \otimes \rho_2, \sigma_1 \otimes \sigma_2) = F_1(\rho_1, \sigma_1) F_2(\rho_2, \sigma_2), \tag{5.30}$$

where here the gate qubits can be represented by ρ_1, σ_1 and the saved qubits by ρ_2, σ_2. Since the dominant damping affects both parts in a similar manner, the error $\mathcal{E} = 1 - F$ in the results for four qubits is approximately twice the error in results for two qubits. The same effect can be also be seen very nicely in plot 5.3 **a)** around $T_{\mathrm{G}}\omega_{\mathrm{G}} \approx 40$, where the gate error for the single qubit rotations are approximately half of that of the two qubit gate. Furthermore by finding the result $F = 0.943$ for only $\kappa = 0$ and $F = 0.961$ for only $\gamma_{\mathrm{m}} = 0$ for two qubits, one can conclude that in this example mechanical losses and cavity losses are at the same order of magnitude.

The different plots can be further understood by considering the cavity induced error rate (5.28). Upon changing any parameter, the ratio $g_{\mathrm{G}}^2 T_{\mathrm{G}}/\Delta$ has to be fixed to allow for a complete gate, compare equation 5.20. So by increasing the gate time T_{G} for fixed detuning Δ in plot 5.3 **a)**, the cavity induced error during one gate does not change, while in contrast the mechanical damping error is increased and dominates for long gate durations. Upon increasing the laser detuning in plot 5.3 **b)** for fixed T_{G}, the cavity induced error scales as $\sim 1/\Delta$, which can be seen in plot. However the cost in laser input power that is needed to increase the coupling g_{G} is then proportional to Δ^4 for otherwise fixed parameters, which drastically limits the range of available detunings.

5.6 Initialisation and Readout

The qubit register can be initialized in the groundstate $|000\ldots\rangle$ for all qubits by resolved sideband cooling. One possibility is to use one laser for each qubit, where every qubit is tuned to a different qubit frequency. Another possiblity is to tune all qubits to the same frequency and use just one laser drive. Then the register of N resonators can be decomposed in N normal modes, where only the center of mass mode $\sum_{n=1}^{N} \mathcal{X}_n$ couples to the cavity and is cooled. However, using local σ_z-rotations, the phase of single resonators can be changed $\mathcal{X}_i \rightarrow -\mathcal{X}_i$, which in effect interchanges the normal modes. In this way all normal modes can be cooled successively to the groundstate which prepares the state $|000\ldots\rangle$.

After performing gate operations, the qubits can be read out using a shelving technique to determine whether a qubit is in state $|0\rangle$ or in state $|1\rangle$ [73, 74]. Here, a cycling transition between $|1\rangle \leftrightarrow |2\rangle$ using a cooling laser on $|2\rangle \rightarrow |1\rangle$ and a coherent rf-drive with local gradient fields on those two levels is employed. The cooling drive is only resonant to the $|2\rangle \rightarrow |1\rangle$ transition for a resolved nonlinearity $\kappa < \delta_{21} - \delta_{10}$. For the rf-drive at frequency δ_{21}, the underlying priciple is exactly the same as that of the previously introduced σ_x-gate, only that the drive is resonant to the $|1\rangle \leftrightarrow |2\rangle$ transition. Here, avoiding off-resonant transitions is achieved by a

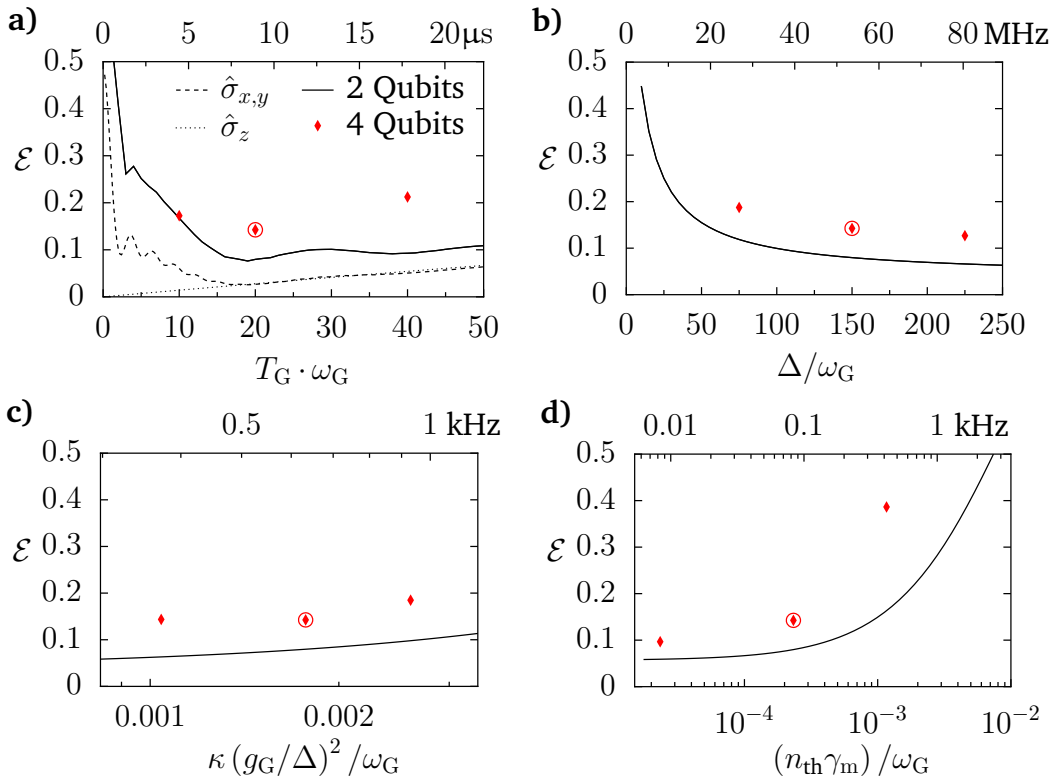

Figure 5.3: Gate errors $\mathcal{E} = 1 - F$ for local operations and the iSWAP-gate. The example that is discussed in the text is marked by a red circle: **a)** Error as a function of gate time T_G. For the iSWAP operation, T_G is the duration of the elementary $\sqrt{\pm\mathrm{iSWAP}}$ gate. For short gate times, the interaction has to be strong, so that higher mechanical levels are excited. In this regime the relevant RWA breaks down. **b)** The gate performance increases for large detunings, as interactions with cavity flucuations are reduced. However this demands increased coupling strengths, i.e. input power for the cavity drive. **c)** Gate error as a function of cavity induced decoherence controlled by κ (g_G and Δ are fixed). The interaction of the qubits with the cavity gives rise to additional loss terms, see appendix A.7 for Details. **d)** Gate performance as a function of the mechanical damping rate.

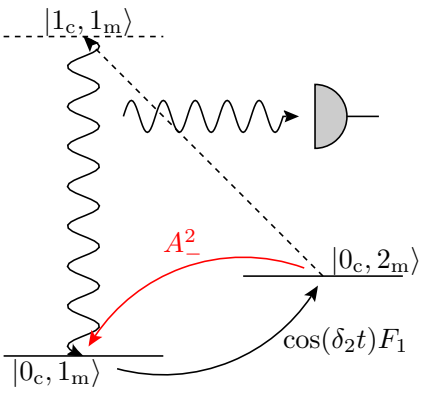

Figure 5.4: Sketch of the qubit readout. The transition between the mechanical levels $|1\rangle \leftrightarrow |2\rangle$ is driven by a cooling drive that is resonant to that transition, compare section 4.5, and by a coherent gradient force drive. If the qubit is projected into state $|1\rangle$, a continious cyclic transition starts. The cooling drive $|2\rangle \rightarrow |1\rangle$ involves the up conversion of laser photons by δ_{21} at rate A_-^2. These photons can be detected. If the qubit is projected into state $|0\rangle$, the drives are off-resonant so that there is no cyclic transition and hence no converted photons.

weak enough drive, compare also the performance of the σ_x-gate in figure 5.3 **a)**. This causes a continious stream of up converted photons only if the resonator is found in the state $|1\rangle$, compare figure 5.4. The upconverted photons can be detected by measuring the corresponding sideband spectrum. A large enough number of photons has to be collected before external damping destroys the intermediate state, which requires $\kappa_{ex}|g_m|^2/\kappa^2 \gg \gamma\overline{n}$.

Unfortunately, both the initialization scheme and the readout scheme can not be applied for the parameters of the presented example, since the condition of resolved sidebands $\kappa \ll \omega_G$ and $\kappa \ll \delta_{21} - \delta_{10}$ is not met. Also further quantitative investigations of these schemes are yet do be done to estimate the corresponding fidelities.

Conclusion and outlook

In summary, the findings that are presented in this thesis can be condensed to the following statement: The concept of tuning nanomechanical resonators, and thereby enhancing their nonlinearity to significant single phonon strength, opens a versatile tool box for controlling and manipulating their motion in the quantum regime. This ranges from the manipulation of a single nanobeam as applied in chapter 4 to implementing interactions within an array or register of nanobeams as employed in chapter 5. In all the presented results, the quantum nature of the nanomechanical motion is inherent. This was explicitly demonstrated by the given steady state results, where a negative Wigner function witnesses the nonclassical nature of the motion of a single resonator. Necessarily, quantum behaviour is also incorporated in the entanglement of different nanomechanical qubits as produced by the application of the introduced iSWAP-gate. While here two different schemes have been introduced, the employed control mechanisms could also be used to investigate other interesting quantum effects, for example beyond the buckling transition for the nanobeam. It is important to note that this generality is a consequence of introducing the nonlinearity only within the mechanical degree of freedom instead of relying on a nonlinear optomechanical coupling. Thereby the optical cavity remains a "passive" control element in the sense that quantum aspects of its dynamics are negligible.

A significant part of this thesis had its emphasis on details of a specific setup, that could possibly be used to implement the introduced schemes. This includes details like the optimization of the arrangement of the CNT and the electrodes on the NEMS chip to optimize the optomechanical coupling strength as well as carefully considered concerns about possible cavity losses introduced by the electrodes. Furthermore one important goal was to optimize the parameters within the theory under the constraint of feasable "external" parameters, since a demonstration of feasibility or at least a good understanding of possible limitations are of course important for the significance within the current context of the field. However unfortunately, regarding the introduced concept of quantum information processing, some questions had to be left uncovered by the scope of this thesis. These are quantitative investigations of the initialisation and readout scheme, as well as details of a possible qubit register setup. Yet, regarding the rather dynamic evolution of experimental techniques in the fields of optomechanics, the respective nanofabrication and of course also of CNT related techniques, the presented scheme is not necessarily restricted

neither to the presented parameters nor even to the presented setup.

Another setup that has been employed to couple to the mechanical modes of CNTs are superconducting circuits that operate in the microwave regime. Here, the nano tube acts as a superconducting junction in a superconducting quantum interference device (SQUID). Since deflections of the CNT change the area enclosed by the SQUID, the flux through the SQUID is modulated and thus coupling to the mechancial motion is achieved [75, 76]. In such a setup, the coupling rate could be tuned by the strength of the magnetic field through the SQUID, and could potentially exceed the coupling rates that are found in optomechanical setups.

Regarding the role of the anharmonic resonator, conventional nanoresonators that are top-down fabricated from bulk material like, for instance SiN or even diamond, are rather unfavorable candidates for the presented schemes, since their geometrical nonlinearity is much smaller than that of a CNT. Yet an interesting alternative could be found in graphene sheets. Their deflectional modes show properties similar to CNTs, which are high frequencies due to the high elasticity and high Q-values that even increase for small motional amplitudes [33]. The intrinsic mechanical nonlinearity of a graphene sheet should also be large, since the energy upon deformation is dominated by streching of the sheet. Possible setups could use graphene sheets as capacitor plates in superconducting micro wave circuits [11].

Appendix

A.1 Corrections due to mode coupling

Here, we discuss the effects of the nonlinearity induced coupling between the normal modes of a nanobeam. This coupling leads to two different effects. One is a potential shift of the fundamental mode frequency which can be absorbed in a redefintion of $\omega_{\mathrm{m},0}$. The other is the tunneling of phonons between modes, potentially leading to unwanted effects like additional losses. Here, we concentrate on the second effect and show that the corresponging processes can be savely neglected. Physically, tunneling between modes is supressed due to the large frequency gap, which can be mathematically accounted for by corresponding rotating wave approximations. In order to estimate the strength of the mode coupling, we rewrite the nonlinearity

$$\lambda^0_{ijkl} = \frac{\hbar}{32\kappa^2 m}\left[\frac{\mu^2 L^2 \tilde{M}_{ij}\tilde{M}_{lk}}{\sqrt{m_i^* m_j^* m_k^* m_l^*}\nu_i\nu_j\nu_k\nu_l}\right] . \tag{A.1}$$

The parts in the brackets are numerical values that result from the shape of modes only and do not depend on the physical quantities L, μ, κ. This can be seen from substituting $\tilde{\phi}_n(\tilde{x}) \equiv \phi_n(L\tilde{x})$, which yields

$$\tilde{M}_{ij} = LM_{ij} = \int_0^1 \tilde{\phi}_i'\tilde{\phi}_j' \mathrm{d}x \,, \tag{A.2}$$

$$m_n^* = \mu L \int_0^1 \tilde{\phi}_n^2 \mathrm{d}x \,. \tag{A.3}$$

Table A.1 shows some numerically obtained values for the bracket (A.1) that are relevant for the fundamental mode. Table A.2 shows values for $\tilde{M}_{ij}$ and the effective masses m_n^*.

We can now estimate the weight of processes corresponding to terms $c_i^{(\dagger)}c_j^{(\dagger)}c_k^{(\dagger)}c_l^{(\dagger)}$ in the multi mode Hamiltonian (2.20) This can be done by comparing those transition matrix elements to the respective energy spacings. The most relevant process is tunneling between the fundamental mode (mode index $n = 1$) and the closest mode of the same parity which ist the third lowest mode (mode index $n = 3$). Including the effect of softening, the corresponding ratio between coupling strength

$j \diagdown i$	1	2	3	4	5
1	0.3024	—	0.1029	—	-0.0512
2	—	0.4106	—	-0.0848	—
3	0.1029	—	0.4498	—	0.0705
4	—	-0.0848	—	0.4721	—
5	-0.0512	—	0.0705	—	0.486232

Table A.1: Numerically obtained nonlinearity induced mode coupling strengths $\lambda_{11ij}/$ in units of $\hbar/(32\kappa^2 m)$. Only modes of same parity couple to each other. Diagonal entries correspond to density-density interactions while off diagonal elements represent phonon tunneling.

$j \diagdown i \tilde{M}_{ij}$	1	2	3	4	5
1	4.88	—	4.36	—	-3.39
2	—	22.1	—	-8.80	—
3	4.36	—	50.0	—	12.2
4	—	-8.80	—	94.6	—
5	-3.39	—	12.2	—	132
$m_i^*/(\mu L)$	0.3965	0.4790	0.5059	0.5514	0.4998

Table A.2: Geometric mode coupling parameters $\tilde{M}_{ij}$ and effective mode masses m_n^* in units of the physical resonator mass μL (bottom row).

and energy gap reads

$$\frac{\lambda_{1113}}{\Delta E_{13}} \approx \frac{0.34\,\zeta_1^{3/2}}{5.4 - 1/\zeta_1} \left(\frac{\lambda_0}{\omega_{\mathrm{m},0}}\right), \tag{A.4}$$

where $5.4\,\omega_{\mathrm{m},0}$ is the frequency of the third mode for the considered boundary conditions and $0.34\,\zeta_1^{3/2}$ results from the ratio $\lambda_{1113}/\lambda^0_{1111}$. Note that while the fundamental mode frequency is changed by the softening factor ζ_1, the third mode's change in frequency can be neglected, compare figure A.2 **a)**. In figure A.1, we show the ratio (A.4) for a typical nanomechanical resonator. Also note that for $\zeta_1 \gg 1$ (A.4) becomes insignificant as the physical nonlinearity saturates in that regime while the given ratio does not. For an estimate of course also the phonon excitation numbers in the respective modes have to be considered. Here, we restrict our analysis to the regime close to the ground state, which can be achieved by sideband cooling for the fundamental mode and by low enough ambient temperature $k_{\mathrm{B}}T \sim \hbar\omega_3$ for the higher modes. Therefore, this additional factor should be $\mathcal{O}(1)$.

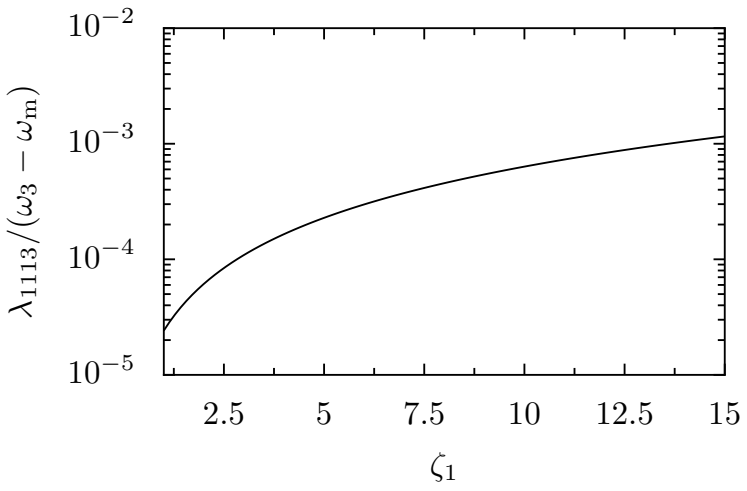

Figure A.1: Ratio of coupling strength over energy gap for as a figure of merit for the most relevant tunneling process between fundamental mode and third mode of the nanobeam. This example corresponds to a nanotube of $3\ \mu\mathrm{m}$ length.

A.2 Calculations for electrostatic tuning

Here, a short discussion of the expansion of the dielectric potential in (2.25) is provided. Furthermore calculations for the diagonalization of the potential including the electrostatic fields are given.

Expansion of the electrostatic potential

The expansion (2.25) of the electrostatic energy around $y = 0$ is stopped after the harmonic term, which is the second order in y. The elastic potential however has been expanded further in order to obtain a nonlinear potential. Therefore, it is indicated to check wether higher order terms in the dieletric potential would have a significant influence on the nonlinearity.

The electrodes that provide the electric field are modeled as point charges q, q', compare figure 2.3. Here, we relabel the charges by $q = Q + \epsilon$, $q' = Q - \epsilon$, so that $Q = 0$ corresponds to an antisymmetric configuration and the field along the nanobeam has only components perpendicular to the beam axis. In contrast for $\epsilon = 0$, we have a symmetric configuration and the field is directed parallel to the tube. We asume that the point charges are placed at a distance $y = \pm d$ from the tube next to the waist of the fundamental mode at $x = L/2$. Using this model we expand the dielectric potential and compare the fourth order term to the elastic nonlinearity. The resulting different order terms are quite complicated for the general case of that model. Therefore we only consider the lowest order in (d/L) for $d \ll L$, which reads

$$V_{\mathrm{el}} \approx \frac{3\pi}{4d^3}\left(\frac{1}{4\pi\epsilon_0}\right)^2\Bigg[Q\epsilon(\alpha_{||}+3\alpha_\perp)\left(\frac{\mathcal{X}}{d}\right) - \frac{1}{16}\left(Q^2(17\alpha_{||}+41\alpha_\perp)+5\epsilon^2(3\alpha_{||}+11\alpha_\perp)\right)\left(\frac{\mathcal{X}}{d}\right)^2 + \frac{10}{3}Q\epsilon(\alpha_{||}+3\alpha_\perp)\left(\frac{\mathcal{X}}{d}\right)^3 - \frac{5}{128}\left(Q^2(65\alpha_{||}+181\alpha_\perp)+7\epsilon^2(9\alpha_{||}+29\alpha_\perp)\right)\left(\frac{\mathcal{X}}{d}\right)^4\Bigg] \tag{A.5}$$

where we dropped the constant term. Note that the resonator length L dropped out since for $d \ll L$ only parts of the beam in the vicinity of the electrodes contribute to the energy. That allows also to approximate the deflectional field $y(x)$ by the displacement $\mathcal{X}$ of the fundamental mode. In order to compare the relevant magnitudes, we consider a field strength that softens the nanobeam to the buckling point. By neglecting the contribution of $\alpha_\perp \ll \alpha_{||}$, this happens as soon as

$$\frac{17}{16}Q^2 + \frac{15}{16}\epsilon^2 \equiv \frac{1}{2}m^*\omega_{\mathrm{m},0}^2 d^2\,. \tag{A.6}$$

As we do not intend to enter the bistable regime, this is an upper bound for the field strength. Note that for the purpose of comparing different orders, we dropped the common prefactor, so that the left and the right side in this equation have actually different physical dimensions. That's why we choose the "$\equiv$" sign. In order to justify the neglect of the fourth order term in the elastic potential, we need

$$\frac{5\cdot 65}{128}\,Q^2 + \frac{5\cdot 63}{128}\,\epsilon^2 \overset{!}{\ll} \frac{\beta}{4} = \frac{0.06}{4}\frac{m^*\omega_{\mathrm{m},0}^2}{\kappa^2}d^4\,. \tag{A.7}$$

Inserting $m^*\omega_{\mathrm{m},0}^2$ from (A.6) finally results into

$$\kappa^2 \overset{!}{\ll} 0.06\left(\frac{2\left(\frac{17}{16}\,Q^2+\frac{15}{16}\,\epsilon^2\right)}{10\left(\frac{2\cdot 65}{128}\,Q^2+\frac{2\cdot 63}{128}\,\epsilon^2\right)}\right)d^2 \tag{A.8}$$

which means $\kappa^2 \ll 0.012\,d^2$ or $\kappa \ll 0.11\,d$. This gives a lower bound for the electrode distance d, as for smaller distances, nonlinear gradient forces have to be considered.

Diagonalization of the combined potential

In order to diagonalize the combined elastic and dielectric potential $V_{\mathrm{b}} + V_{\mathrm{el}}^{(2)}$, it is conventient to change to a different normalisation of modes that the one given in

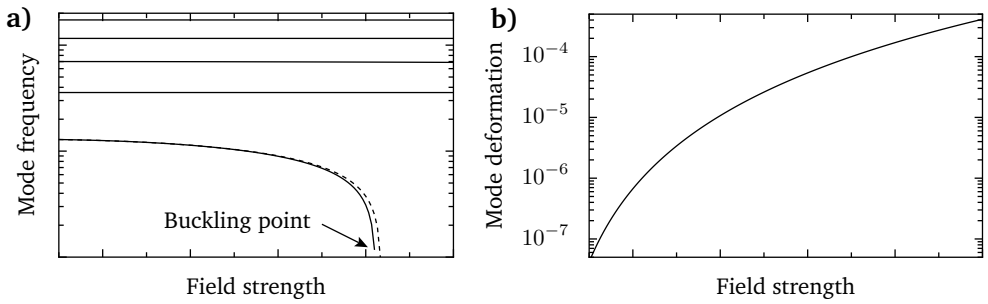

Figure A.2: **a)** Typical behaviour for the mode frequencies subject to a softening field. Only the fundamental mode frequency is significantly lowered. Solid lines are obtained numerically by diagonalizing the harmonic potential, compare equations (A.10). (A.11). The dashed line for the fundamental mode is obtained with the approximation (2.31). **b)** Average deformation of modes $1-F$, where F is the average of overlap $\int \mathrm{d}x\overline{\phi}_n(x)\overline{\phi}'_n(x)$ between the unsoftened normal modes $\overline{\phi}_n$ and the softened normal modes $\overline{\phi}'_n$.

(2.7) and (2.9). Instead we expand the displacement in modes that are normalized to unity, compare also (2.10)

$$y(x,t) = \sum_n \overline{\phi}_n(x)\overline{\mathcal{X}}_n(t)\,, \qquad \overline{\phi}_n(x) = \sqrt{\frac{m_n^*}{\mu}}\phi_n(x)\,, \qquad \overline{\mathcal{X}}_n(t) = \sqrt{\frac{\mu}{m_n^*}}\mathcal{X}_n(t)\,, \tag{A.9}$$

In that description all mode masses are the same, which allows to diagonalize only the harmonic potential part, given by

$$V^{(2)} = V_\mathrm{b} + V_\mathrm{el}^{(2)} = \sum_{lk}\frac{\mu}{2}\left[\omega_l^2\delta_{lk} + \frac{1}{\mu}\overline{W}_{lk}\right]\overline{\mathcal{X}}_l\overline{\mathcal{X}}_k\,, \tag{A.10}$$

$$= \sum_j \frac{\mu}{2}\omega_j'^2\overline{\mathcal{X}'}_i^2\,, \tag{A.11}$$

while the kinetic part does not change. Here we also adapted the normalization of the coefficients W_{lk}, compare equation (2.28)

$$\overline{W}_{lk} = \int_0^L \left.\frac{\partial^2 W(x,Y)}{\partial Y^2}\right|_{Y=0}\overline{\phi}_l(x)\overline{\phi}_k(x)\mathrm{d}x = \frac{\mu}{\sqrt{m_l^* m_k^*}}W_{lk} \tag{A.12}$$

and introduced ω'_j as the tuned eigenfrequencies obtained upon diagonalization. For the parameters that are considered later, we find that the change in the mode shape is negligible, e.g. $\overline{\mathcal{X}'}_i \approx \overline{\mathcal{X}}_i$, compare figure A.2. This means we can change back to the original modes $\mathcal{X}_i$ and end up with the mechanical Hamiltonian for the fundamental mode (2.32).

A.3 Optimization of C_{corr}

The geometric correction factor in (3.16) has to be optimized with respect to the angles ϑ, φ. The correction factor factorizes $C_{\mathrm{corr}} = C(\vartheta)D(\varphi)$, so that the two functions C and D kann be optimized independently.

By substituting $x = \sin^2\vartheta$, we find immediatly that $C = x\sqrt{1-x}$ is maximized for $x_* = \sin^2\vartheta_* = 2/3$, leading to $C(\vartheta_*) = \frac{2}{3\sqrt{3}}$.

To optimize $D(\varphi)$, we substitute $x = \sec\varphi$ and $\tilde{a} = 2\kappa_\perp(d+a_{\mathrm{c}}) \gg 1$. Thus, we have

$$D(x) = \mathrm{e}^{\tilde{a}}\frac{\mathrm{e}^{-\tilde{a}x}}{x^3}\sqrt{x^2-1}\,, \tag{A.13}$$

$$D'(x) = \mathrm{e}^{\tilde{a}}\frac{\mathrm{e}^{-\tilde{a}x}}{x^3}\left[\frac{x}{\sqrt{x^2-1}} - (\tilde{a}+3)\sqrt{x^2-1}\right]. \tag{A.14}$$

Therefore, D is maximized if

$$(\tilde{a}+3)x_*^2 - x_* + (\tilde{a}+3) = 0 \Rightarrow x_* \approx \frac{1}{2\tilde{a}} \overset{(+)}{(-)} \sqrt{1+\frac{1}{4\tilde{a}^2}} \approx 1 + \frac{1}{2\tilde{a}} \Rightarrow \varphi_* \approx \sqrt{1/\tilde{a}}\,, \tag{A.15}$$

for which we find $D(\varphi_*) \approx 1/\sqrt{\mathrm{e}\tilde{a}}$ and consequently $C_{\mathrm{corr}} \approx 0.23/\sqrt{\tilde{a}}$.

A.4 Calculations for electrode losses

Incident field and power

By using equations (3.24)-(3.29) in the Fourier expansion of the incident field, we find

$$E_{z'}^{(\mathrm{in})}(k') = \frac{-\mathrm{i}\omega}{\kappa_\perp}\sqrt{a_{\mathrm{c}}(d+a_{\mathrm{c}})}\tilde{\xi}\mathrm{e}^{-\kappa_\perp d}B_z(0)\underbrace{\int_{-\infty}^{\infty}\mathrm{d}x\frac{\mathrm{e}^{-\kappa_\perp(d+a_{\mathrm{c}})(\sqrt{1+x^2}-1+\mathrm{i}\tilde{k}x)}}{(1+x^2)^{3/4}}}_{F}\,,$$

where we have substituted $x = z'\sin\theta/(d+a_{\mathrm{c}})$ and $\tilde{k} = (k' - n_{\mathrm{c}}k\cos\theta)/(\kappa_\perp\sin\theta)$. The integral F can be estimated by applying the method of steepest descents, using $\kappa_\perp(d+a_{\mathrm{c}}) \gg 1$ and $d \sim \kappa_\perp^{-1} \ll a_{\mathrm{c}}$, which yields

$$|F| \approx \sqrt{2\pi/(d+a_{\mathrm{c}})\kappa_\perp}\mathrm{e}^{-\kappa_\perp(d+a_{\mathrm{c}})|\tilde{k}|} \tag{A.16}$$

for $|\theta| \ll 1$ and is maximized by $k' = k$ for small angles.

The calculation of the incident power involves the integral

$$\int_0^{a_{\mathrm{c}}=3.83/\gamma} rJ_1^2(\gamma r)\mathrm{d}r = \frac{1}{\gamma^2}\int_0^{3.83} xJ_1^2(x)\mathrm{d}x \approx \frac{1.19}{\gamma^2}\,. \tag{A.17}$$

Scattered power

We integrate the energy flux through the surface of a cylinder with radius $R_* \to \infty$ that encloses the electrode. The component of the energy flux perpendicular to the cylinder surface for scattered wave with z'-dependence $\mathrm{e}^{\mathrm{i}k'z'}$ is given by

$$\langle \hat{r}' \cdot \vec{S} \rangle = \frac{1}{2} \Re\{\hat{r}' \cdot (\vec{E} \times \vec{H})\} = \frac{1}{2} \Re \left\{ \frac{\mathrm{i}c\epsilon_0 k}{k'^2 - k^2} \frac{\partial E_{z'}^{(s)}}{\partial r'} E_{z'}^{(s)*} \right\} . \tag{A.18}$$

We further use the far field and near field approximations

$$H_0^{(1)}(x) \approx \mathrm{i}\tfrac{2}{\pi} \ln x \qquad x \ll 1, , \tag{A.19}$$

$$H_0^{(1)}(x) \approx \sqrt{2/\pi x} \exp\left[\mathrm{i}(x - \pi/4)\right] \qquad x \gg 1 , \tag{A.20}$$

so that by using the abbreviation $\tilde{\kappa} = \sqrt{k^2 - k'^2}$ we have at the cylinder surface

$$E_{z'}^{(s)}(k') \approx -E_{z'}^{(\mathrm{in})}(k') \frac{2}{\pi} \frac{1}{\sqrt{\tilde{\kappa} R_*}} \frac{\mathrm{e}^{\mathrm{i}\tilde{\kappa}R_*}}{\mathrm{i}\frac{2}{\pi} \ln(\tilde{\kappa}R)} , \tag{A.21}$$

$$\frac{\partial}{\partial r'} E_{z'}^{(s)}(k') \bigg|_{r'=R_*} \approx \left[\mathrm{i}\tilde{\kappa} - \frac{1}{2R_*} \right] E_{z'}^{(s)}(k') . \tag{A.22}$$

The ϕ'-integration immediately gives $2\pi R_*$, since the only scattering mode considered here does not depend on φ'. The integration along the electrode axis is carried out in k'-space, so that we have

$$\begin{aligned} P_s &= 2\pi R_* \int_{-k}^{k} \frac{\mathrm{d}k'}{2\pi} \langle \hat{r}' \cdot \vec{S} \rangle \\ &= \frac{\pi}{4} c\epsilon_0 \int_{-k}^{k} \frac{\mathrm{d}k'}{2\pi} \frac{k |E_{z'}^{(\mathrm{in})}(k')|^2}{\sqrt{k^2 - k'^2} \ln^2\left[(k^2 - k'^2)R\right]} . \end{aligned} \tag{A.23}$$

An upper bound for the scattered power is given by substituting $|E_{z'}^{(\mathrm{in})}(k')|$ with its maximum in $\{-k, k\}$ and pulling it out of the integral, giving

$$P_s \lesssim \pi c\epsilon_0 \max \left\{ \left| E_{z'}^{(\mathrm{in})}(k') \right|^2 \right\} \Big|_{|k'| \le k} \underbrace{2 \int_0^k \mathrm{d}k' \frac{k}{(k^2 - k'^2) \ln^2\left[(k^2 - k'^2)R^2\right]}}_{I} \tag{A.24}$$

The integral I can be estimated after some substitutions $x = \frac{1}{2}(1 - \frac{k'}{k})$, $u = \frac{\ln x}{\ln(2kR)}$, and $\alpha = -\ln(2kR) \gg 1$ which transforms I to

$$I = \frac{1}{\alpha} \int_{(\ln 2)/\alpha}^{\infty} \frac{\mathrm{d}u}{1 - \mathrm{e}^{-\alpha u} \left[u - \frac{1}{\alpha} \ln(1 - \mathrm{e}^{-\alpha u}) + 2 \right]} . \tag{A.25}$$

By taking now the limit $\alpha \to \infty$, which corresponds to the sub-wavelength condition for the electrode radius $kR \to 0$, we find

$$I \approx \frac{1}{\alpha} \int_0^\infty \frac{\mathrm{d}u}{(u+2)^2} = \frac{1}{2|\ln(2kR)|} \,. \tag{A.26}$$

Absorpted power

Using (3.24) in (3.43) we find

$$P_\mathrm{a} \approx \pi R \sigma \frac{\omega^2}{\gamma} \xi^2 a_\mathrm{c} \sin\theta \mathrm{e}^{-2\kappa_\perp d} |B_z(0)|^2 \underbrace{\int_{-\infty}^{\infty} \mathrm{d}x \frac{\mathrm{e}^{-2\kappa_\perp (d+a_\mathrm{c})(\sqrt{1+x^2}-1)}}{(1+x^2)^{3/2}}}_{J} \,, \tag{A.27}$$

where we again substituted $x = z' \sin\theta/(d+a_\mathrm{c})$. The integral J can again be estimated by the method of steepest decents for $2\kappa_\perp(d+a_\mathrm{c}) \gg 1$, which yields $J \approx (\kappa_\perp(d+a_\mathrm{c})/\pi)^{-1/2}$.

A.5 Derivation of the reduced master equation

Inserting the identity $\mathbb{1} = \mathcal{P} + \mathcal{Q}$ in (4.11) and projecting yields coupled equations for the relevant and the irrelevant part

$$\mathcal{P}\dot{\rho} = \mathcal{P}\mathcal{L}\mathcal{P}\rho + \mathcal{P}\mathcal{L}\mathcal{Q}\rho \,, \tag{A.28}$$

$$\mathcal{Q}\dot{\rho} = \mathcal{Q}\mathcal{L}\mathcal{P}\rho + \mathcal{Q}\mathcal{L}\mathcal{Q}\rho \,. \tag{A.29}$$

The formal solution for the irrelevant part reads

$$\mathcal{Q}\rho = \mathcal{T}_+ \mathrm{e}^{\int_{t_0}^t \mathcal{Q}\mathcal{L}(t')\mathrm{d}t'} \int_{t_0}^t \mathrm{d}\tau \mathcal{T}_- \mathrm{e}^{-\int_{t_0}^\tau \mathcal{Q}\mathcal{L}(t'')\mathrm{d}t''} \mathcal{Q}\mathcal{L}\mathcal{P}\rho \,, \tag{A.30}$$

where we asumed that the systems state at initial time t_0 satisfies $\mathcal{Q}\rho(t_0) = 0$. Inserting this into (A.28) yields the Nakashima-Zwanzig equation (4.21). Some useful properties of the projection operators are

$$\mathcal{P}^2 = \mathcal{P} \,, \tag{A.31}$$

$$\mathcal{Q}^2 = \mathcal{Q} \,, \tag{A.32}$$

$$\mathcal{P}\mathcal{Q} = \mathcal{Q}\mathcal{P} = 0 \,, \tag{A.33}$$

In combination with the parts of the Liouvillian we find

$$\mathcal{P}\mathcal{L}_0 = \mathcal{L}_0\mathcal{P} = 0 \,, \tag{A.34}$$

$$\mathcal{P}\mathcal{L}_2 = \mathcal{L}_2\mathcal{P} \,, \tag{A.35}$$

$$\Rightarrow \mathcal{P}\mathcal{L}\mathcal{Q} = \mathcal{P}\mathcal{L}_1\mathcal{Q} \,, \tag{A.36}$$

$$\mathcal{Q}\mathcal{L}\mathcal{P} = \mathcal{Q}\mathcal{L}_1\mathcal{P} \,. \tag{A.37}$$

Identity (A.34) follows since $\mathcal{P}\rho$ is a steady state solution of $\mathcal{L}_0$ and (A.35) follows directly by pulling $\mathcal{L}_2$ out of the trace $\mathrm{Tr_c}\{.\}$. We continue by expanding the integrand in (A.30)

$$\begin{aligned}\mathcal{T}_+ \mathrm{e}^{\int_{t_0}^{t} \mathcal{Q}\mathcal{L}(t')\mathrm{d}t'} \mathcal{T}_- \mathrm{e}^{-\int_{t_0}^{\tau} \mathcal{Q}\mathcal{L}(t'')\mathrm{d}t''} &= \mathcal{T}\mathrm{e}^{\int_{\tau}^{t} \mathcal{Q}\mathcal{L}(t')\mathrm{d}t'} \\ &= \mathrm{e}^{\zeta^2 \mathcal{Q}\mathcal{L}_0\mathcal{Q}(t-\tau)} \left[\mathbb{1} + \mathcal{O}\left(\frac{1}{\zeta}\right)\right], \end{aligned} \tag{A.38}$$

which can be done since $\zeta^2\mathcal{L}_0$ contains the dominating negative real part. In the next step we substitute $\tau' = \zeta^2(t-\tau)$ to get

$$\mathcal{P}\dot{\rho} = \mathcal{P}\left[\zeta\mathcal{L}_1(\zeta^2 t) + \mathcal{L}_2(\zeta^2 t)\right]\mathcal{P}\rho + \mathcal{P}\mathcal{L}_1(\zeta^2 t)\mathcal{Q}\int_0^{\zeta^2 t} \mathrm{d}\tau' \mathrm{e}^{\mathcal{L}_0\tau'}\mathcal{Q}\mathcal{L}_1\left(\zeta^2 t - \tau'\right)\mathcal{P}\rho(t-\tau'/\zeta^2), \tag{A.39}$$

where we also applied the given relations (A.34)-(A.37). Now we apply the limit $\zeta \to \infty$ for which all fast rotating terms drop out and using (4.14) we arrive at (4.22).

The double commutator in (4.24) yields different variations of the photon two-time correlations, where the operators can be reordered using the identies:

$$X_j \rho_{\mathrm{c},j}^{(\mathrm{th})} = \left[\rho_{\mathrm{c},j}^{(\mathrm{th})} X_j\right]^\dagger, \tag{A.40}$$

$$\mathcal{L}_0 \hat{O}^\dagger = \left[\mathcal{L}_0 \hat{O}\right]^\dagger, \tag{A.41}$$

$$\Rightarrow \left[\mathrm{e}^{\mathcal{L}_0\tau}\rho_{\mathrm{c},j}^{(\mathrm{th})} X_j\right]^\dagger = \mathrm{e}^{\mathcal{L}_0\tau} X_j \rho_{\mathrm{c},j}^{(\mathrm{th})}. \tag{A.42}$$

Identity (A.40) directly follows for Hermitian operators, (A.41) can be calculated considering the definition of $\mathcal{L}_0$ and (A.42) follows from that. Note that one has to be careful with expressions containing super operators, since $(\mathcal{L}\hat{O}_1)\hat{O}_2 \neq \mathcal{L}(\hat{O}_1\hat{O}_2)$. Therefore expressions are evaluated using right-associativity if there are no brackets. The correlation terms that appear are

$$\mathrm{Tr_c}\left\{X_j \mathrm{e}^{\mathcal{L}_0\tau} X_j \rho_{\mathrm{c}}^{(\mathrm{th})}\right\} = \left\langle X_j \right\rangle_{\tilde{\rho}}(\tau), \tag{A.43}$$

$$\mathrm{Tr_c}\left\{\left(\mathrm{e}^{\mathcal{L}_0\tau} X_j \rho_{\mathrm{c}}^{(\mathrm{th})}\right) X_j\right\} = \left\langle X_j \right\rangle_{\tilde{\rho}}(\tau), \tag{A.44}$$

$$\mathrm{Tr_c}\left\{X_j \mathrm{e}^{\mathcal{L}_0\tau} \rho_{\mathrm{c}}^{(\mathrm{th})} X_j\right\} = \left\langle X_j \right\rangle_{\tilde{\rho}}^*(\tau), \tag{A.45}$$

$$\mathrm{Tr_c}\left\{\left(\mathrm{e}^{\mathcal{L}_0\tau} \rho_{\mathrm{c}}^{(\mathrm{th})} X_j\right) X_j\right\} = \left\langle X_j \right\rangle_{\tilde{\rho}}^*(\tau). \tag{A.46}$$

Here we used the given identities and defined the expectation value with respect to $\tilde{\rho}(\tau) = \mathrm{e}^{\mathcal{L}_0\tau} X_j \rho_{\mathrm{c}}^{(\mathrm{th})}$

$$\left\langle \hat{O} \right\rangle_{\tilde{\rho}}(\tau) = \mathrm{Tr_c}\left\{\hat{O}\tilde{\rho}(\tau)\right\}. \tag{A.47}$$

The time dependence of $\tilde{\rho}(\tau)$ and therefore of $\langle X_j \rangle_{\tilde{\rho}}(\tau)$ can be calculated since

$$\dot{\tilde{\rho}} = \mathcal{L}_0 \tilde{\rho}\,, \qquad \tilde{\rho}(0) = X_j \rho_{\mathrm{c}}^{(\mathrm{th})}\,. \tag{A.48}$$

We can now calculate $\langle X_j \rangle_{\tilde{\rho}}(\tau)$ using

$$\partial_t \langle a_j \rangle_{\tilde{\rho}}(\tau) = (\mathrm{i}\Delta_j - \kappa_j/2) \langle a_j \rangle_{\tilde{\rho}}(\tau)\,, \tag{A.49}$$

$$\langle a_j \rangle_{\tilde{\rho}}(0) = \frac{\alpha_j}{\sqrt{2}|\alpha_j|}\,, \tag{A.50}$$

$$\left\langle a_j^\dagger \right\rangle_{\tilde{\rho}}(0) = 0\,, \tag{A.51}$$

so that we find

$$\langle X_j \rangle_{\tilde{\rho}}(\tau) = \frac{1}{2} \mathrm{e}^{(\mathrm{i}\Delta_j - \kappa_j/2)\tau} \tag{A.52}$$

from which equations (4.25) and (4.26) follow.

A.6 Derivation of H_{eff} using an effective Schrödinger equation

The effective Hamiltonian (5.12) can be motivated by the derivation of an effective Schrödinger equation. We consider a fast rotating interaction Hamiltonian,

$$H_{\mathrm{I}}(t) = \mathrm{e}^{\mathrm{i}H_0 t/\hbar} H_{\mathrm{I}} \mathrm{e}^{-\mathrm{i}H_0 t/\hbar}\,, \tag{A.53}$$

where the fast time scale is in our example set by the laser detuning $\Delta \gg g_{\mathrm{G}}$ for the photon mode that is part of H_0 and the slow timescale is given by the optomechanical couling at g_{G} in H_{I}. We consider the Schrödinger equation

$$\mathrm{i}\hbar \frac{\partial}{\partial t} |\psi(t)\rangle = H_{\mathrm{I}}(t) |\psi(t)\rangle \tag{A.54}$$

and its formal solution

$$|\psi(t)\rangle = |\psi(t_0)\rangle + \frac{1}{\mathrm{i}\hbar} \int_{t_0}^{t} H_{\mathrm{I}}(t') |\psi(t')\rangle \mathrm{d}t'\,, \tag{A.55}$$

which we plug into the right side of (A.54) to get

$$\mathrm{i}\hbar \frac{\partial}{\partial t} |\psi(t)\rangle = H_{\mathrm{I}}(t) |\psi(t_0)\rangle + \frac{1}{\mathrm{i}\hbar} H_{\mathrm{I}}(t) \int_{t_0}^{t} H_{\mathrm{I}}(t') |\psi(t')\rangle \mathrm{d}t'\,. \tag{A.56}$$

We are now only interested in the dynamics of the slow time scales. As $H_{\mathrm{I}}(t)$ is fast rotating, we drop the first term and identify $|\psi(t')\rangle \approx |\psi(t)\rangle$ as the fast oscillations leave the state nearly unchanged. This leaves us with an effective Schrödinger

equation for the slow time scale from which we extract the effective Hamiltonian

$$H_{\text{eff}}(t) \equiv \frac{1}{\mathrm{i}\hbar} H_{\mathrm{I}}(t) \int_{t_0}^{t} H_{\mathrm{I}}(t')\mathrm{d}t' \,. \tag{A.57}$$

The lower integration limit amounts to an irrelevant intial value that only contributes another fast rotating term.

A.7 Derivation of H_{eff} by adiabatic eliminiation

The same result as above can be derived more rigorously by tracing out the cavity degrees of freedom in the master equation description of the system, including damping. In an interaction picture for the qubits this master equation reads

$$\dot{\rho}(t) = \mathcal{L}(t)\rho(t) \,, \tag{A.58}$$

where we split the Liouvillian $\mathcal{L}(t) = \mathcal{L}_0 + \mathcal{L}_1(t) + \mathcal{L}_2$,

$$\mathcal{L}_0 = \mathrm{i}\left[\Delta a^\dagger a, \rho\right] + \frac{\kappa}{2}\mathcal{D}_a \,, \tag{A.59}$$

$$\mathcal{L}_1(t)\rho = -\mathrm{i}\sqrt{2}G_0|\alpha| \sum_{nm,j} \mathrm{e}^{-\mathrm{i}\delta_{nm,j}t} \left[X_{\mathrm{c}} X_{nm,j} |n\rangle_j\langle m|_j, \rho\right] \,, \tag{A.60}$$

$$\mathcal{L}_2 = \frac{\gamma_{\mathrm{m}}}{2} \sum_j \left\{ (\overline{n}+1)\mathcal{D}_{b_j}\rho + \overline{n}\mathcal{D}_{b_j^\dagger}\rho \right\} \,. \tag{A.61}$$

We again consider the Nakashima-Zwanzig equation of motion for the relevant part, compare section 4.5, equation (4.21)

$$P\dot{\rho} = \mathcal{P}\mathcal{L}(t)\mathcal{P}\rho + \mathcal{P}\mathcal{L}(t) \int_0^t \mathrm{d}\tau \mathcal{T}_+ \left[\mathrm{e}^{\int_0^t \mathrm{d}\tau' \mathcal{Q}\mathcal{L}(\tau')\mathcal{Q}}\right] \mathcal{T}_- \left[\mathrm{e}^{-\int_0^\tau \mathrm{d}\tau'' \mathcal{Q}\mathcal{L}(\tau'')\mathcal{Q}}\right] \mathcal{Q}\mathcal{L}(t)\mathcal{P}\rho \,. \tag{A.62}$$

Following the same procedure as in section 4.5, we arrive at the equation corresponding to equation (4.27) in that section

$$\mathcal{P}\mathcal{L}_1(t) \int_0^t \mathrm{d}\tau' \mathrm{e}^{\mathcal{L}_0\tau'} \mathcal{Q}\mathcal{L}_1(t-\tau')\mathcal{P}\rho(t-\tau') = \tag{A.63}$$

$$-2G_0^2|\alpha|^2 \sum_{ij} \sum_{nmlk} \mathrm{e}^{-\mathrm{i}(\delta_{nm,i}+\delta_{lk,j})t} X_{nm,i} X_{lk,j} \int_0^t \mathrm{d}\tau' \mathrm{e}^{-\mathrm{i}\delta_{lk}\tau'} \times \tag{A.64}$$

$$\times \,\mathrm{Tr}_{\mathrm{c}} \left\{ \left[X_{\mathrm{c}} |n\rangle_i\langle m|_i, \left[\mathrm{e}^{\mathcal{L}_0\tau'} X_{\mathrm{c}} \left(|l\rangle_j\langle k|_j \right), \mathcal{P}\rho \right] \right] \right\} \,. \tag{A.65}$$

After using again the cavity two-time correlation function (4.25), we can rearrange the real parts and imaginary part of (A.65), contributing to the unitary time evolution and damping, respectively. The resulting reduced master equation for the state of the qubit register reads

$$\dot{\mu} \approx -\frac{\mathrm{i}}{\hbar}\left[\sum_j H_{\mathrm{m},j} + \tilde{H}_{\mathrm{G}} + \tilde{H}_{\mathrm{S}}, \mu\right] + \mathcal{L}_2\mu + \sum_{nm} A_{nm} \sum_{ij} \left[2|n\rangle\langle m|_i \mu |m\rangle\langle n|_j - |n\rangle\langle m|_i |m\rangle\langle n|_j \mu - \mu |n\rangle\langle m|_i |m\rangle\langle n|_j\right] \tag{A.66}$$

where

$$\tilde{H}_{\mathrm{G}} = \hbar \sum_{nm} \sum_{i,j=1}^{2} G_0^2 |\alpha^2| \frac{(\Delta - \delta_{nm,j}) X_{nm,j}^2}{(\Delta - \delta_{mn,j})^2 + \kappa^2/4} |n\rangle\langle m|_i \, |m\rangle\langle n|_j \approx H_{\mathrm{G}}\,, \tag{A.67}$$

$$\tilde{H}_{\mathrm{S}} = \hbar \sum_{nm} \sum_{i,j>2} G_0^2 |\alpha^2| \frac{(\Delta - \delta_{nm,j}) X_{nm,j}^2}{(\Delta - \delta_{mn,j})^2 + \kappa^2/4} |n\rangle\langle m|_i \, |m\rangle\langle n|_j \approx H_{\mathrm{S}}\,. \tag{A.68}$$

and the cavity induced decoherence rates, similar to the cooling/heating rates in section 4.5, are given by

$$A_{nm} = 2G_0^2 |\alpha|^2 X_{nm}^2 \frac{\kappa}{(\Delta - \delta_{nm})^2 + \kappa^2/4} \approx \frac{g_{\mathrm{G/S}}^2 \kappa}{\Delta^2}\,. \tag{A.69}$$

The corrections to the effective Hamiltonian 5.13 are of order κ^2/Δ^2 since

$$\frac{(\Delta - \delta_{nm})}{(\Delta - \delta_{mn})^2 + \kappa^2/4} + \frac{(\Delta + \delta_{nm})}{(\Delta + \delta_{mn})^2 + \kappa^2/4} \approx \frac{\Delta}{\Delta^2 - \delta_{nm}^2}\left(1 + \mathcal{O}\left(\frac{\kappa}{\Delta}\right)^2\right)\,, \tag{A.70}$$

and the cavity induced decoherence rates are small as long as $\kappa g_{\mathrm{G}}^2/\Delta^2 \ll \omega_{\mathrm{G}}$.

Bibliography

[1] J. S. Bell, *On the problem of hidden variables in quantum mechanics.* Rev. Mod. Phys. **38**, 447 (1966).

[2] S. Groblacher, T. Paterek, R. Kaltenbaek, C. Brukner, M. Zukowski, M. Aspelmeyer, and A. Zeilinger. *An experimental test of non-local realism.* Nature **449**, 7159 (2007).

[3] G. Binnig, C. F. Quate, and Ch. Gerber. *Atomic force microscope.* Phys. Rev. Lett. **56**, 9 (1986).

[4] D. Rugar, R. Budakian, H. J. Mamin, and B. W. Chui. *Single spin detection by magnetic resonance force microscopy.* Nature **430**, 6997 (2004).

[5] J. Moser, J. GuttingerJ, A. Eichler, M. J. Esplandiu, D. E. Liu, M. I. Dykman, and A. Bachtold. *Ultrasensitive force detection with a nanotube mechanical resonator.* Nat Nano **8**, 493 (2013).

[6] M. Aspelmeyer, T. J. Kippenberg, and F. Marquardt. *Cavity optomechanics.* ArXiv e-prints (2013).

[7] V. B. Braginskii and A. B. Manukin. *Ponderomotive effects of electromagnetic radiation.* JETP **25**, 953 (1967).

[8] P. F. Cohadon, A. Heidmann, and M. Pinard. *Cooling of a mirror by radiation pressure.* Phys. Rev. Lett., **83** 3174 (1999).

[9] D. Kleckner and D. Bouwmeester. *Sub-kelvin optical cooling of a micromechanical resonator.* Nature **444**, 7115 (2006).

[10] M. Poggio, C. L. Degen, H. J. Mamin, and D. Rugar. *Feedback cooling of a cantilever's fundamental mode below 5 mK.* Phys. Rev. Lett. **99**, 017201 (2007).

[11] J. D. Teufel, T. Donner, Dale Li, J. W. Harlow, M. S. Allman, K. Cicak, A. J. Sirois, J. D. Whittaker, K. W. Lehnert, and R. W. Simmonds. *Sideband cooling of micromechanical motion to the quantum ground state.* Nature **475**, 7356 (2011).

[12] J. Chan, T. P. Mayer Alegre, A. H. Safavi-Naeini, J. T. Hill, A. Krause, S. Groblacher, M. Aspelmeyer, and O. Painter. *Laser cooling of a nanomechanical oscillator into its quantum ground state.* Nature, **478** 7367 (2011).

[13] R. Rivière, S. Deléglise, S. Weis, E. Gavartin, O. Arcizet, A. Schliesser, and T. J. Kippenberg. *Optomechanical sideband cooling of a micromechanical oscillator close to the quantum ground state.* Phys. Rev. A **83**, 063835 (2011).

[14] S. L. Adler and A. Basso. *Is quantum theory exact?* Science **325**, 5938 (2009).

[15] P. Rabl, S. J. Kolkowitz, F. H. L. Koppens, J. G. E. Harris, P. Zoller, and M. D. Lukin. *A quantum spin transducer based on nanoelectromechanical resonator arrays.* Nat Phys **6**, 8 (2010).

[16] K. Stannigel, P. Rabl, A. S. Sørensen, P. Zoller, and M. D. Lukin. *Optomechanical transducers for long-distance quantum communication.* Phys. Rev. Lett. **105**, 220501 (2010).

[17] P. Ehrenfest. *Bemerkung über die angenäherte Gültigkeit der klassischen Mechanik innerhalb der Quantenmechanik.* Z. Phys. A **45**, 7-8 (1927).

[18] Q. P. Unterreithmeier, E. M. Weig, and J. P. Kotthaus. *Universal transduction scheme for nanomechanical systems based on dielectric forces.* Nature **458**, 7241 (2009).

[19] A. D. O'Connell, M. Hofheinz, M. Ansmann, R, C. Bialczak, M. Lenander, E, Lucero, M. Neeley, D. Sank, H. Wang, M. Weides, J. Wenner, J, M. Martinis, and A. N. Cleland. *Quantum ground state and single-phonon control of a mechanical resonator.* Nature **464**, 7289 (2010).

[20] A. D. Armour, M. P. Blencowe, and K. C. Schwab. *Entanglement and decoherence of a micromechanical resonator via coupling to a cooper-pair box.* Phys. Rev. Lett. **88**, 148301 (2002).

[21] K. Jacobs. *Engineering quantum states of a nanoresonator via a simple auxiliary system.* Phys. Rev. Lett. **99**, 117203 (2007).

[22] S. M. Carr, W. E. Lawrence, and M. N. Wybourne. *Accessibility of quantum effects in mesomechanical systems.* Phys. Rev. B **64**, 220101 (2001).

[23] P. Werner and W. Zwerger. *Macroscopic quantum effects in nanomechanical systems.* EPL **65**, 2 (2004).

[24] E Babourina-Brooks, A Doherty, and G J Milburn. *Quantum noise in a nanomechanical duffing resonator.* New J. Phys. **10**, 10 (2008).

[25] V Peano and M Thorwart. *Nonlinear response of a driven vibrating nanobeam in the quantum regime.* New J. Phys. **8**, 2 (2006).

[26] M.-A. Lemonde, N. Didier, and A. A. Clerk. *Nonlinear interaction effects in a strongly driven optomechanical cavity.* Phys. Rev. Lett. **111**, 053602 (2013).

[27] M. Ludwig, B. Kubala, and F.Marquardt. *The optomechanical instability in the quantum regime.* New J. Phys. **10**, 9 (2008).

[28] C. W. Gardiner and M. J. Collett. *Input and output in damped quantum systems: Quantum stochastic differential equations and the master equation.* Phys. Rev. A **31**, 6 (1985).

[29] I. Wilson-Rae. *Intrinsic dissipation in nanomechanical resonators due to phonon tunneling.* Phys. Rev. B **77**, 24 (2008).

[30] S. M. Carr, W. E. Lawrence, and M. N. Wybourne. *Accessibility of quantum effects in mesomechanical systems.* Phys. Rev. B **64**, 22 (2001).

[31] J. D. Teufel, T. Donner, Dale Li, J. W. Harlow, M. S. Allman, K. Cicak, A. J. Sirois, J. D. Whittaker, K. W. Lehnert, and R. W. Simmonds. *Sideband cooling of micromechanical motion to the quantum ground state.* Nature **475**, 7356 (2011).

[32] A. K. Hüttel, G. A. Steele, B. Witkamp, M. Poot, L. P. Kouwenhoven, and H. S. J. van der Zant. *Carbon nanotubes as ultrahigh quality factor mechanical resonators.* Nano Letters **9**, 7 (2009).

[33] A. Eichler, J. Moser, J. Chaste, M. Zdrojek, I. Wilson-Rae, and A. Bachthold. *Nonlinear damping in mechanical resonators made from carbon nanotubes and graphene.* Nat Nano **6**, 6 (2011).

[34] S. Zaitsev, O. Shtempluck, E. Buks, and O. Gottlieb. *Nonlinear damping in a micromechanical oscillator.* Nonlinear Dynamics **67**, 1 (2012).

[35] A. K. Hüttel, M. Poot, B. Witkamp, and H. S. J. van der Zant. *Nanoelectromechanics of suspended carbon nanotubes.* New J. Phys. **10**, 9 (2008).

[36] G. A. Steele, A. K. Hüttel, B. Witkamp, M. Poot, H. B. Meerwaldt, L. P. Kouwenhoven, and H. S. J. van der Zant. *Strong coupling between single-electron tunneling and nanomechanical motion.* Science **325**, 5944 (2009).

[37] B. Lassagne, Y. Tarakanov, J. Kinaret, D. Garcia-Sanchez, and A. Bachtold. *Coupling mechanics to charge transport in carbon nanotube mechanical resonators.* Science **325**, 5944 (2009).

[38] V. Sazonova, Y. Yaish, H. Ustunel, D. Roundy, T. A. Arias, and P. L. McEuen. *A tunable carbon nanotube electromechanical oscillator.* Nature **431**, 7006 (2004).

[39] B. Kozinsky and N. Marzari. *Static dielectric properties of carbon nanotubes from first principles.* Phys. Rev. Lett. **96** 166801 (2006).

[40] G. Anetsberger, O. Arcizet, Q. P. Unterreithmeier, R. Riviere, A. Schliesser, E. M. Weig, J. P. Kotthaus, and T. J. Kippenberg. *Near-field cavity optomechanics with nanomechanical oscillators.* Nat Phys, **5**, 12 (2009).

[41] T. J. Kippenberg, S. M. Spillane, and K. J. Vahala. *Demonstration of ultra-high-q small mode volume toroid microcavities on a chip.* App. Phys. Lett. **85**, 25 (2004).

[42] S. M. Spillane, T. J. Kippenberg, O. J. Painter, and K. J. Vahala. *Ideality in a fiber-taper-coupled microresonator system for application to cavity quantum electrodynamics.* Phys. Rev. Lett. **91**, 043902 (2003).

[43] D. J. Alton, N. P. Stern, Takao Aoki, H. Lee, E. Ostby, K. J. Vahala, and H. J. Kimble. *Strong interactions of single atoms and photons near a dielectric boundary.* Nat Phys **7**, 2 (2011).

[44] E. Vetsch, S.T. Dawkins, R. Mitsch, D. Reitz, P. Schneeweiss, and A. Rauschenbeutel. *Nanofiber-based optical trapping of cold neutral atoms.* IEEE Jour. Sel. Top. Quant. Elec. **18**, 6 (2012).

[45] J. D. Jackson. *Classical Electrodynamics*. Wiley, New York (1998).

[46] D. Y. Joh, J. Kinder, L. H. Herman, S.-Y. Ju, M. A. Segal, J. N. Johnson, G. K.-L. Chan, and J. Park. *Single-walled carbon nanotubes as excitonic optical wires.* Nat Nano **6**, 1 (2011).

[47] H. Nyquist. *Thermal agitation of electric charge in conductors.* Phys. Rev. **32**, 1 (1928).

[48] B. C. Stipe, H. J. Mamin, T. D. Stowe, T. W. Kenny, and D. Rugar. *Noncontact friction and force fluctuations between closely spaced bodies.* Phys. Rev. Lett. **87**, 096801 (2001).

[49] *The Nobel Prize in Physics 2012*, Nobelprize.org. Nobel Media AB 2013, <http://www.nobelprize.org/nobel_prizes/physics/laureates/2012/>.

[50] X. Zhou, I. Dotsenko, B. Peaudecerf, T. Rybarczyk, C. Sayrin, S. Gleyzes, J. M. Raimond, M. Brune, and S. Haroche. *Field locked to a fock state by quantum feedback with single photon corrections.* Phys. Rev. Lett. **108**, 243602 (2012).

[51] D. J. Wineland. *Nobel lecture: Superposition, entanglement, and raising schrödinger's cat.* Rev. Mod. Phys. **85**, 3 (2013).

[52] T. Rocheleau, T. Ndukum, C. Macklin, J. B. Hertzberg, A. A. Clerk, and K. C. Schwab. *Preparation and detection of a mechanical resonator near the ground state of motion.* Nature **463**, 7277 (2010).

[53] S. Rips, M. Kiffner, I. Wilson-Rae, and M. J. Hartmann. *Steady-state negative wigner functions of nonlinear nanomechanical oscillators.* New J. Phys. **14**, 2 (2012).

[54] I. Wilson-Rae, N. Nooshi, W. Zwerger, and T. J. Kippenberg. *Theory of ground state cooling of a mechanical oscillator using dynamical backaction.* Phys. Rev. Lett. **99**, 093901 (2007).

[55] F. Marquardt, J. P. Chen, A. A. Clerk, and S. M. Girvin. *Quantum theory of cavity-assisted sideband cooling of mechanical motion.* Phys. Rev. Lett. **99** 093902 (2007).

[56] R. Zwanzig. *On the identity of three generalized master equations.* Physica **30**, 6 (1964).

[57] E. Wigner. *On the quantum correction for thermodynamic equilibrium.* Phys. Rev. **40**, 5 (1932).

[58] K. Vogel and H. Risken. *Determination of quasiprobability distributions in terms of probability distributions for the rotated quadrature phase.* Phys. Rev. A **40**, 5 (1989).

[59] A. Kenfack and K. Zyczkowski. *Negativity of the wigner function as an indicator of non-classicality.* J. Opt. B: Quantum and Semiclassical Optics, **6**, 10 (2004).

[60] A. Mari, K. Kieling, B. Melholt Nielsen, E. S. Polzik, and J. Eisert. *Directly estimating nonclassicality.* Phys. Rev. Lett. **106**, 010403 (2011).

[61] H. Ollivier and W.H. Zurek. *Quantum discord: A measure of the quantumness of correlations.* Phys. Rev. Lett. **88**, 017901 (2001).

[62] M. Hofheinz, E. M. Weig, M. Ansmann, R. C. Bialczak, E. Lucero, M. Neeley, A. D. O/'Connell, H. Wang, J. M. Martinis, and A. N. Cleland. *Generation of fock states in a superconducting quantum circuit.* Nature **454**, 7202 (2008).

[63] H. P. Breuer and F. Petruccione. *The Theory of Open Quantum Systems*. Oxford University Press, (2002).

[64] I Wilson-Rae, N Nooshi, J Dobrindt, T J Kippenberg, and W Zwerger. *Cavity-assisted backaction cooling of mechanical resonators.* New J. Phys. **10**, 9 (2008).

[65] D. P. DiVincenzo. *The physical implementation of quantum computation.* Fortschr. Phys. **48**, 9-11 (2000).

[66] S. C. Masmanidis, R. B. Karabalin, I. De Vlaminck, G. Borghs, M. R. Freeman, and M. L. Roukes. *Multifunctional nanomechanical systems via tunably coupled piezoelectric actuation.* Science **317**, 5839 (2007).

[67] I. Mahboob, E. Flurin, K. Nishiguchi, A. Fujiwara, and H. Yamaguchi. *Interconnect-free parallel logic circuits in a single mechanical resonator.* Nat Comm. **2**, 198 (2011).

[68] M. M. Shulaker, G. Hills, N. Patil, H.-Y. Chen, H.-S. P. Wong, and S. Mitra. *Carbon nanotube computer.* Nature **501**, 7468 (2013).

[69] S. Rips and M. J. Hartmann. *Quantum information processing with nanomechanical qubits.* Phys. Rev. Lett. **110**, 120503 (2013).

[70] S. Savel'ev, X. Hu, and F. Nori. *Quantum electromechanics: qubits from buckling nanobars.* New J. Phys. **8**, 6 (2006).

[71] J. M. Martinis. *Superconducting phase qubits.* Quantum Information Processing **8**, 2-3 (2009).

[72] N. Schuch and J. Siewert. *Natural two-qubit gate for quantum computation using the* XY *interaction.* Phys. Rev. A **67**, 032301 (2003).

[73] H. G. Dehmelt. *Monoion oscillator as potential ultimate laser frequency standard.* IEEE Trans. Instr. Meas. **IM-31**, 2 (1982).

[74] B. G. U. Englert, G. Mangano, M. Mariantoni, R. Gross, J. Siewert, and E. Solano. *Mesoscopic shelving readout of superconducting qubits in circuit quantum electrodynamics.* Phys. Rev. B **81** 134514 (2010.

[75] J.-P. Cleuziou,W. Wernsdorfer, V. Bouchiat,T. Ondarcuhu, and M. Monthioux *Carbon nanotube superconducting quantum interference device.* Nat Nano **1**, 1 (2006).

[76] B. H. Schneider, S. Etaki, H. S. J. van der Zant, and G. A. Steele. *Coupling carbon nanotube mechanics to a superconducting circuit.* Sci. Rep. **2**, 599 (2012).

Acknowledgments

At the end of writing a PhD thesis, once one has finally reached the point of composing acknowledgements, I guess most of us do it facing rather mixed feelings and so do I. On the one hand I feel proud of the work the lies behind me and, only for the moment, also reliefed that it actually lies *behind* me. Nevertheless it is the last chapter note only of a thesis, but also of an important period of my life that I could spend working in an exciting field of research and in a great environment. For that I am grateful.

My special thanks goes to my supervisor Michael Hartmann, who not only gave me the opportunity to work in his group and entrusted me with an exciting research topic, but also accompanied my work with lots of attention, support, room for discussions, and also confidence. But most importantly, his open-minded and kind attitude towards his students created a very familiar and cooperative atmosphere, which I appreciated very much.

That being said I also want to thank all my other colleagues from T34 for the nice time, for various discussions and for the fun on conferences we attended partially together.

Furthermore, I want to thank Martin Kiffner for his help during the first half year and I want to thank Igancio Wilson-Rae for various comprehensive discussions.

I also want to thank Prof. Wilhelm Zwerger for providing the second review of this thesis.

Finally and most of all I want to thank Eva for her support and for being by my side all that time.